2013

Study of microburst-like wind and its loading effects on structures using impinging-jet and cooling-source approaches

Yan Zhang
Iowa State University

Study of microburst-like wind and its loading effects on structures using impinging-jet and cooling-source approaches

by

Yan Zhang

A dissertation submitted to the graduate faculty

in partial fulfillment of the requirements for the degree of

DOCTOR OF PHILOSOPHY

Major: Aerospace Engineering

Program of Study Committee:
Hui Hu, Co-Major Professor
Partha P. Sarkar, Co-Major Professor
Alric P. Rothmayer
Chris R. Rehmann
Xinwei Wang

Iowa State University
Ames, Iowa
2013

TABLE OF CONTENTS

ACKNOWLEDGEMENTS

I would like to express my sincere gratitude and appreciation to my major advisors, Dr. Hui Hu and Dr. Partha P. Sarkar, whose expertise, enthusiasm, and research attitude have been influencing me during my entire Ph.D. period. Without their generous guidance and support, this dissertation would not have been possible. I consider it a great honor to work with these prominent professors in the past four years.

My heartily appreciation also goes to my committee members, Dr. Alric P. Rothmayer, Dr. Chris R. Rehmann, and Dr. Xinwei Wang, for their generous help during my research. I would also like to thank them for evaluating my research work and giving me many insightful comments.

I would like to thank Mr. William L. Rickard and Mr. James D. Benson, for their continuous help on setting up my experimental facilities.

I am grateful to all the staff member at the Department of Aerospace Engineering, especially former and present department sectaries, Ms. Dee Pfeiffer and Ms. Gayle Fay for their help on all the paperwork and many other important things.

Finally, my deepest appreciation is reserved for my wife, Xinxin Wang, who has always been by my side during my Ph.D. study. With her love and encouragement, I have been able to overcome many difficulties in my life. I am also hugely grateful to my father and mother, Shengping Zhang, and Ailing Liu, who have given me this opportunity to study abroad. I cannot become who I am without their unconditional love and support throughout my life.

ABSTRACT

Microburst can produce downdraft and strong divergent outflow wind, whose characteristics are distinct from those of the atmospheric boundary layer (ABL) wind. The current research is directed to simulation of microburst phenomenon and study of the microburst-wind loading effects on different civil structures using laboratory and numerical simulations and scaled models.

In the first part, the steady impinging jet model was comprehensively studied by using a 2-feet-diameter laboratory microburst simulator that can generate a steady impinging jet. Point and Particle Image Velocimetry (PIV) measurements were both conducted. Comparisons suggest that the average wind velocity profile matches well with those derived from field data and previous research. The transient features of impinging jet and cooling source models were studied and compared by performing numerical simulations. Results showed that the cooling source model could produce a reasonable instantaneous radial velocity profile at maximum wind condition, while the transient impinging jet model resulted in some deviation from the field data. Merits and demerits of each modeling method are presented.

The second part of this study relates to the microburst-wind loading effects on different civil structures such as low-rise buildings, an agro-storage structure, and a high-rise building by deploying the microburst simulator to simulate steady-impinging jet flow over geometrically-scaled models. The effects of important parameters, such as the distance of the model from the center of the microburst, the model geometry, and the

orientation of the building with respect to radial outflow of the oncoming microburst-like wind, on the surface pressure distributions as well as the resultant wind loads acting on the test models were assessed quantitatively. Detailed results on both mean and fluctuating wind loads were discussed and compared to those obtained in conventional straight-line or Atmospheric Boundary Layer (ABL) wind.

Finally, a numerical simulation using a commercial CFD code was performed to simulate the microburst flow field and its wind loading effects on a low-rise building and a high-rise building in full scale, utilizing an improved impinging jet model and a cooling source model with temporal and spatial inlet parameters. The macroscopic flow features of the flow field and their comparison with previous numerical, laboratory and field data suggest that by eliminating the strong shear at the jet interface, the improved impinging jet model can generate a reasonable simulation of the transient microburst flow field, similar to that of the cooling source model. Since the cooling source model that has more resemblance to the real microburst is difficult to replicate in the laboratory, the improved impinging jet model as studied here can be considered as an alternative to the steady-impinging jet model commonly used in the laboratory studies, in the future.

CHAPTER 1

GENERAL INTRODUCTION

1. Microburst--Definition, Characteristics, and Damage

A downburst is a localized intense downdraft which descends to the ground resulting in a violent divergent outburst wind near surface. Based on field observations and a meteorological study of the Eastern 66 accident at New York City's JFK airport, Fujita (1976) first coined the term "downburst" to relate the damaging wind near the ground to the strong downdraft in thunderstorms. Downbursts were later further classified into microbursts and macrobursts according to the horizontal extent of the damaging winds (Fujita, 1981; Fujita 1985). A microburst is a "Miso-scale" downburst with damaging wind extending less than 4 km, while a macroburst is a relatively large downburst extending over 4 km. Although smaller in size, microbursts usually produce higher wind speed than macrobursts. In early 1900s, the definition of microburst has been further specified by Federal Aviation Administration, as windshears with peak-to-peak wind speed differences of more than 30 knots (≈15.4m/s) over distances less than 2.5 NM (4.6 km), for the implementation of TDWR & LLWAS (Terminal Doppler Weather Radar & Low Level Windshear Alert System) at major airports.

Microbursts are usually developed during the dissipating stage of thunderstorms, when the cumulonimbus cloud is dominated by sinking currents, i.e. downdrafts. This downdraft of air is driven and accelerated primarily by the evaporative cooling and the mass loading due to the weight of precipitation, as suggested by many meteorological

studies (Srivastava, 1985; Proctor, 1988). Due to the complexity of the atmospheric condition, not all downbursts are alike. Microbursts can be further classified into wet microbursts and dry microbursts based on the level of precipitation during the events. Wet microbursts are those accompanied with heavy rain and hail, which are normally seen in humid areas, such as Southeast and East-coast states in the United States. During wet downbursts, the upper-level dry air is entrained into the lower-level moist air, which catalyzes the evaporative cooling and accelerates the downdraft. On the contrary, dry microbursts occur in an opposite stratification of atmosphere, which has dry air at lower-level and moist air in the high-altitude cloud base. The precipitation from the upper-level cumulonimbus cloud evaporates in the lower-level dry atmosphere, forming so-called "virga" beneath the cloud base. The downdraft is intensified due to the evaporative cooling, but little precipitation is expected at the ground level. Dry microbursts are normally seen in the vast area of the Midwest in the United States.

Microbursts have many distinct flow characteristics differing from the conventional boundary layer winds. First, the outburst wind profile resembles a wall-jet flow, which is different from the conventional logarithmic-law profile, as illustrated in Figure 1. An intense microburst is capable of producing damaging wind near 270 km/h (170 mph) with the maximum wind speed very close to the surface, which makes low-rise buildings more vulnerable to a microburst type wind compared to the boundary-layer wind. Second, due to the impact of downdraft flow and the gravity of the cooled air, high pressure could be expected at the dead center of a microburst. For example, a pressure rise 5 millibars (500 Pa) was detected at Dulles International Airport on June 26, 1978.

(Bedard, 1984). In another study, Fujita (1985) found a pressure rise of about 4 millibars with an extent of less than 2 km during the Andrews Air Force Base microburst. These so-called pressure noses are not normally seen in conventional atmospheric boundary layer winds. Third, a microburst is a transient process which produces a vortex-ring traveling in radial direction. The vortex-ring does not only accelerate the flow beneath it, but also introduce significant vertical velocity component and turbulence. Because of this large-scale structure, it is also believed that the downburst wind is much better correlated laterally than in the conventional boundary layer wind. Fourth, a microburst is often very short-lived (normally 5-15 minutes) and typically non-stationary. These features bring many difficulties to the detection and prediction of microburst events.

Thunderstorms are responsible for nearly one-third of the extreme winds in the United States (Thom, 1969). Over 75% of the peak gust wind speeds occurred during thunderstorms outside the hurricane regions in the United States (Vickery and Twisdale, 1992). Observations suggest that approximately 5% of all thunderstorms produce microbursts. Therefore, microbursts are not rare events and actually much more frequent than tornadoes. Due to the suddenness and intensity, microbursts are extremely dangerous for airplanes at low altitude which are taking off or landing. According to incomplete statistics, there have been approximately 10 fatal accidents happened in the U.S., causing a total number of 573 fatalities during the period 1970-1995 (NTSB/National Research Council). After 1990s, the accident number has been minimized by the successful implementation of TDWR & LLWAS at major airports. Microbursts also cause a considerable amount of damages to civil structures every year,

which is drawing an increasing attention in the wind engineering society. It was reported that an average of $1.4 billion insured property loss every year in the U.S. caused by thunderstorms (data from 1950-1997, Extreme Weather Sourcebook 2001), which is more than the yearly tornado damage reported ($850 million). However, the current design standard of minimum wind loads for civil structures are generally based on model tests in conventional boundary-layer wind tunnels. Since the flow regime resulting from a microburst is completely different from those expected in the conventional boundary-layer winds, microburst wind loads on different civil structures need to be further studied.

2. Literature Review

The study of microburst was initiated within the meteorological society after the investigation of the 1976 Eastern 66 accident at New York City's JFK airport. Since 1970s, several field research projects have been conducted to study the origin, flow structure, and meteorological parameters of the microburst. These famous research projects include the Northern Illinois Meteorological Research on Downburst (NIMROD, Chicago, IL) and the Joint Airport Weather Studies (JAWS, Denver, CO). These studies provided valuable trustworthy data and depicted a vivid picture of microbursts occurring in nature. These field research efforts were documented in Fujita (1979), Wilson et al. (1984), Hjelmfelt (1987), and Hjelmfelt (1988). There are also some field studies outside of these major projects. For example, Atlas, et al. (2003) investigated the physical origin of a microburst occurring in the Amazon region of South America. Vasiloff and Howard (2008) deployed two types of radar systems to capture

data from a severe microburst occurring near Phoenix, Arizona. Meanwhile, many meteorologists have also performed numerical simulations based on the full-cloud model to compare and complement the field studies. Srivastava (1985) examined the properties of a microburst downdraft in a one-dimensional microphysical model and suggested that microburst intensity would increase with the increase of temperature lapse rate, precipitation concentration, and humidity. Proctor (1988, 1989) performed two-dimensional axisymmetric simulation on the Terminal Area Simulation System (TASS) and found that the primary driving force of a microburst was found to be evaporative cooling. Similar uses of the full-cloud models can also be found in Straka and Anderson (1993), Fu and Guo (2006), etc.

From engineering point of view, the near-surface flow characteristics and the flow-structure interaction are of more interests to researchers. Therefore, it is of great importance to develop an appropriate modeling method, which can neglect the complexity of the microphysical process and reasonably reproduce the microburst flow features in a smaller scale. So far there are three different models used for the microburst simulation, either experimentally and numerically. These models are vortex-ring model, impinging jet model, and cooling source model.

The vortex-ring model refers to the theoretical model, which focuses on revealing the structure and evolution of flow patterns around the primary vortex generated in a microburst. Ivan (1985) described a mathematical model of a downburst that resolves the stream function around a ring vortex. The results of this model resembled the primary-vortex pattern found in the JAWS project. Schultz (1990) constructed a multiple vortex-

ring model by using time-invariant vortex ring filaments from potential flow theory. The velocity distribution around this simulated ring vortex matched the field data of the 1985 DFW microburst reasonably well. Vicroy (1992) compared three theoretical models: linear, vortex-ring, and empirical. It was found that latter two types provided better agreements with the field data than the linear model.

The impinging jet model has been widely adopted due to its simplicity and ability to produce reasonable outflow-velocity profiles. As early as in 1987, by summarizing field data collected from a series of Colorado microbursts during the JAWS project, Hjelmfelt (1987) pointed out that the outflow structures were found to have features resembling those of a laboratory-simulated wall jet. Subsequently, the impinging jet model was utilized, both numerically and experimentally, by a number of researchers for microburst studies. Selvam and Holmes (1992) used a two-dimensional k-epsilon model to simulate impingement of a steady jet of air on a ground plane. A reasonable agreement between numerical results and field data was achieved. Holmes (1999) and Letchford and Illidge (1999) performed experimental studies using impinging jet model to investigate topographic effects of a microburst outflow on velocity profiles. Holmes and Oliver (2000) empirically combined wall-jet velocity and translational velocity and obtained a good representation of a travelling microburst which was well correlated with a 1983 Andrews AFB microburst. Wood et al. (2001) experimentally and numerically studied impinging jets over various terrains. Choi (2003) also used an impinging jet flow for the laboratory study to compare with the field observation of a series of Singapore thunderstorms. Mason et al. (2005) deployed a pulsed-jet model to simulate transient

microburst phenomenon. The formation and evolution of the primary, successive intermediate, and trailing edge vortices were visualized and recorded. Sengupta and Sarkar (2008) studied the microburst flow characteristics by conducting laboratory measurement using a steady impinging jet simulator and numerical simulation. Both numerical and PIV results showed good agreements with full-scale data. Similar numerical simulations using impinging jet model can be found in Chay et al. (2005), Kim and Hangan (2007) and Das, et al. (2010).

The cooling source model is an alternative approach to simulate the microburst, whose forcing source is generated by the density difference instead of the momentum input. Experimentally, this method was accomplished by dropping denser fluids into less dense surroundings. These experimental tests can be found in Lundgren et al. (1992), Yao and Lundgren (1996), and Alahyari and Longmire (1995). Nevertheless, the scale of the experimental cooling source model is generally very limited, making it almost impossible to study the wind loading effects on scaled building models. Numerical simulations using cooling source approach usually involves a cooling source function, which was suggested by Anderson (1992). The atmospheric full-cloud model was simplified to a space- and time-dependent cooling source function without considering the microphysical process in the real microburst event. This model was later used by Orf et al. (1996) to study colliding microbursts, and by Orf and Anderson (1999) to study travelling microbursts. Mason et al. (2010) also investigated topographic effects on simulated downbursts using a sub-cloud model. Comparing the simulation results to their previous impinging jet modeling results, they suggested that little discrepancy was

found with respect to the topographic effects. Most recently, Vermeire et al. (2010) compared the non-dimensional results using cooling source model and transient impinging jet model, and claimed that the impinging jet results deviated significantly from the cooling source results due to its unrealistic forcing parameters. However, it remains arguable to evaluate the impinging jet model using the simplified cooling source model as the benchmark. More comparisons with field data and previous research data are needed to compare and validate these two models.

Wind effects on buildings in the boundary-layer winds have been extensively studied during past few decades, by means of full-scale tests, wind-tunnel tests, or numerical simulations. Since microbursts are dramatically different from the conventional boundary-layer winds, the existing design standard generated by conventional boundary layer wind tunnel tests could not provide convincing estimations for the wind loads induced by microburst winds. However, only a very limited number of studies can be found in literature to specifically address the microburst-wind loads acting on different civil structures. Nicholls et al. (1993) conducted a Large Eddy Simulation (LES) study to investigate the flow structures around a cube-shaped building model in microburst-like wind. Savory et al. (2001) utilized an impinging-jet model to investigate the failure of a lattice transmission tower in microburst-like wind. Chay and Letchford (2002) and Letchford and Chay (2002) investigated the pressure distribution over a cube-shaped building model in steady and translating microburst-like wind by performing laboratory experiments with an impinging-jet model. Chen and Letchford (2004) evaluated and compared the maximum dynamic magnification factor (MDMF) of a standard high-rise

building model induced by standard wind profile and conceptual generic downburst wind profiles. More recently, Sengupta et al. (2008) conducted an experimental study to quantify the transient loads acting on a cube-shaped building model with an impinging-jet-based microburst simulator. Besides these efforts, more studies are needed to clearly understand the microburst loading effects on different types of civil structures, such as low-rise houses, agro-storage facilities, bridges, and high-rise buildings.

3. Motivation for Current Research

In summary, the literature review shows several research gaps:

1. Although the impinging jet model was widely adopted for microburst simulation, the detailed flow field characteristics, especially the whole-field information, have not been fully studied.

2. Difference between existing microburst modeling methods, i.e. transient impinging jet model and cooling source model, have not been comprehensively studied. Further, the transient effects of these models have not been validated with field data.

3. The wind loading effects on different types of civil structures are far from being fully understood in the microburst winds, unlike the conventional boundary-layer wind.

4. Very little research has been conducted to reveal the flow field in the vicinity of a realistic building model and the wind-structure interaction in a simulated microburst.

5. Almost no existing literature can be found to address the differences of microburst-wind loading effects on buildings due to different modeling methods.

To fill these gaps, the objectives of the present study are listed as follows:

1. Employ the ISU laboratory microburst simulator (2-foot diameter, 0.61m) with a translating capability to generate and study realistic microburst flow fields. Conduct comprehensive laboratory tests, including point measurements and Particle Image Velocimetry measurements, to study the detailed velocity and turbulence distribution within a simulated microburst flow field.

2. Conduct a numerical simulation to study the different transient behaviors between an impinging jet model and a cooling source model and compare the results with that of the experimental data and field study data.

3. Conduct laboratory tests to study the microburst wind loading effects on different civil structures, using the steady impinging jet flow. Due to the relative scale of microburst flow field and building sizes, low-rise and high-rise buildings will experience dramatically different wind loading effects in microburst winds. Therefore, wind loading effects on these two types of buildings will be studied separately.

4. Conduct a numerical simulation to compare different wind loading effects on buildings due to an impinging jet flow and a cooling source driven flow.

4. Thesis Organization

The dissertation includes five chapters that are in journal paper manuscript format. In addition, a general introduction (Chapter 1) is given at the beginning and a conclusion is provided as the last chapter of the dissertation (Chapter 7). Appendix is also included at the end of this dissertation to discuss the translational effects which are not covered by the main chapters. Due to the format of the dissertation, some repetition might be found in the introduction and experimental setup part of each chapter.

The first paper (Chapter 2) reveals the detailed flow field characteristics of a laboratory steady-impinging jet model and compare transient behaviors of different modeling methods by numerical simulation. The steady impinging jet model was comprehensively studied by using a 2-foot-diameter (0.61m) microburst simulator available in the Department of Aerospace Engineering at Iowa State University. Point measurements and Particle Image Velocimetry (PIV) measurements were both performed to reveal a detailed picture of the overall flow and distribution of velocity and turbulence in the outflow of the steady impinging jet. Transient behaviors of the impinging jet model and cooling source model were then compared by conducting numerical simulation using commercial CFD software, FLUENT (ANSYS 12.1). Both the experimental and numerical results were compared with the data obtained by previous studies and the field studies.

The second paper (Chapter 3) studies the flow-structure interaction and wind loading effects on two gable-roofed building models within a simulated microburst-like wind, compared with those in conventional atmospheric boundary layer (ABL) winds. Two gable-roof building models with the same base plan and mean roof height, but different roof angle, were used for a comparative study. In addition to measuring the surface pressure distributions to determine the resultant wind loads acting on the building models, a digital Particle Image Velocimetry (PIV) system was used to conduct flow field measurements to reveal the wake vortex and turbulence flow structures around the building models placed in the microburst-like wind. The effects of important parameters, such as the distance of the building from the center of the microburst, the roof angle of

the building, and the orientation of the building with respect to radial outflow of the oncoming microburst-like wind, on the flow features such as the vortex structures and the surface pressure distributions around the building models as well as the resultant wind loads acting on the test models were assessed quantitatively.

The third paper (Chapter 4), which studies the microburst-wind loading effects on various low-rise building models with different geometric shapes, could be considered as a continuing work of Chapter 3. In this chapter, microburst-wind loading effects on a cube, a grain bin and two gable-roofed building models were evaluated and compared by performing laboratory tests. Velocity and turbulence intensity profiles at given locations were revealed by point measurements. The distributions of mean and root-mean-square pressure coefficients were shown for selected cases. The results of microburst-wind loads of different models were compared with those obtained in conventional atmospheric boundary-layer winds.

The fourth paper (Chapter 5) studies the mean and dynamic wind loads acting on a high-rise building model in the microburst-like wind. Since the height of a tall building can be easily higher than the depth of the microburst outflow, the high-rise building would suffer a different microburst-wind loading effects than a low-rise building. The mean and dynamic wind loads induced by the simulated microburst were studied in detail by taking both pressure and force measurements. Results were compared with data from previous studies and suggested that the characteristics of wind loads acting on the high-rise building model were dramatically different from those obtained in the ABL wind. Power spectrum density of the velocity and force coefficient fluctuations was also

investigated to reveal different frequency components of the dynamic wind loads. Generally, great complexity of the microburst flow field and the wind loading effect was revealed in this study. Results presented in this paper may be helpful for the safe design of high-rise building in the thunderstorm-prone areas.

The fifth paper (Chapter 6) includes a numerical simulation to simulate the microburst flow field and its wind loading effects on building models, utilizing an improved impinging jet model and a cooling source model. The improved impinging jet model incorporated a space- and time-dependent velocity inlet, which was different from the traditional constant velocity inlet. The cooling source model was simulated by adding a cooling source function into the energy conservation equation, which had a similar spatial and temporal variation as that used in the improved impinging jet model. Macroscopic flow features of both models were shown and compared with those in the previous studies. Flow structure around a high-rise and a low-rise building model was analyzed. The differences of wind loading effects on building models between two modeling methods were discussed.

References

Alahyari A., Longmire E.K., 1995. Dynamics of experimentally simulated microbursts. AIAA Journal. 33 (11), 2128-2136.

Anderson J. R., Orf, L. G., Straka J. M., 1992. A 3-D model system for simulating thunderstorm microburst outflows, Meteor. Atmos. Phys., 49, 125–131.

Atlas D., Ulbrich C.W., Williams C.R., 2004. Physical Origin of a Wet Microburst: Observations and Theory. J Atmos Sci, 61, 1186-1196

Bedard A.J., Jr., 1984. Optimizing the use of surface sensors for wind shear detection. J. Aircraft, 21(12), 971-977.

Chay M.T., Albermani F., Wilson R., 2005. Numerical and analytical simulation of downburst wind loads. Engineering Structures. 28, 240-254

Chay M.T., Letchford C.W., 2002. Pressure distributions on a cube in a simulated thunderstorm downburst, Part A: stationary downburst observations. J. Wind Eng. and Ind. Aerodyn. 90, 711-732.

Chen L., Letchford C.W., 2004. Parametric study on the along-wind response of the CAARC building to downbursts in the time domain. J. Wind. Eng. Ind. Aerodyn. 92, 703–724.

Choi E.C.C., 2004. Field measurement and experimental study of wind speed profile during thunderstorms. J. Wind Eng. and Ind. Aerodyn. 92, 275-290

Das K.K., Ghosh A.K., Sinhamahapatra K.P., 2010. Investigation of the axisymmetric microburst flow field. J. Wind and Eng. 7, 1-15.

Fujita T.T., 1976. Spearhead echo and downburst near the approach end of a John F. Kennedy runway, New York City, SMRP Research Paper, University of Chicago, 137, 51.

Fujita T.T., 1979. Objectives, operations and results of project NIMROD. Preprint, 11th conf. on Severe Local Storms. Kansas City. Amer. Meteor. Society;

Fujita T.T., Wakimoto R.M., 1981. Five scales of airflow associated with a series of downbursts on 16 July 1980. Monthly Weather Review, 109, 1438-1456

Fujita T.T., 1985. The downburst, microburst, and macroburst. SMRP Res. Paper No. 210 [NTIS No. PB85-148880], Univ. of Chicago.

Fu D. and Guo X., 2007. Numerical study on a severe downburst-producing thunderstorm on 23 August 2001 in Beijing. Advances in Atmo. Sci. 24, 227-238.

Hjelmfelt M.R., 1987. The microbursts of 22 June 1982 in JAWS. J Atmos Sci 44(12), 1646-1665.

Hjelmfelt M.R., 1988. Structure and life cycle of microburst outflows observed in Colorado. J. Appl. Meteorol, 27(8), 900-927.

Holmes J. D., 1999. Modeling of Extreme Thunderstorm Winds for Wind Loading of Structures and Risk Assessment. Wind Engineering into the 21st Century, Proc. of the 10th Intl. Conf. on Wind Eng. eds. A. Larsen et al., Denmark, June 1999, 1409−1415.

Holmes J.D., Oliver S.E., 2000. An empirical model of a downburst. Engineering Structures. 22, 1167-1172.

Ivan M., Boeing Computer Services Co., Seattle, WA, 1985: IN: Flight Simulation Technologies Conference, St. Louis, MO, July 22-24, 1985, Technical Papers (A85-40551 19-09). New York, 1985,p. 57-61. AIAA-1985-1749

Kim J., Hangan H., 2007: Numerical simulation of impinging jets with application to downbursts. J. Wind Eng. and Ind. Aerodyn. 95, 279-298.

Letchford C.W., Chay M.T., 2002. Pressure distributions on a cube in a simulated thunderstorm downburst, Part B: moving downburst observations. J. Wind Eng. and Ind. Aerodyn. 90, 733–753.

Letchford C.W., Illidge G., 1999. Turbulence and Topographic effects in Simulated Thunderstorm Downdrafts by Wind Tunnel Jet. Wind Engineering into the 21st Century, Proceedings of the Tenth International Conference on Wind Engineering. eds. A. Larsen G. L. Larose and F. M. Livesey, Denmark, June 1999, 1907-1912.

Lundgren T.S., Yao J., Mansour N.N., 1992, Microburst modeling and scaling. J. Fluid Mech. 239, 461-488.

Mason M.S. Letchford C.W., James D.L. 2005: Pulsed wall jet simulation of a stationary thunderstorm downburst, Part A: Physical structure and flow field characterization. J. Wind Eng. and Ind. Aerodyn. 93, 557-580.

Mason M.S., Wood G.S., Fletcher D.F. 2010. Numerical investigation of the influence of topography on simulated downburst wind fields. J. Wind Eng. and Ind. Aerodyn. 98, 21-33.

Nicholls M., Pielke R., Meroney R., 1993. Large eddy simulation of microburst winds flowing around a building. J. Wind Eng. and Ind. Aerodyn. 46-46, 229-237.

Orf L.G., Anderson J.R., Straka J.M. 1996. A Three Dimensional Numerical Analysis of Colliding Microburst Outflow Dynamics. J. Atmospheric Sciences. 53(17), 2490-2511.

Orf L.G., Anderson J.R., 1999. A Numerical Study of Traveling Microbursts. Monthly Weather Review. 127, 1244-1258.

Proctor F.H., 1988. Numerical simulations of an isolated microburst, part I: dynamics and structure. Journal of the Atmospheric Sciences, 45(21), 3137-3160.

Proctor F.H., 1989. Numerical simulations of an isolated microburst. Part II: Sensitivity Experiment. J. Atmos. Sci. 46, 2143-2165

Savory E. et al., 2001. Modelling of tornado and microburst-induced wind loading and failure of a lattic transmission tower. Eng Struct. 23: 365-375.

Schultz T., 1990. Multiple vortex ring model of the DFW microburst. Journal of Aircraft. Vol. 27, pp. 163-168.

Selvam R.P., Holmes J.D., 1992. Numerical simulation of thunderstorm downdrafts. J Wind Eng Ind Aerod 44: 2817-2825.

Sengupta A., Haan F.L, Sarkar P.P., Balaramudu V., 2008. Transient loads on buildings in microburst and tornado winds. J. Wind. Eng. Ind. Aerodyn. 96, 2173-2187.

Sengupta A., Sarkar P. P., 2008. Experimental measurement and numerical simulation of an impinging jet with application to thunderstorm microburst winds. J. Wind Eng. and Ind. Aerodyn. 96, 345-365.

Srivastava R.C., 1985. A simple model of evaporatively driven downdraft: application to microburst downdraft. Journal of the Atmospheric Sciences, 42(10), 1004-1023.

Srivastava R.C. 1987. A model of intense downdrafts driven by the melting and evaporation of precipitation. J. Atmos. Sci., 44 (13) 1752-1773.

Straka J.M., Anderson J.R., 1992. Numerical Simulations of Microburst-producing Storms: Some Results from Storms Observed during COHMEX. Journal of the Atmo. Sci. 50, 1329-1348.

Thom H.C.S., 1969. New Distributions of extreme wind speeds in the United States. J. Structure Div., ASCE, 94, 1787-1801

Vickery P.J., Twisdale L.A., 1995. Analysis of thunderstorm occurrences and wind speed statistics. J. Wind Eng. Ind. Aerodyn. 55, 813-821

Vicroy D., 1992. Assessment of microburst models for downdraft estimation. Journal of Aircraft. Vol. 29, no. 6, pp. 1043-1048.

Vasiloff S.V., Howard K.W. 2008. Investigation of a Severe Downburst Storm near Phoenix, Arizona, as Seen by a Mobile Doppler Radar and the KIWA WSR-88D. Weather and Forecasting 24: 856-867.

Vermeire B.C., Orf L.G., Savory E., 2011. Improved modelling of downburst outflows for wind engineering applications using a cooling source approach. J. Wind Eng. and Ind. Aerodyn., 99(8), 801-814.

Wilson J.W., Roberts R.D., Kenssiger C., McCarthy J., 1984. Microburst wind structure and evaluation of Doppler radar for airport wind shear detection. J Clim Appl Meteorol 23, 898-915

Wood G.S., Kwok C.S., Motteram N.A., Fletcher D.F., 2001. Physical and numerical modelling of thunderstorm downbursts. J. Wind Eng. and Ind. Aerodyn. 89, 535–552.

Yao J., Lundgren T.S., 1996. Experimental investigation of microbursts. Exp. Fluids 21, 17–25.

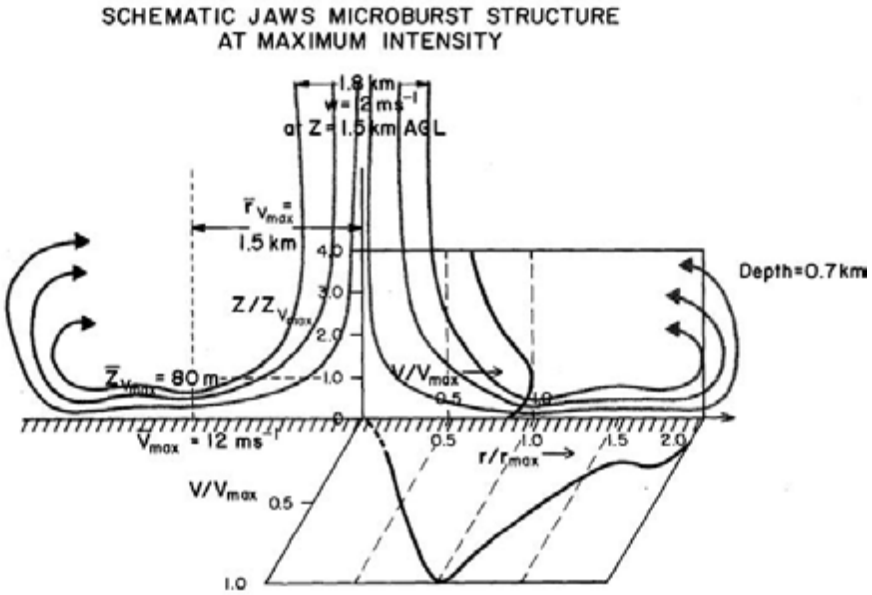

Figure 1. *Schematic of JAWS microburst (Hjelmfelt, 1988)*

Figure 2. *Vortex-ring in a microburst*
(Credit: NOAA Photo Library, NOAA Central Library)

CHAPTER 2

MODELING OF MICROBURST OUTFLOWS USING IMPINGING JET AND COOLING SOURCE APPROACHES AND THEIR COMPARISON

Yan Zhang, Hui Hu, Partha P. Sarkar

Department of Aerospace Engineering, Iowa State University, Ames, Iowa, 50010

Abstract: Microbursts have been simulated and studied using different physical and numerical modeling methods. In the present study, the steady impinging jet model was comprehensively studied by using a 2-foot-diameter (0.61m) microburst simulator available in the Department of Aerospace Engineering at Iowa State University. Point measurements and Particle Image Velocimetry (PIV) results revealed a detailed picture of the overall flow and distribution of velocity and turbulence in the outflow of the steady impinging jet. Comparisons suggested that the average wind velocity profile of the steady impinging jet matched well with those derived from field data and previous research. FFT of the velocity time-history and instantaneous PIV results implied that the outflow consisted of low-frequency periodic shedding of vortices and the steady impinging jet model could be seen as an ensemble average of a series of simulated microburst events. Due to lack of time-dependent evolutionary information of the steady impinging jet model, a transient impinging jet model was studied to capture the transient features which were then compared with those of the cooling-source model by performing numerical simulations. Transient features of the transient impinging jet model and cooling source model showed several differences mainly related to the different formation and transportation process of the primary vortex. Ground surface

pressure distributions were found to be different due to different forcing parameter of the two models. Comparison with the field data suggested that both models resembled the dynamic features of a real microburst outflow. However, results showed that the cooling source model could produce a reasonable instantaneous radial velocity profile at maximum wind condition, while the transient impinging jet model resulted in a large deviation. Finally, merits and demerits of each modeling methods were discussed.

1. Introduction

A microburst is defined as an intense downdraft impacting the ground and forming a damaging outflow with a diameter less than 4 kilometers [1]. Since 1970s, a number of field projects had been conducted to study this natural phenomenon, mainly within the meteorological society [2-5]. Microbursts are dramatically different from the traditional straight-line winds and other wind hazards. They could produce significant wind shear and extreme winds near ground with a wind profile differing from the atmospheric boundary layer. Due to its transient nature, microbursts usually have very short lifespan and large vertical velocity components, which make it difficult to be detected and studied by Doppler radar. Therefore, different engineering models have been developed and used to produce microburst-like flow fields for a variety of research purposes.

Microburst-modeling methods to date can be classified into three categories, i.e. ring-vortex modeling, impinging jet modeling, and cooling source modeling. The first method has mainly focused on revealing the structure and evolution of flow patterns around the primary vortex generated in a microburst. Ivan [6] described a mathematical

model of a downburst that resolves the stream function around a ring vortex. It was reported that this model produced results resembling some of the flow patterns, particularly the primary-vortex pattern noted in field data from the JAWS project. Schultz [7] constructed a multiple vortex-ring model by using time-invariant vortex ring filaments from potential flow theory. The velocity distribution around this simulated ring vortex matched the field data of the 1985 DFW microburst reasonably well. Vicroy [8] compared three theoretical models: linear, vortex-ring, and empirical. He found that latter two types provided more favorable results than the linear model.

The impinging jet model has been widely adopted due to its simplicity and ability to produce reasonable outflow-velocity profiles. As early as in 1987, by summarizing field data collected from a series of Colorado microbursts during the JAWS project, Hjelmfelt [4] pointed out that the outflow structures were found to have features resembling those of a laboratory-simulated wall jet. Subsequently, the impinging-jet model was utilized, both numerically and experimentally, by a number of researchers for microburst studies. Selvam and Holmes [9] used a two-dimensional k-ε model to simulate impingement of a steady jet of air on a ground plane. A reasonable agreement between numerical results and field data was achieved. Holmes [10] and Letchford and Illidge [11] performed experimental studies using a jet impinging on a wall to investigate topographic effects of a microburst outflow on velocity profiles. Holmes and Oliver [12] empirically combined wall-jet velocity and translational velocity and obtained a good representation of a travelling microburst which was well correlated with a 1983 Andrews AFB microburst. Wood et al. [13] experimentally and numerically studied impinging jets over various

terrains. This study found agreement with respect to the established steady outflow at distances beyond 1.5 jet diameters from the impingement center. Choi [14] carried out both field and laboratory studies on a series of Singapore thunderstorms. Terrain sensitivity of microburst outflows was studied by comparing microburst observations at different heights and impinging jet experiments with different H/D ratios. The study produced similar trends, reflecting the impinging jet model's good capability for dealing with such problems. Chay et al. [15] conducted steady simulation and obtained good agreement with downburst wind-tunnel results. A non-turbulent analytical model was also used to study velocity-time history at a single point. Kim and Hangan [16] and Das, et al. [17] performed both steady and transient two-dimensional CFD studies using an impinging jet model, producing reasonable radial-velocity profiles and good primary-vortex representation. Sengupta and Sarkar [18] carried out laboratory and 3-D numerical simulations using an impinging jet model. Both numerical and PIV results showed good agreements with full-scale data. To physically capture transient features, Mason et al. [19] deployed a pulsed-jet model to simulate transient microburst phenomenon. The formation and evolution of the primary, successive intermediate, and trailing edge vortices were visualized and recorded. Additionally, Nicholls et al. [20], Chay and Letchford [21], Letchford and Chay [22], and Sengupta et al. [23] performed impinging jet simulations to study the effects of microburst winds on low-rise structures. Generally, the impinging jet model is driven by a momentum-forcing source without any buoyancy effects. Although the steady-state models of impinging jet flow has been

validated with field data by comparing wind velocity profiles, the transient features of an impinging jet flow compared to that of a real microburst still remains unknown.

An alternative approach using thermal cooling source was adopted by a few researchers, which puts more emphasis on the negative buoyancy and the dynamic development of the microburst. Experimentally, this method was accomplished by dropping denser fluids into less dense surroundings, which can be found in Lundgren et al. [24], Yao and Lundgren [25], and Alahyari and Longmire [26]. Nevertheless, the scale of physical modeling has remained very limited, making it almost impossible to study the wind loading effects on reasonably-scaled building models. Numerical simulations using cooling source approach involves a cooling source function, which was suggested by Anderson et al. [27]. The atmospheric full-cloud model was simplified to a space- and time-dependent cooling source function without considering the micro-physical process of a real microburst. This model was later used by Orf et al. [28] to study colliding microbursts, and by Orf and Anderson [29] to study travelling microbursts. Mason et al. [30] also investigated topographic effects on simulated downbursts using a sub-cloud model. Comparing the simulation results to their previous impinging jet modeling results, they suggested that little discrepancy was found with respect to the topographic effects despite use of two different modeling methods. Most recently, Vermeire et al. [31] compared the non-dimensional results using cooling source model and transient impinging jet model, and claimed that the impinging jet results deviated significantly from the cooling source results due to its unrealistic forcing parameters. This study used simplified impinging jet and cooling-source models and did

not compare the simulation results with the transient characteristics of the field data. More comparisons with field data and data obtained from laboratory and numerical simulations are needed to compare and validate these two models apart from improving the models themselves.

Overall, due to the scarcity of field data and the complexity of this natural phenomenon, it is of critical importance to know which modeling method is the best for microburst study, particularly from an engineering point of view. Despite significant efforts by previous researchers, very little research has been found that compares the merits and demerits of different microburst models. In the present study, a steady impinging jet model was investigated by taking point and PIV measurements. Although the time-averaged characteristics of a microburst have been studied previously, its transient behavior and hence its dynamic features have not been fully explored. To complement the experimental study of a steady-impinging jet model, the transient behavior of an impinging jet model was studied numerically and compared with a simplified cooling source model. All results were compared to field data collected in the NIMROD and JAWS projects. Finally, the merits and demerits of these modeling methods were analyzed and concluded to provide references for use in future studies.

2. Experimental Setup

The microburst was physically generated by a steady impinging jet flow simulator in the WiST (Wind Simulation and Testing) Laboratory at Iowa State University, shown in Figure 1. The jet flow is produced constantly by a fan on the top and impinges on a wooden plate to form a steady wall-jet flow field. The diameter of the nozzle is about

0.6m (2 feet). The distance between the nozzle exit and the plate representing the ground plane is adjustable from 1 to about 2.3 times the diameter (D) of the nozzle (0.75 to 7.5D in nature). The fan at the top of the simulator is driven by a step motor (RELIANCE ELECTRIC Duty-Master, Model number P2167403L).A honeycomb and several screens are placed at the exit of the nozzle to produce a uniform velocity across the exit and reduce the turbulence of the issuing jet. The axial velocity of the jet was measured at one nozzle diameter underneath the nozzle exit at different fan speeds, and the distribution across the jet was found to be sufficiently uniform, as shown in Figure 2. The mean jet velocity under the nozzle exit was $V_{jet} \approx 6.9$m/s.

Velocity measurements were first performed at different r/D locations (i.e. r/D=1, 1.5, 2, 2.5) using three-component cobra-probe (TFI Pvt. Ltd.), where r is the radial distance from the center. Using this multi-hole probe, three components and the overall magnitude of the velocity vector can be measured at the same time. At each r/D location, measurements were taken at 38 points ranging from 0.25 inches to 7 inches above the ground plane. For each point, the data was collected at a frequency of 1250 Hz for 10 seconds. The measurement error was within ±0.5m/s according to the specified accuracy of the cobra-probe. However, the probe could only resolve velocity information for the incoming flow within ±45 degrees of the probe's axis. Therefore, for the shear layer of the wall jet flow, which is dominated by large-scale vortex structures, the accuracy of statistical results within the shear layers is significantly reduced due to reduced quantity of valid data gathered by the probe. PIV (Particle Image Velocimetry) technique was used (schematic is shown in Figure 3) to capture whole-field information of the near-

ground wall jet flow. The coordinate system indicating three velocity components was also shown in Figure 3. The flow was seeded with 1-5 μm oil droplets and illumination was provided by a double-pulsed Nd:YAG laser (NewWave Gemini 200) adjusted on the second harmonic frequency and emitting two 200 mJ laser pulses at a wavelength of 532 nm and with a repetition rate of 10 Hz. The laser beam was shaped into a laser sheet (thickness ~1 mm) by using a set of mirrors along with spherical and cylindrical lenses. A high-resolution (1365×1024 pixels) charge-coupled device (CCD) camera with axis perpendicular to the laser sheet was used for PIV image acquisition. The CCD camera and the double-pulsed Nd:YAG lasers were connected to a workstation via a digital delay generator that controlled the timing of both the laser illumination and the image acquisition.

The CCD camera was focused on a measurement window of 207×152 mm size such that a total of 14 windows were used to cover the entire microburst outflow region's areas of interest. The layout of these investigation windows is illustrated in Figure 4. To ensure that results from different windows match each other reasonably well, 30% overlaps were established between each window and its vertically-adjacent window. Instantaneous PIV velocity vectors were obtained using a frame-to-frame cross-correlation technique involving successive frames of patterns of particle images in an interrogation window with 32×32 pixels and an effective overlap of 50% to satisfy the Nyquist criterion. After the instantaneous velocity vectors were determined, time-averaged quantities such as mean velocity, turbulent-velocity fluctuations, normalized turbulent kinetic energy, and Reynolds stress distributions were obtained from a cinema

sequence of 500 frames of instantaneous velocity fields for each case. The measurement uncertainty level for the velocity vectors was estimated to be within 2.0%, and that of the turbulent velocity fluctuations and turbulent kinetics energy was about 5.0%.

3. Numerical Simulation

3.1 Computational Parameters

An axisymmetric unsteady RANS (Reynolds Averaged Navier-Stokes) model was used in this study using commercially available software FLUENT 12.1 (ANSYS Inc.). Although LES has the well-known ability to resolve large-scale turbulent structures and simulate time-dependent turbulent flows, the application of LES requires a very fine mesh and sufficiently small time steps. Given the large geometric scale of the computational domain, use of LES could be extremely expensive for this problem with relatively high-Reynolds-number. The objective of this numerical simulation, however, was to investigate the differences of macro-scale flow features between two modeling methods and compare these features with the field data. Therefore, unsteady RANS or URANS model was used because it is proved to be economic and effective for this study. In the URANS simulation, the ensemble-averaged velocities, denoted by $\langle u \rangle$, are still functions of time, so the Reynolds decomposition of velocity can be expressed as $u = \langle u \rangle + u' = \bar{u} + u'' + u'$, where $\bar{u}$ is the time-averaged velocity, u'' is the resolved unsteadiness of the mean flow and u' is the fluctuating component of velocity. Therefore, the unsteady features of the ensemble-averaged flow field are resolved, making URANS an effective tool for solving only macro-flow problems.

The governing equations for the numerical simulation in Cartesian coordinate system are given as follows:

Continuity

$$\frac{\partial \rho}{\partial t} + \frac{\partial}{\partial x_i}(\rho u_i) = 0 \tag{1}$$

Momentum

$$\frac{\partial}{\partial t}(\rho u_i) + \frac{\partial}{\partial x_j}(\rho u_i u_j) = -\frac{\partial p}{\partial t} + \frac{\partial}{\partial x_j}\left[\mu\left(\frac{\partial u_i}{\partial x_j} + \frac{\partial u_j}{\partial x_i} - \frac{2}{3}\delta_{ij}\frac{\partial u_k}{\partial x_k}\right)\right] + \frac{\partial}{\partial x_j}\left(-\rho\overline{u_i' u_j'}\right) + f_i \tag{2}$$

The Reynolds stress term $-\rho\overline{u_i' u_j'}$ needs to be modeled to close the equation. Generally, the Reynolds stress term was modeled based on Boussinesq hypothesis as $-\overline{u_i' u_j'} = 2\nu_t S_{ij} - \frac{2}{3}k\delta_{ij}$, where $S_{ij} = \frac{1}{2}\left(\frac{\partial u_i}{\partial x_j} + \frac{\partial u_j}{\partial x_i}\right)$ and ν_t is newly introduced turbulence eddy viscosity term. f_i is the gravitational force term, which was considered in the cooling source model but set to zero in the impinging jet model.

For the cooling source model, the energy equation was also included

$$\frac{\partial}{\partial t}(\rho E) + \frac{\partial}{\partial x_i}\left(u_i(\rho E + p)\right) = \frac{\partial}{\partial x_i}\left(K_{eff}\frac{\partial T}{\partial x_i}\right) + Q_s \tag{3}$$

where $Q_s = Cp \cdot Q(x, y, t)$ is a source term which will be discussed later (Cp is the specific heat of air).

In the present study, the standard $k-\varepsilon$ model was used to solve the turbulence eddy viscosity term. Such models are widely used due to their simplicity, robustness, and reasonable accuracy over a wide range of turbulent flows. The turbulence eddy viscosity was defined as $\nu_t = \frac{\mu_t}{\rho} = C_\mu \frac{k^2}{\varepsilon}$, where k is turbulence kinetic energy and ε is its rate of dissipation. Transport equations for k and ε could be found in Launder and Spalding [32] and the default model parameters were set in FLUENT during the simulation ($C_{1\varepsilon} = 1.44$, $C_{2\varepsilon} = 1.92$, $C_\mu = 0.09$, $\sigma_k = 1.0, \sigma_\varepsilon = 1.3$). A second order upwind scheme was used for solving the continuity and momentum equations and T.K.E. and turbulent dissipation rate were both determined using the Quadratic Upstream Interpolation for Convective Kinematics (QUICK) scheme. The SIMPLE scheme was used to provide pressure-velocity coupling. For the transient formulation, a second-order implicit scheme was adopted.

Both impinging jet and cooling source models were solved on a 2D axisymmetric domain. As shown in Figure 5 (a), only w velocity in z direction and u velocity in r direction were considered in this simulation and swirling velocity was zero. To simulate the realistic microburst phenomena while keeping the computational domain in consideration, the jet diameter (D) and the jet-nozzle height from ground plane (H) were each set as 2,500m such that the H/D ratio was 1. These figures were well within the

range of diameter D and H/D for a microburst, known to be varying between 400 to 4000m and 0.75 to 7.5, respectively. For the steady impinging jet, a velocity inlet combined with an incompressible flow condition was used. For the cooling source model, a specific cooling function covering the inlet region was incorporated by adding a source term into the energy function. This cooling function will be discussed in detail later. A pressure inlet and compressible flow condition were used to resolve a density change induced by the cooling function.

All simulations in this study were solved on a structured grid with quadrilateral cells. At the wall boundary, the distance between the first row of grids and the ground was confined to be less than 1m. The mesh was gradually stretched as it moved away from the ground-plane boundary and the cell spacing became constant above approximately 50m from the ground level, as shown in Figure 5 (b). A study of mesh independent was carried out separately before settling on the mesh. As shown in Figure 6, all the radial velocity profiles for the impinging-jet model (at the r/D=1 location at the 470 second time step) tend to converge to the same line as the number of cells increases. Therefore, a 1-million-cell grid was chosen and it should be safe to believe that the results are independent of mesh conditions.

3.2 Cooling Function

A cooling source model was simulated by adding a spatial and temporal cooling source to the computational domain, as shown in Figure 5. This sub-cloud cooling model was suggested by Anderson et al. [27]. This effect is achieved by adding a spatio-temporal source term to the energy equation described by:

$$Q(x,y,t)=\begin{cases} g(t)\cos^2 \pi R & for\ R<\dfrac{1}{2} \\ 0 & for\ R>\dfrac{1}{2} \end{cases} \qquad R^2=\left(\frac{x-x_0}{h_x}\right)^2+\left(\frac{y-y_0}{h_y}\right)^2$$

where g(t) = $A\sin^2(\pi t/2\tau)$ K/s is a time-dependent coefficient which ramps up from 0 to a maximum (A= -0.1 K/s) in the first 120 seconds and then g(t) = $A\sin^2(\pi(540-t)/2\tau)$ gradually decreases to 0 in the interval from 420 s to 540 s. τ is a time constant which was set to be 120s in the present study. Between 120 s and 420s, g(t) was kept constant at a maximum intensity of g(t)=A, which is larger than that described in Anderson et al. [27] to obtain more significant cooling effects. R is non-dimensional radius (0 to 1) of the cooling source (elliptical in shape) determined by position of the geometric center (x_0, y_0) of the ellipse (x, y) and the major and minor half axes of the ellipse, h_x and h_y. Mason [33] pointed out that changing the temporal term of the cooling function almost did not affect the normalized velocity profiles, while the geometric shape of the cooling source have a great influence on the results. However, the choice of the current simplified cooling function was made by Anderson [27] based on a comparison of the numerical full cloud model and the real field events, and it was further utilized by Orf et al. [28] based on the microphysical calculations for a downburst producing storm and by Vermeire et al. [31] for a model comparison. Therefore, the cooling function used here, though simplified, could be seen as a reasonable approximation. Figure 7 illustrates the entire life-cycle of a simulated microburst event visualized by the evolution of the temperature field of the cooling source model.

3.3 Scaling Parameters

To compare the transient features of the two numerical models, the flow-field variables of the models should be normalized to common critical parameters. Since the forcing mechanism is intrinsically different between the impinging jet model and the cooling source model, it was decided not to directly match the results based on the computational time and length scales.

As is widely known, the most prominent feature of a microburst is the primary vortex ring that is known to produce extreme wind velocity. Therefore, the time scale T_0 was taken here as the computational time in each of the two modeling results at which maximum velocity (V_0) occurred. The velocity parameter was taken as V_0 and the length scale was calculated as $L_0 = V_0 T_0$. The corresponding Reynolds number would be

$$\mathrm{Re} = \frac{V_0 L_0}{\nu}$$

Numerical scaling parameters for this case study are given in Table 1. It can be seen that the Reynolds numbers with the characteristic length L_0 are of the same order if using this scaling method

Table 1. *Scaling parameters for the numerical analysis*

	V_0	T_0	L_0	Re
Impinging Jet	V_{01}=45.9 m/s	T_{01}=470s	$L_{01}=2.16\times10^4$m	6.55×10^{10}
Cooling Source	V_{02}=67.5 m/s	T_{02}=260s	$L_{02}=1.76\times10^4$m	7.84×10^{10}

4. Results and Discussions

4.1 The Steady Impinging Jet Model

4.1.1 Overall/componential Velocity and Turbulence Intensity Profiles

A well-developed steady impinging jet flow normally consists of three flow regions: downdraft region, stagnation region and the wall jet region. The flow field of the wall jet region is usually more complex than the other two flow regions and of greater importance for engineering. Figure 8 shows the total velocity (U) and velocity components (u, v, w) normalized by mean jet velocity (V_{jet}) at different radial locations r/D= 1, 1.5, 2, and 2.5, where r/D is the radial distance from the center normalized by the jet diameter. The vertical distance from the ground (z) was normalized by the jet diameter (D). Here, u denotes the mean velocity in the radial direction ($U = \sqrt{u^2 + v^2 + w^2}$), while v and w denote the mean velocity in tangential and axial directions respectively, of the impinging-jet flow

Generally, the overall velocity distribution in vertical direction shows a wall-jet shape Maximum velocity was found at a height around z/D= 0.05 (corresponding to 20m-200m above ground level in a real microburst event). As radial locations moved from r/D=1 to 2.5, maximum velocity decreased and the slope of velocity with elevation also reduced significantly. The radial velocity (u) was found to be dominant for all radial locations. However, it is interesting to observe that a considerable increase of the magnitudes of v and w component occurred at r/D=1 from the ground to z/D=0.1. This phenomenon was possibly related to the channeling effect between the primary vortex

and the secondary vortex, which has been mentioned by others [16, 17]. At a radial location around r/D=1, a counter-rotating vortex, i.e. the secondary vortex, was possibly generated at the ground due to wall friction. The primary and secondary vortices could narrow down the flow path and stretch the flow between them, causing a locally accelerated flow, and also add a positive w velocity component by lifting up the local flow. Also affected by this vortex pairs, the trend of tangential velocity v at r/D=1 was more complicated than other radial locations where tangential velocities were almost zero.

Figure 9 shows the overall and the three turbulence intensity components at different radial locations, calculated by normalizing the root-mean-square (RMS) of the velocity fluctuation by the local mean of the resultant velocity (U=$\sqrt{u^2 + v^2 + w^2}$). Generally, it is clear that the turbulence intensity first decreased as the height increased from z/D=0 to approximately z/D=0.05 (where peak velocity occurred). However, it increased significantly above z/D=0.1 and reached a constant value above z/D=0.25 approximately. This turbulence profile is dramatically different from that of an atmospheric boundary layer, where turbulence intensity is larger near ground due to friction and disturbances. As the radial distance from the center increased, turbulence intensity near ground increased notably and the slope of the curve became milder, indicating enhanced flow mixing and reduced wind speed. Furthermore, the w-component turbulence intensity behaved differently from that of other components. Fluctuation of the vertical component was found significantly lower than those of other components at locations very near the ground due to the wall effects. However, with the

height increased, fluctuation of w component increased dramatically and contributed the largest at r/D=1.0 and r/D=1.5. Nevertheless, for r/D=2 and larger, the peak value of the w component turbulence intensity dropped and eventually followed the same trends of other components. The significant fluctuation in vertical direction might be closely related to the shedding vortices within the shear layer, which will be further discussed later.

4.1.2 Whole-field Flow Characteristics

The ensemble-averaged PIV results are presented in Figure 10, which shows distributions of velocity and turbulence in the wall-jet region. It can be seen that the jet flow expanded as it approached the ground. As shown in Figure 10 (a), radial velocity u was almost zero at the center of the stagnation region. As the flow diverged away from the core center, it accelerated at first, reached its maximum speed at the location of r/D ≈1.0, and then slowed down gradually further downstream. A high velocity region with a maximum magnitude of more than u/V_{jet}=1.1 (V_{jet}≈6.9) covered a considerable area from r/D=0.7 to r/D=1.0. The depth of outflow expanded as flow travelled radially, illustrated by the shape of the contour. In Figure 10 (b), a region of accelerated flow is seen where w changes to positive values from negative values (downward direction) in the downdraft region.

Figure 10 (c) and (d) show the turbulence kinetic energy and Reynolds shear stress, which were normalized by the squared jet velocity (V_{jet}^2). It can be seen clearly that the turbulence level within the core region of the steady impinging jet (i.e., r/D≤0.5) is quite low. The turbulence intensity was found to increase greatly in the outflow region of the

steady impinging jet (i.e., r/D>1.0). A region with very high turbulence intensity (i.e., much higher turbulence kinetic energy) was found to exist at the downstream location of r/D≈1.5~2.0. Generally, the turbulence was generated from two sources: the interface between the jet flow and the boundary layer on the ground. Turbulent flow arising from these two sources then mixed to form a large turbulence region in the wall jet flow. In the Reynolds-shear-stress contour, turbulence from these two sources can be easily distinguished. The negative regions were caused by a negative velocity gradient in the vertical direction and therefore represented the turbulent flow formed at the interface due to the strong shear. In contrast, the red region showed the turbulence developed in the wall-jet boundary layer.

4.1.3 Time-domain Characteristics of The Steady Impinging Jet

In the previous section, ensemble-averaged information of the microburst outflow was shown in detail. Turbulence mixing was remarkable in the shear layer due to flow instability. However, it was found that turbulence in shear layer actually contains large-scale movement of the periodically-shed vortices. Figure 11 shows Fast Fourier Transformations of the velocity time history at a height of z/D=0.2, which could be considered within the shear layer of the wall-jet flow. It can be seen in Figure 11 (a) that, instead of complete randomness, a low-frequency component near f≈16 Hz dominated the spectrum at r/D=1, corresponding to a Strouhal number St=1.63 ($St = fD/V_{jet}$). This number is very close to that obtained in O'Donovan and Murray [34]. As the flow moved to r/D=2 (Figure 11 (b)), the dominant frequency and its magnitude decreased as the flow velocity decreased and the large-scale structure broke down into many smaller

ones. This phenomenon was further verified in Figure 12, which presents a single snapshot of the instantaneous flow in the investigated window 2B. Vorticity was calculated as $\frac{\partial w}{\partial x} - \frac{\partial u}{\partial z}$. In this figure, two primary vortices could be clearly visualized at the flow interface. Therefore, if the generation and expansion of the primary vortex is assumed to be the major characteristic of a natural microburst event, the steady impinging jet flow could be seen as a combination or an ensemble-average of a series of microburst events with sufficiently long period.

In Figure 13, the averaged velocity profiles at the maximum velocity locations were extracted and compared with the field data and the previous numerical and experimental results. In this plot, the vertical distance 'z' was non-dimensionalized by 'b', which denotes the height where the radial wind speed (u) is half of its maximum (u_{max}) and radial velocity u is normalized by u_{max}. It can be seen in the plots that there is very good agreement between these measurements and the field data, particularly for H/D=2. It should also be noted that considerable discrepancies was present between the point-measurement results and the PIV results over z/b=1.0. These discrepancies may arise from the measurement error of the cobra-probe, whose accuracy was dramatically decreased in the shear layer where flow direction rapidly changes.

Therefore, even though the time-dependent information is neglected in the steady impinging jet model, the similarity of the velocity profiles suggests that it could still be used as a valid simulation model for quasi-steady study.

4.2 Numerical Simulation: Comparison of Transient Characteristics of the Impinging Jet Model and the Cooling Source Model

4.2.1 Comparison of Velocity and Surface Pressure Distribution

To obtain an intuitive sense of the differences in the transient features of impinging jet model and cooling source model, the evolution of velocity fields of the two models was first analyzed and compared. Velocity was normalized by the maximum wind speed obtained during each simulation, namely V_{01} and V_{02}. Figure 14 shows the contours of normalized radial velocity component for two modeling methods at different scaled time. The four contours were organized by matching the locations of the first vortex core, i.e. before touching the ground, at r_{max}/D, $1.5r_{max}/D$, and $2r_{max}/D$, where r_{max} is the radial location where the maximum velocity occurred. As shown in Figure 14 (a1), the impinging jet produced a pair of negative and positive velocity contours, i.e., a primary vortex, before the flow touched the ground. As the primary vortex touched the ground at T/T_{01}=1.00, the outflow was stretched and accelerated within the channel between the primary vortex and the secondary vortex as caused by ground friction. These vortices can be clearly seen in Figure 16. The spatial and temporal maximum velocity of each model was found at this time to accompany the primary vortex. As the vortex traveled and decayed radially, new vortices were found to continuously form at the shear layer between the jet flow and the ambient air. These subsequently-formed vortices then produced a series of large-velocity regions that were comparable with the maximum velocity, as shown in Figure 14 (a3 and a4).

The radial-velocity contours of the cooling source model exhibited significant differences from those of the impinging jet model. In contrast to the case of impinging jet model, no significant reverse flow occurred at the jet-ambient interface before the

flow touched the ground as shown in Figure 14 (b1). Maximum velocity was found at T/T_{02}=1.00 accompanied with the traveling primary vortex as shown in Figure 14 (b2). Due to a different forcing parameter and gravitational effects, the velocity contour was apparently more compressed near the ground than that of the impinging jet model. As the outflow traveled radially, the reverse-flow velocity inside the primary vortex was found to be more significant than that of the impinging jet model. Most importantly, no follow-up vortices developed after the primary vortex. The primary vortex accompanied with the large velocity region decayed with time and eventually died out after the strength of the cooling source decreased to zero. As shown in Figure 16, no secondary vortex was found at the time when maximum velocity occurred.

The normalized axial velocity contours produced by the two modeling are presented in Figure 15, with a same time sequence as Figure 14. It can be seen that the axial velocity distributions in the downdraft core of the two models were different. For the impinging jet model, the flow exhausted from the jet exit remained constant until it started to decelerate towards the ground at a height of z/D=0.6. However, for the cooling source model, flow accelerated due to gravity and reached maximum at a height of z/D=0.3 before it slowed down towards the stagnation point. As the flow expanded radially, it can be seen that the axial velocity component induced by the primary vortex was significant in both two cases. Particularly in the cooling source model, the maximum axial velocity was found to have same magnitude with the maximum radial velocity. This considerable axial velocity component is crucial for the safety of aircrafts and civil structures. However, this time-dependent phenomenon apparently cannot be

studied using steady impinging jet model and usually is hard to be detected by a Doppler radar in the field.

Generally, differences in velocity fields depicted above mostly resulted from the formation and transportation of the primary vortex. As discussed earlier, the primary vortex in the impinging jet model formed at early downdraft stage due to strong shear at the interface. However, the formation of the primary vortex in the cooling source model was a completely different process. Figure 17 shows the density map of the cooling source model at different time steps. It can be seen clearly that the leading edge of the denser air gradually rolled up as it traveled in radial direction. Therefore instead of being transported from the upstream in the impinging jet model, the primary vortex in the cooling source model actually generated locally at the leading edge of the outflow and resembled the features of a gravity current head [35].

Differences of underlying physics can be also seen from the surface pressure distributions in Figure 18, where pressure coefficients of transient impinging jet (at T/T_{01}=1), cooling source model (at T/T_{02}=1) and the experimental steady impinging jet were compared. Pressure coefficient is defined as $Cp_{jet} = (P - P_{atm})/0.5\rho V_{jet}^2$ for both transient and steady impinging jet, where ρ is constant and V_{jet} is constant jet velocity. For cooling source model, maximum ρ and V_{jet} at T/T_{02}=1 were chosen to be the maximum along the central axial axis from varying density and velocity distributions. A good match between the results of transient and steady impinging jet was found except that a large negative pressure was found at r/r_{max}=1 for the transient impinging jet

model. Due to the existence of secondary vortex in the transient impinging jet, a smaller peak of negative pressure could also be seen at this time step. Similar minimum pressure was found for both transient impinging jet and cooling source models corresponding to the location of the primary vortex of the two models. However, a large deviation was seen at the center of the flow field. For both transient and steady impinging jet, Cp_{jet} is equal to 1 at the center due to the stagnation of jet flow, whereas a much larger Cp_{jet} was found at the center for the cooling source model due to the contribution of the hydrostatic pressure of the denser air. Therefore, a much higher pressure load would be expected when a civil-structure model was located within the core region, if the microburst is simulated using cooling source model. However, the transient loading effects outside the core region caused by the primary vortex could be similar for these two modeling methods.

4.2.2 Comparison of the Primary Vortex Trajectory

Based on discussion in previous sections, the most dominant feature of the transient microburst flow is the primary vortex. Besides the formation of the primary vortex, it is also of great importance to understand how primary vortices move in the expanding outflow for transient impinging jet and cooling source models.

Figure 19 shows the height of the primary vortex core as a function of time for two models. The vortex core was located by tracking the lowest pressure point within the primary vortex. Because of strong instability at the interface of the wall-jet flow, the primary vortex descending from a high-altitude position in the impinging jet model was found to oscillate in the vertical direction as it expanded radially. However, the primary

vortex in the cooling source model appeared rather stable as it moved outwards. Because of gravity, the vortex was also found to be much closer to the ground.

The radial-direction trajectories of the primary vortex cores were compared with field data gathered from the JAWS project [5] in Figure 20. To make this comparison valid, the field data in this study was re-normalized to ensure that $r/r_{max}=1$ corresponds to the normalized time $T/T_0=1$, where T_0 represents T_{01} for the impinging jet model and T_{02} for the cooling source model respectively. It should be noted that the field data does not represent the actual vortex core movement, but rather the expansion of the gust front of the microburst. Hence, it is assumed here that the vortex expansion is equivalent to or similar to the gust front expansion. From this figure, it is clear that both the impinging jet model and the cooling source model resulted in a linearly-expanded primary vortex, similar to real microburst events in nature. The slope of each curve represents the relative expansion speeds corresponding to the initial conditions of each of the real or simulated microburst events, which could be different from case to case.

4.2.3 Comparisons with the Field Data

Based on the previous discussions, the differences between the two models were significant and considerable simplifications were made in both two modeling methods. To better serve the research purpose, a comparison with field data is necessary to evaluate the validity of different modeling methods.

In Figure 21, time series of the radial velocity profiles were compared with the time history of a single microburst event occurring during the JAWS project [5]. In this typical microburst event, the maximum velocity increased dramatically and reached its

peak at time 16:48. The maximum velocity location moved away from the center as the primary vortex expanded. This time-series data covered 9 minutes of the entire event. However, matching the simulation results and the field data in time dimension is difficult due to the random nature of the microburst event. This comparison was made by matching the maximum velocity at $T/T_0=1$ of two modeling results. Velocity was normalized by the maximum velocity at $T/T_0=1$ and radial distance was normalized by r_{max}, which stands for the radial distance where maximum velocity occurred in the field and experiment respectively. It can be seen that both models provided reasonably good estimations of dynamic features of the outflow expansion within the range of the maximum velocity location. Nevertheless, the prediction is poor beyond the maximum velocity location, probably due to the complexity of the atmospheric conditions in a real microburst event.

A transient microburst event is actually a four dimensional problem, which does not only evolves in space but also changes rapidly in time domain. From an engineering point of view, the most interesting part is to examine the maximum wind which could be induced by the microburst and the velocity distribution at the maximum wind condition. However, it should be admitted that the wind profiles at the maximum condition is highly dependent on when and where the data was extracted particularly in a transient simulation. Therefore in order to eliminate the uncertainty, data was extracted from the spatial and temporal vicinity of the computed maximum wind condition and compared with the field data and the results of previous studies in Figure 22. The field data are usually collected by Doppler radar within a very short time period and a certain spatial

range. Hence, from whole-event point of view, the field data could still be seen as a snapshot of the entire microburst event. Figure 22 (a) shows the radial velocity profiles at the maximum velocity time and in the vicinity of the maximum velocity location for both models. It is evident that the transient impinging jet data deviated considerably from both the steady impinging jet data and the field data, while the cooling source resulted in an instantaneous velocity profile similar to that of the field data up to the boundary-layer height (b). This result was further verified by comparing with the data of the previous studies. Vermeire et al. [31] obtained a similar velocity profile using the impinging jet model which had a large discrepancy compared with the field data, while the profile generated by cooling source function showed a good match. Mason [33] also generated a maximum-storm velocity profile following the trend of the field data. Slight deviation under z/b=1 is possibly due to the secondary vortex reported in his research caused by the surface roughness, which were not considered in this study. Similar results could be found in Figure 22 (b), in which the velocity profiles were compared by taking data from the vicinity of the maximum velocity time.

These results imply that because of the similar trajectories of the primary vortex in radial direction, transient impinging jet and cooling source models were both valid in terms of predicting the time-dependent velocity distribution along radial direction. However, due to the intrinsic differences of the formation and structure of the primary vortices, the maximum velocity profiles at the critical location of two models were dramatically different. Apparently, the “rolling-up” type primary vortex generated in a

cooling source model is more similar to the field event than that of an impinging jet model.

5. Concluding Remarks

In the present study, the microburst outflow was first simulated experimentally using steady impinging jet model. Both point measurements and whole-field measurements (PIV) were conducted to study the flow field. Results showed a detailed picture of overall/componential velocity and turbulence within a steady impinging jet flow. Comparisons suggested that the wind profile at the critical location matched well with the field data and the previous research. FFT of the velocity time-history and instantaneous PIV results implied the turbulence in the shear layer was dominated by shedding vortices at a low frequency ($St = fD / V_{jet} = 1.63$). Therefore, it was suggested that the steady impinging jet model could be seen as a statistical average of a series of simulated microburst events.

Numerical simulations were performed to compare different transient outflow characteristics between the transient impinging jet model and the cooling source model. The comparisons of velocity contours and vortex trajectories between the impinging jet model and the cooling source model revealed several different characteristics induced by intrinsically different underlying physics. While the flow patterns in the impinging jet model were dominated by instability in the shear layer, the cooling source model produced a relatively smooth outflow resembling the features of gravity current. Due to the strong shear at the interface, a primary vortex was found to form immediately after

the flow was initiated in the transient impinging jet model. As the primary vortex touched the ground and expanded radially, follow-up vortices were continuously generated and produced a series of large-velocity regions that were comparable with the maximum velocity. However, for the cooling source model, the primary vortex was found to be formed only after the cooled air descended to the ground. Denser air was found to roll up to form the primary vortex at the leading edge of the outflow. No follow-up vortices like those of the impinging jet model were found.

Surface pressure distributions were also investigated. While the negative pressures induced by the primary vortices was similar between the two models, the cooling source model produced much higher pressure in the core region due to the extra contribution from the hydrostatic pressure. A secondary peak of negative pressure was found in the transient impinging jet corresponding to the secondary vortex found at the maximum-velocity time.

The trajectories of the primary vortex in these two models show distinct features. In impinging jet model, the primary vortex propagated in a wavy fashion whereas in the cooling source model it remained at a rather constant height. The transient expansion of the primary vortex in these two models, though exhibiting different speeds, resembles the linear characteristic of the natural events.

Comparisons were performed between transient velocity profiles of each of the two modeling methods and the field data. Results indicated that, transient impinging jet and cooling source models were both valid in terms of predicting the time-dependent velocity distribution along radial direction. However, in terms of reproducing the

instantaneous radial-velocity profile at the maximum wind condition, the impinging jet model deviated from the field data, while the cooling source model provided more reasonable agreement.

The merits and demerits of each modeling method are summarized as follows:

1) The steady impinging jet model provided an averaged flow field with a reasonable radial-velocity profile at the critical location (maximum velocity location), but it lacks time-dependent information. It is simple to simulate and convenient for quasi-steady wind load test on laboratory models.

2) The transient impinging jet model provided a good simulation of the dynamic properties of the primary vortex expansion, but it failed to provide the instantaneous radial velocity profile resembling the field data at the critical location. Like the steady case, it is relatively easy to simulate in a laboratory with a reasonable scale.

3) The cooling source model provided a good simulation of the instantaneous radial velocity profile similar to the field data at the critical location, and also gave a reasonable representation of the transient expansion of the primary vortex. Although successfully simulated numerically, the cooling source model is difficult to simulate in the laboratory environment, particularly with a sufficient scale to conduct wind load tests on scaled laboratory models.

In conclusion, since field data is rather scarce, the truth regarding real microbursts in nature is far from being fully-understood. Therefore, from an engineering point of view, the choice between the uses of the three microburst modeling methods should depend on the purpose. Future studies related to microburst modeling should attempt to take

advantage of certain aspects of simplicity and accuracy while avoiding the drawbacks of each modeling method.

Acknowledgments

This study is funded by the US National Science Foundation (NSF) under award number CMMI-1000198. The authors would like to thank NSF for the financial support and acknowledge the help of Bill Rickard, department technician, and Nick Krauel, undergraduate student, at Iowa State University in building test models and experimental setups.

References

[1] Fujita TT. The downburst: microburst and macroburst. University of Chicago Press, 1985.

[2] Fujita TT. Spearhead echo and downburst near the approach end of John F. Kennedy runway, New York City: SMRP Res. Pap. 1976.

[3] Wilson JW, Roberts RD, Kenssiger C, McCarthy J. Microburst wind structure and evaluation of Doppler radar for airport wind shear detection. J. Climate and Applied Meteor. 1984; 23: 898-915.

[4] Hjelmfelt MR. The microbursts of 22 June 1982 in JAWS. J. Atmospheric Sciences, 1987; 44(12):1646-1665.

[5] Hjelmfelt MR.: Structure and life cycle of microburst outflows observed in Colorado. J. Applied Meteorology 1988; 27(8): 900-927.

[6] Ivan M. A ring-vortex downburst model for flight simulations. Journal of Aircraft, 1986; 23(3): 232-236.

[7] Schultz T. Multiple vortex ring model of the DFW microburst. Journal of Aircraft, 1990; 27: 163-168.

[8] Vicroy D. Assessment of microburst models for downdraft estimation. Journal of Aircraft, 1992; 29(6):1043-1048.

[9] Selvam RP, Holmes JD. Numerical simulation of thunderstorm downdrafts. J. Wind Eng. and Ind. Aerodyn., 1992; 44(1-3): 2817-2825.

[10] Holmes JD. Modelling of extreme thunderstorm winds for wind loading of structures and risk assessment. In: Larson A, Larose GL, Livesey FM, editors. Wind engineering into the 21st century. Rotterdam: Balkema, 1999:1409–15.

[11] Letchford CW, Illidge G. Turbulence and topographic effects in simulated thunderstorm downdrafts by wind tunnel jet. In: Larson A, Larose GL, Livesey FM, editors. Wind engineering into the 21st century. Rotterdam: Balkema, 1999:1907–12.

[12] Holmes JD, Oliver SE. An empirical model of a downburst. Engineering Structures, 2000; 22:1167-1172.

[13] Wood GS, Kwok CS, Motteram NA, Fletcher DF. Physical and numerical modelling of thunderstorm downbursts. J. Wind Eng. and Ind. Aerodyn. 2001; 89: 535–552.

[14] Choi ECC. Field measurement and experimental study of wind speed profile during thunderstorms. J. Wind Eng. and Ind. Aerodyn. 2004; 92: 275-290.

[15] Chay MT, Albermani F, Wilson R. Numerical and analytical simulation of downburst wind loads. Engineering Structures, 2005; 28: 240-254

[16] Kim J, Hangan H. Numerical simulation of impinging jets with application to downbursts. J. Wind Eng. and Ind. Aerodyn. 2007; 95: 279-298.

[17] Das KK, Ghosh AK, Sinhamahapatra KP. Investigation of the axisymmetric microburst flow field. J. Wind and Eng. 2010; 7: 1-15.

[18] Sengupta A, Sarkar PP. Experimental measurement and numerical simulation of an impinging jet with application to thunderstorm microburst winds. J. Wind Eng. and Ind. Aerodyn. 2008; 96: 345-365.

[19] Mason MS, Letchford CW, James DL. Pulsed wall jet simulation of a stationary thunderstorm downburst, Part A: Physical structure and flow field characterization. J. Wind Eng. and Ind. Aerodyn. 2005; 93: 557-580.

[20] Nicholls M, Pielke R, Meroney R. Large eddy simulation of microburst winds flowing around a building. J. Wind Eng. and Ind. Aerodyn. 1993; 46: 229-237.

[21] Chay MT, Letchford CW. Pressure distributions on a cube in a simulated thunderstorm downburst, Part A: stationary downburst observations. J. Wind Eng. and Ind. Aerodyn. 2002; 90: 711-732.

[22] Letchford CW, Chay MT. Pressure distributions on a cube in a simulated thunderstorm downburst, Part B: moving downburst observations. J. Wind Eng. and Ind. Aerodyn. 2002; 90: 733–753.

[23] Sengupta A, Haan FL, Sarkar PP, Balaramudu V. Transient loads on buildings in microburst and tornado winds. J. Wind Eng. and Ind. Aerodyn, 2008; 96: 2173-2187.

[24] Lundgren TS, Yao J, Mansour NN. Microburst modeling and scaling. J. Fluid Mech. 1992; 239: 461-488.

[25] Yao J, Lundgren TS. Experimental investigation of microbursts. Experiments in Fluids, 1996; 21:17–25.

[26] Alahyari A, Longmire EK. Dynamics of experimentally simulated microbursts. AIAA Journal, 1995; 33 (11): 2128-2136.

[27] Anderson JR, Orf LG, Straka JM. A 3-D model system for simulating thunderstorm microburst outflows, Meteor. Atmos. Phys., 1992; 49: 125–131.

[28] Orf LG, Anderson JR, Straka JM. A Three Dimensional Numerical Analysis of Colliding Microburst Outflow Dynamics. J. Atmospheric Sciences, 1996; 53(17): 2490-2511.

[29] Orf LG, Anderson JR. A Numerical Study of Traveling Microbursts. Monthly Weather Review, 1999; 127: 1244-1258.

[30] Mason MS, Wood GS, Fletcher DF. Numerical investigation of the influence of topography on simulated downburst wind fields. J. Wind Eng. and Ind. Aerodyn. 2010; 98: 21-33.

[31] Vermeire BC, Orf LG, Savory E. Improved modelling of downburst outflows for wind engineering applications using a cooling source approach. J. Wind Eng. and Ind. Aerodyn. 2011; 99(8): 801-814.

[32] Launder BE, Spalding DB. The numerical computation of turbulent flows. Computer Methods in Applied Mechanics and Engineering, 1974; 3:269-289.

[33] Mason MS, Wood GS, Fletcher DF. Numerical simulation of downburst winds. J. Wind Eng. and Ind. Aerodyn. 2009; 97: 523-539.

[34] O'Donovan TS, Murray DB. Jet impingement heat transfer--Part II: A temporal investigation of heat transfer and velocity distributions, Int. J. Heat Mass Transfer 2007; 50: 3302 – 3314.

[35] Benjamin TB. Gravity currents and related phenomena. J. Fluid Mech., 1968; 31(2): 209-248.

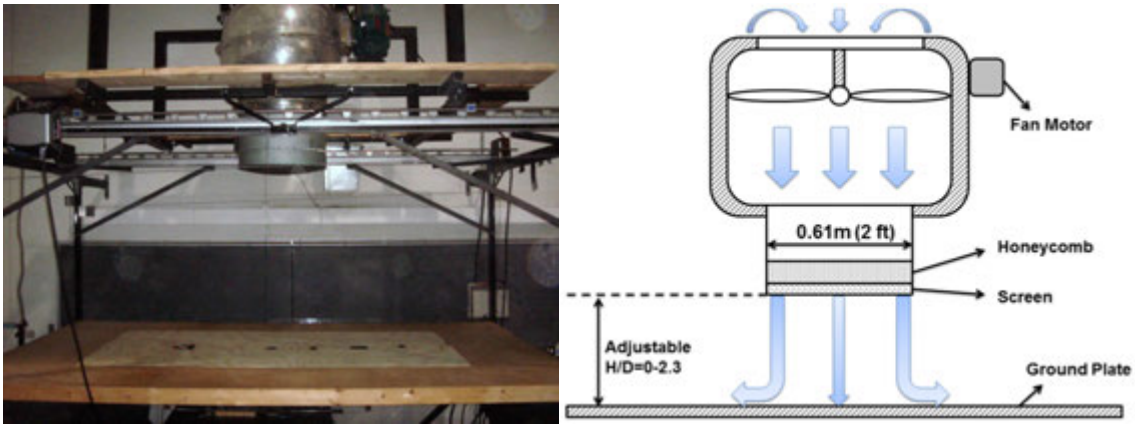

Figure 1. *Microburst simulator in WiST lab at Iowa State University*

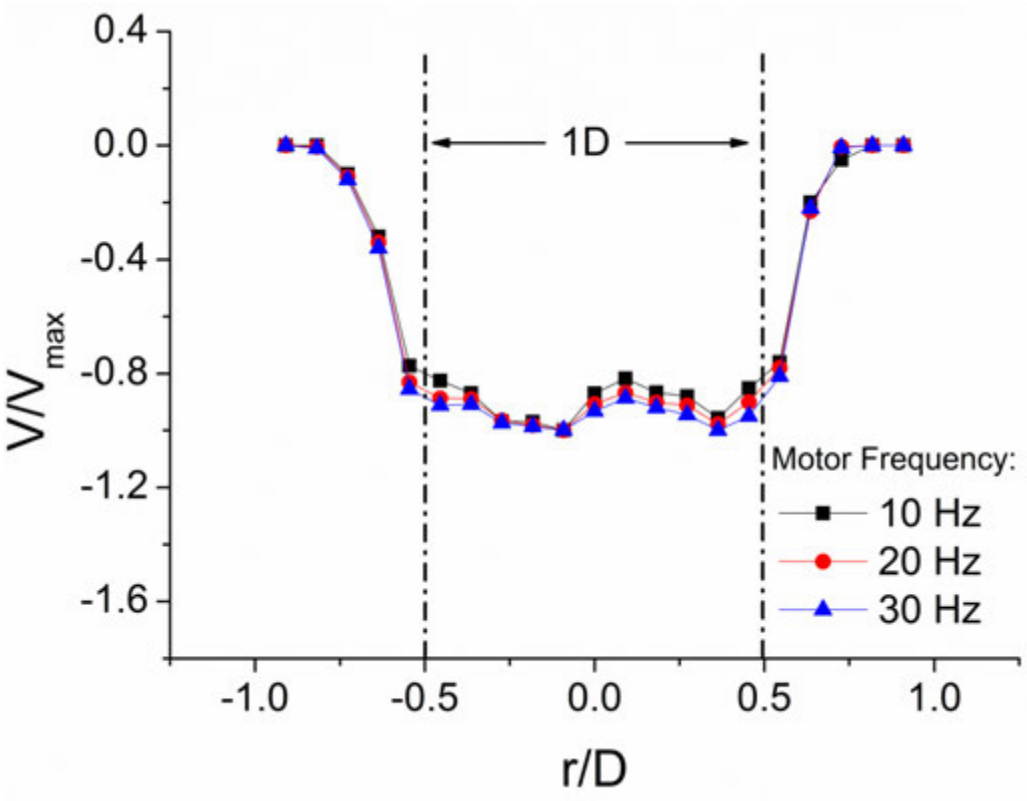

Figure 2. *Axial-velocity distribution across the jet (Experiment, Cobra-probe)*

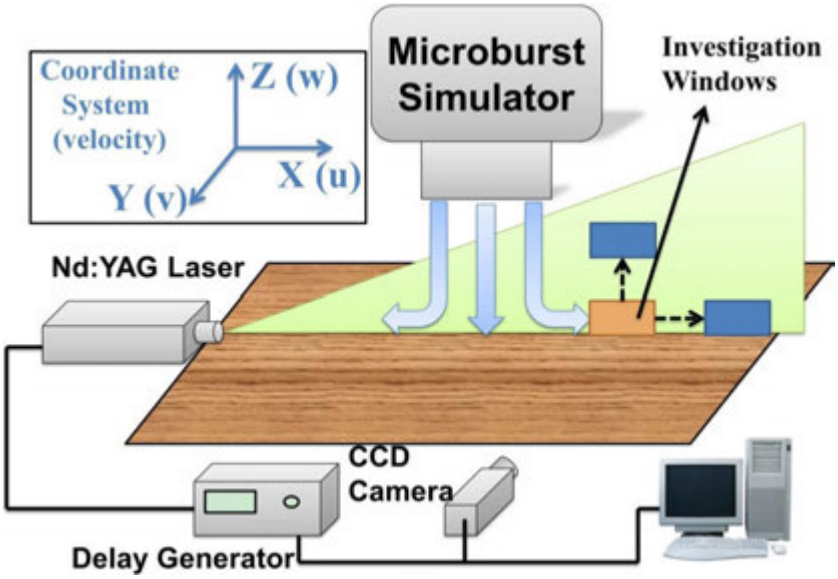

Figure 3. *Schematic of the PIV system*

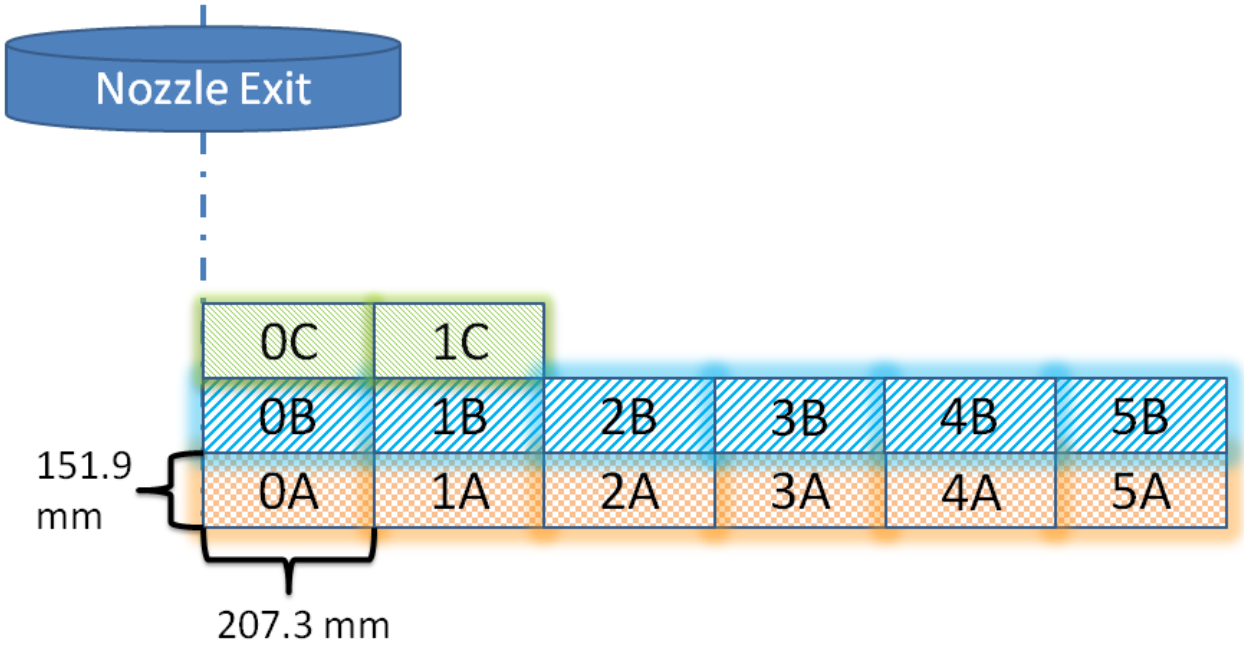

Figure 4. *Layout of investigation windows for PIV measurements*

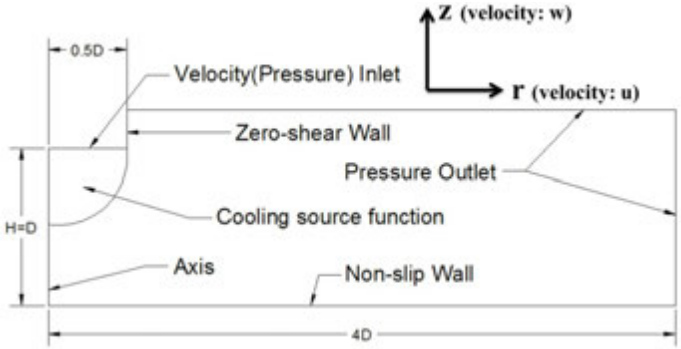

(a)

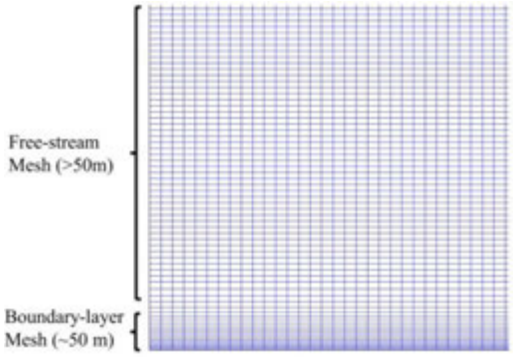

(b)

Figure 5. *Computational domain (a) and typical grid structure near wall boundary (b)*

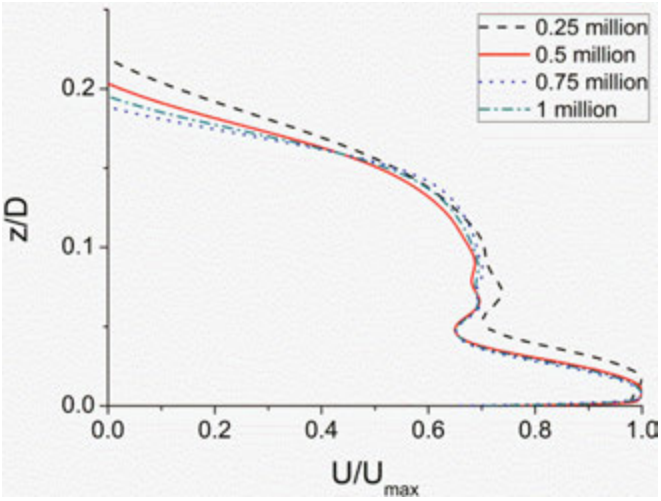

Figure 6. *Study of mesh independence (Normalized velocity at r/D=1.0)*

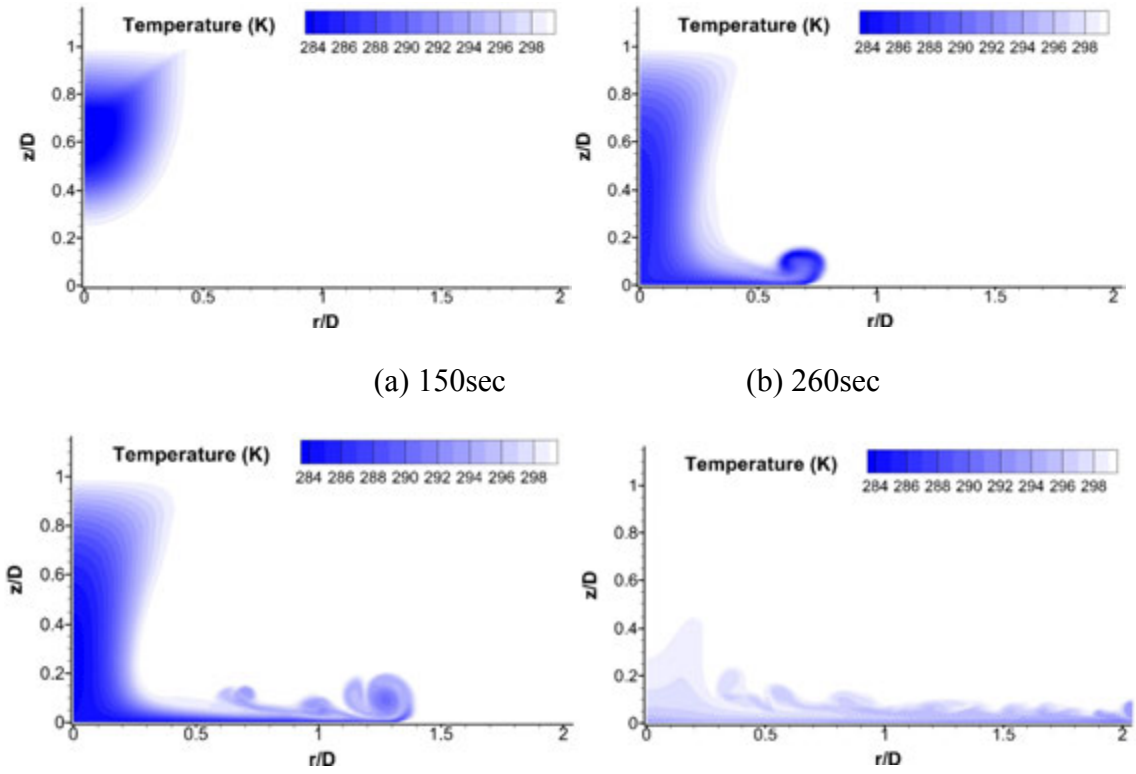

(a) 150sec (b) 260sec

(c) 380 sec. (d) 700 sec.

Figure 7. *Evolution of the temperature field in cooling source model (Numerical Simulation)*

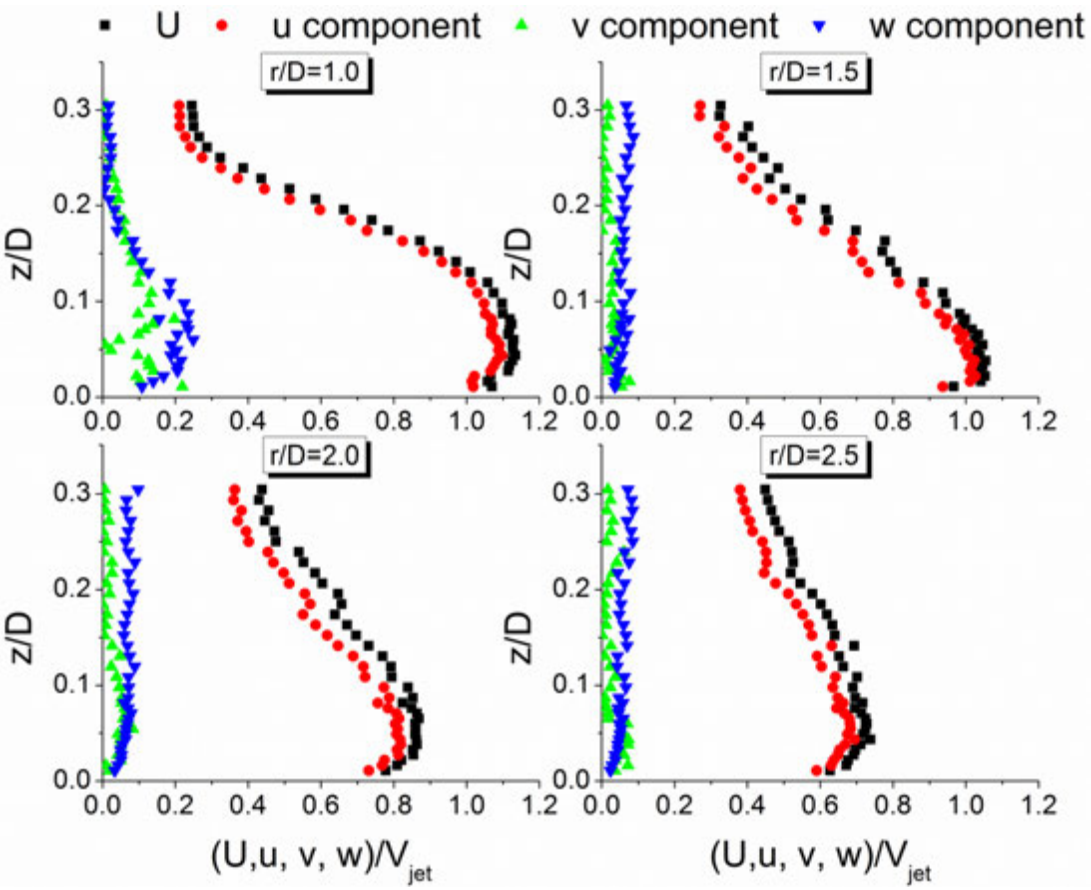

Figure 8. *Normalized componential radial-velocity profiles (Experiment, Cobra-probe)*

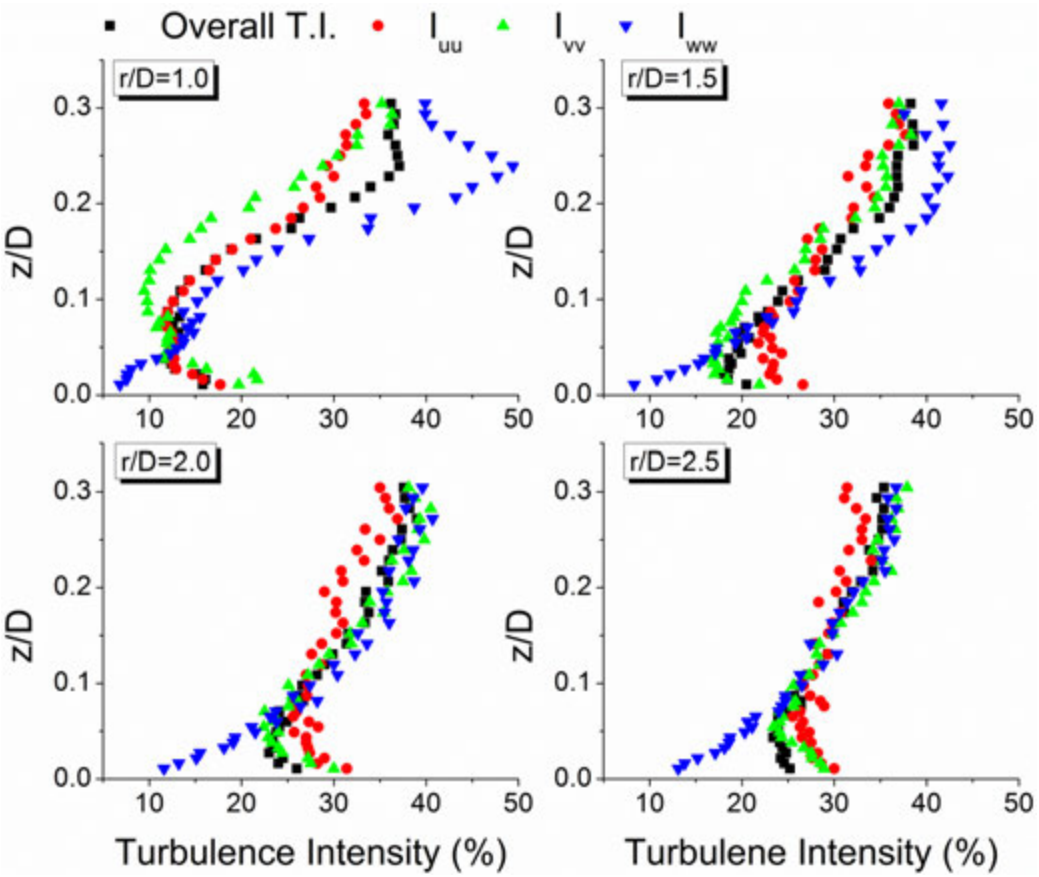

Figure 9. *Componential turbulence intensity component profiles (Experiment, Cobra-probe)*

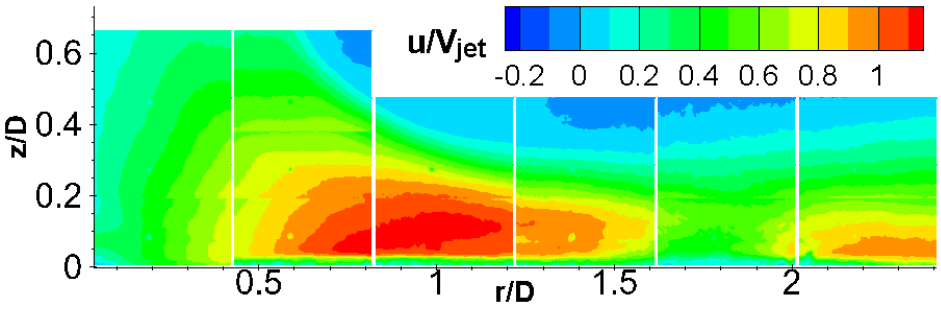

(a) Normalized U velocity

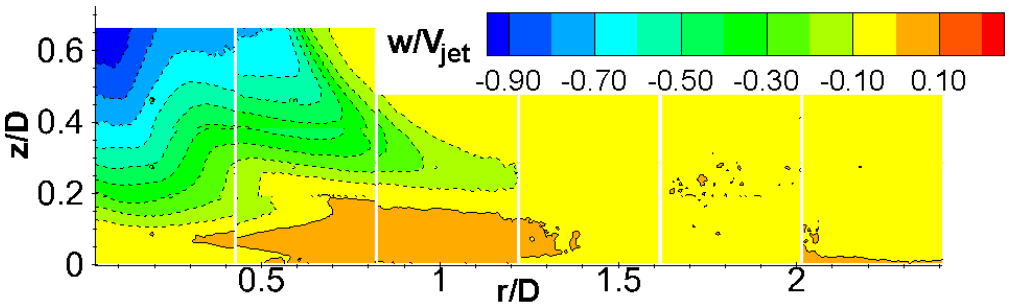

(b) Normalized W velocity

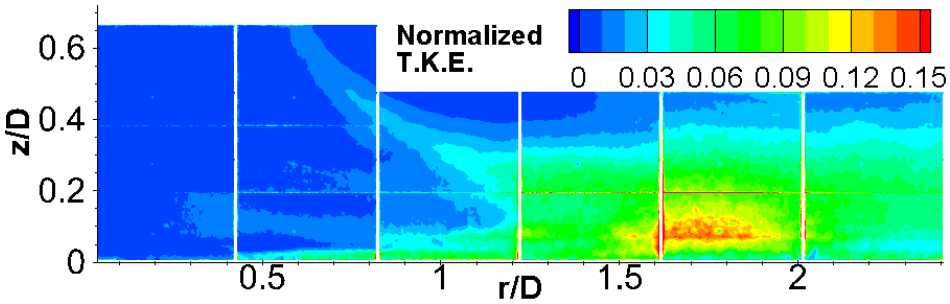

(c) Normalized T.K.E.

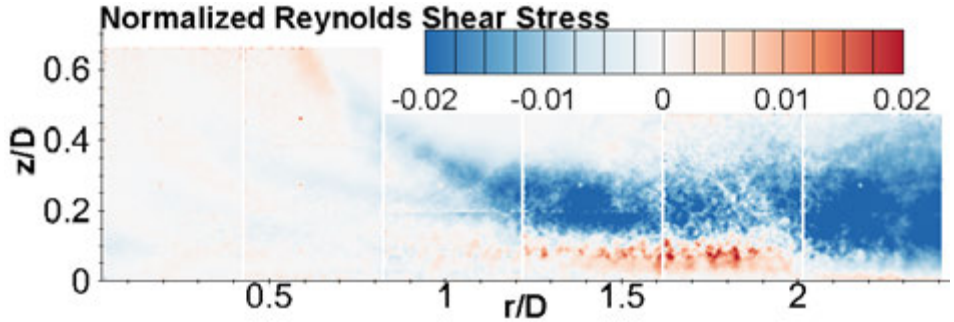

(d) Normalized Reynolds shear stress

Figure 10. *Ensemble-averaged flow fields for H/D=1 case (Experiment, PIV)*

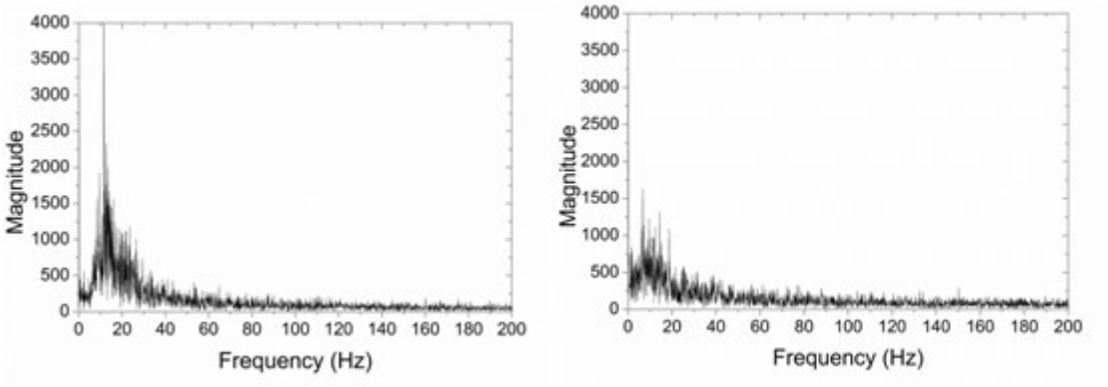

(a) r/D=1 (b) r/D=2

Figure 11. *Frequency spectrum of the radial-velocity fluctuation at z/D=0.20 (Experiment, Cobra-probe)*

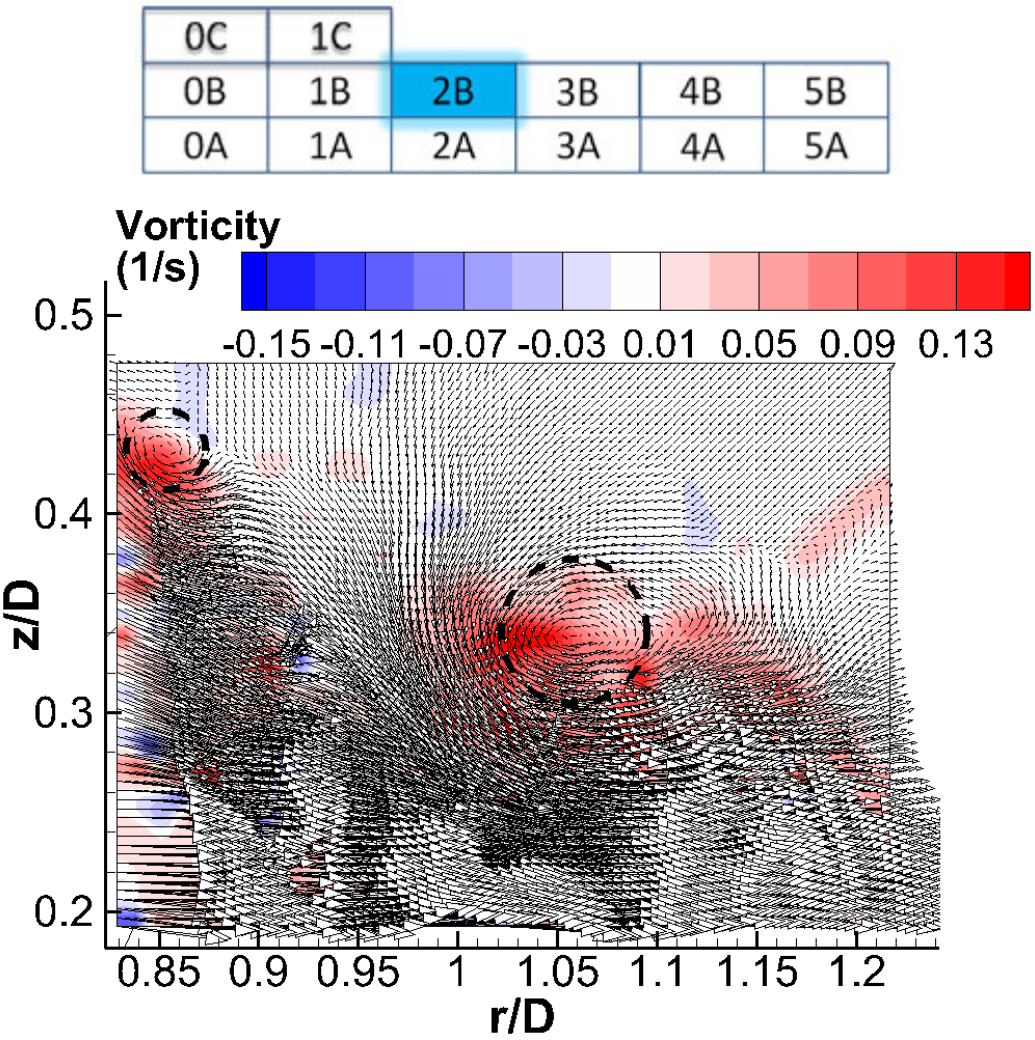

Figure 12. *A snapshot of the instantaneous vorticity field (Experiment, PIV)*

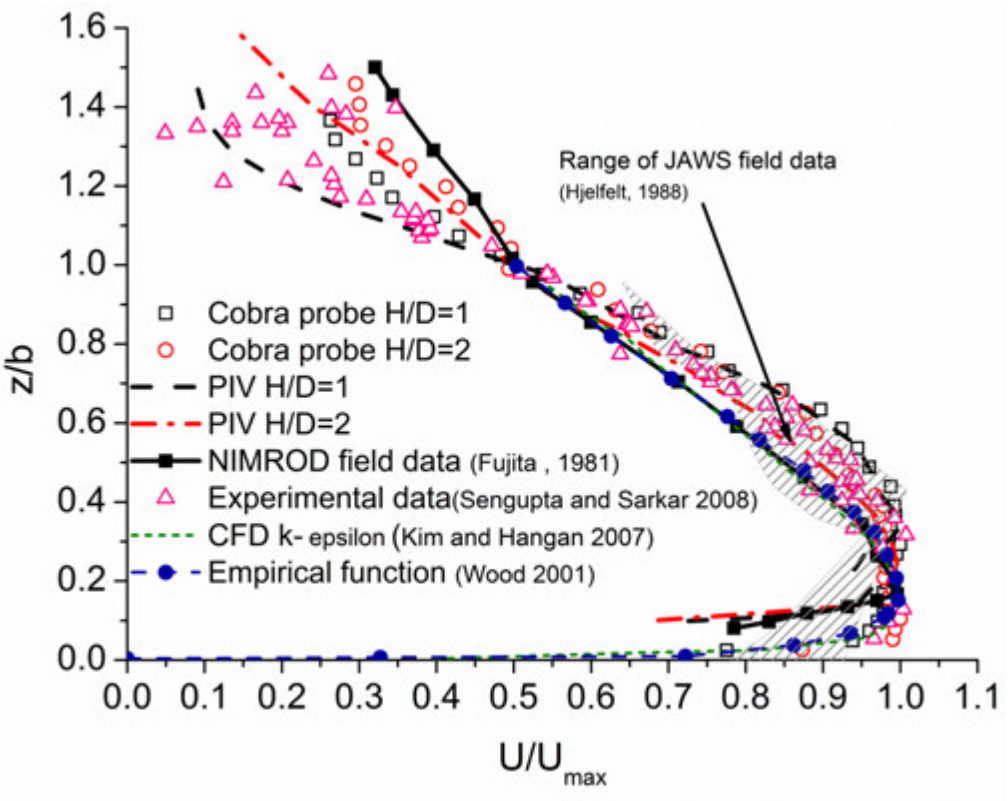

Figure 13. *Comparison of velocity profiles at the maximum velocity location (r/D=1)*

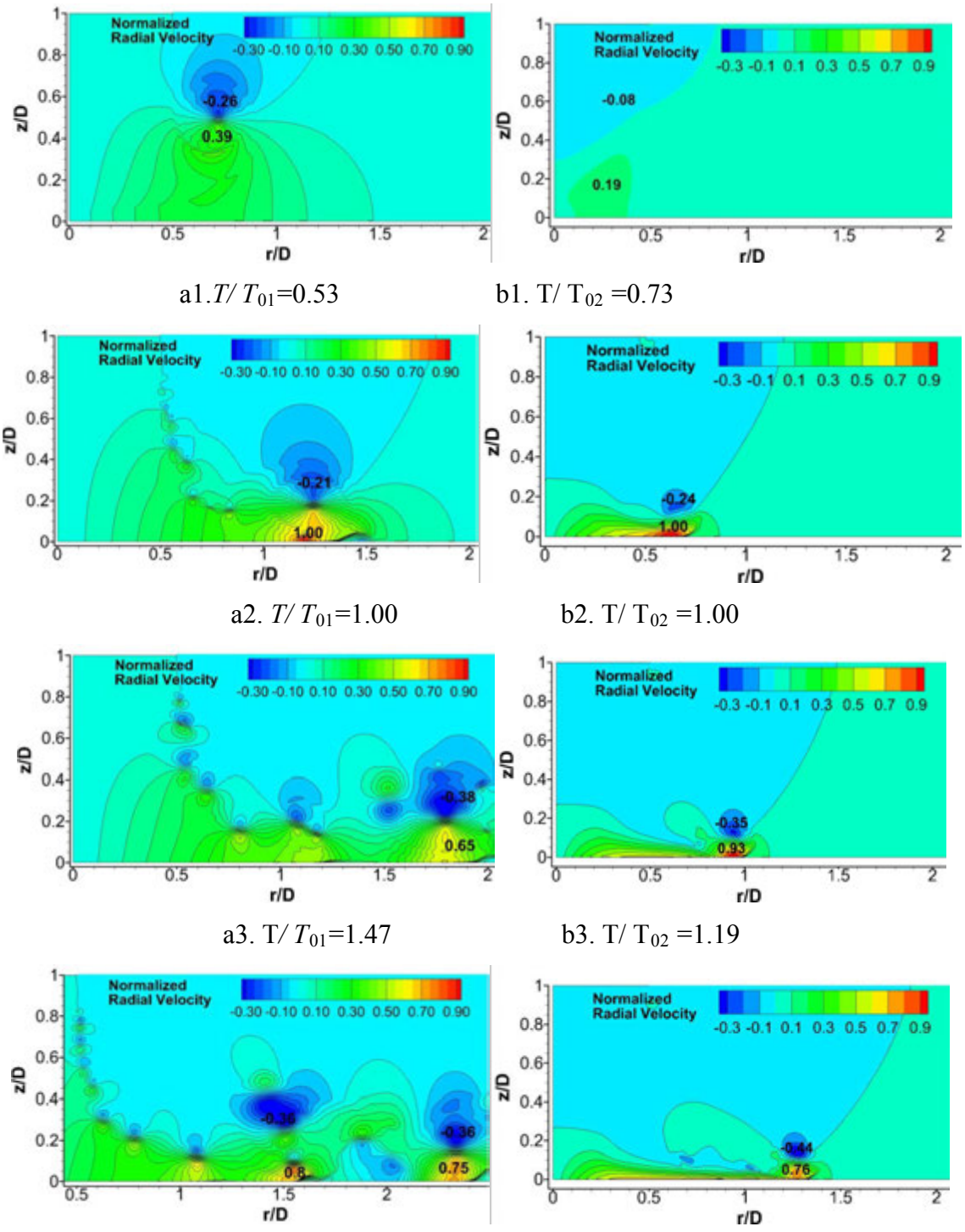

a1.T/T_{01}=0.53 b1. T/ T_{02} =0.73

a2. T/T_{01}=1.00 b2. T/ T_{02} =1.00

a3. T/ T_{01}=1.47 b3. T/ T_{02} =1.19

a4.T/ T_{01}=1.96 b4. T/ T_{02}=1.46

Figure 14. *Contour of normalized radial velocity (Numerical simulation)*

(a1-a4 impinging jet model;b1-b4 cooling source model)

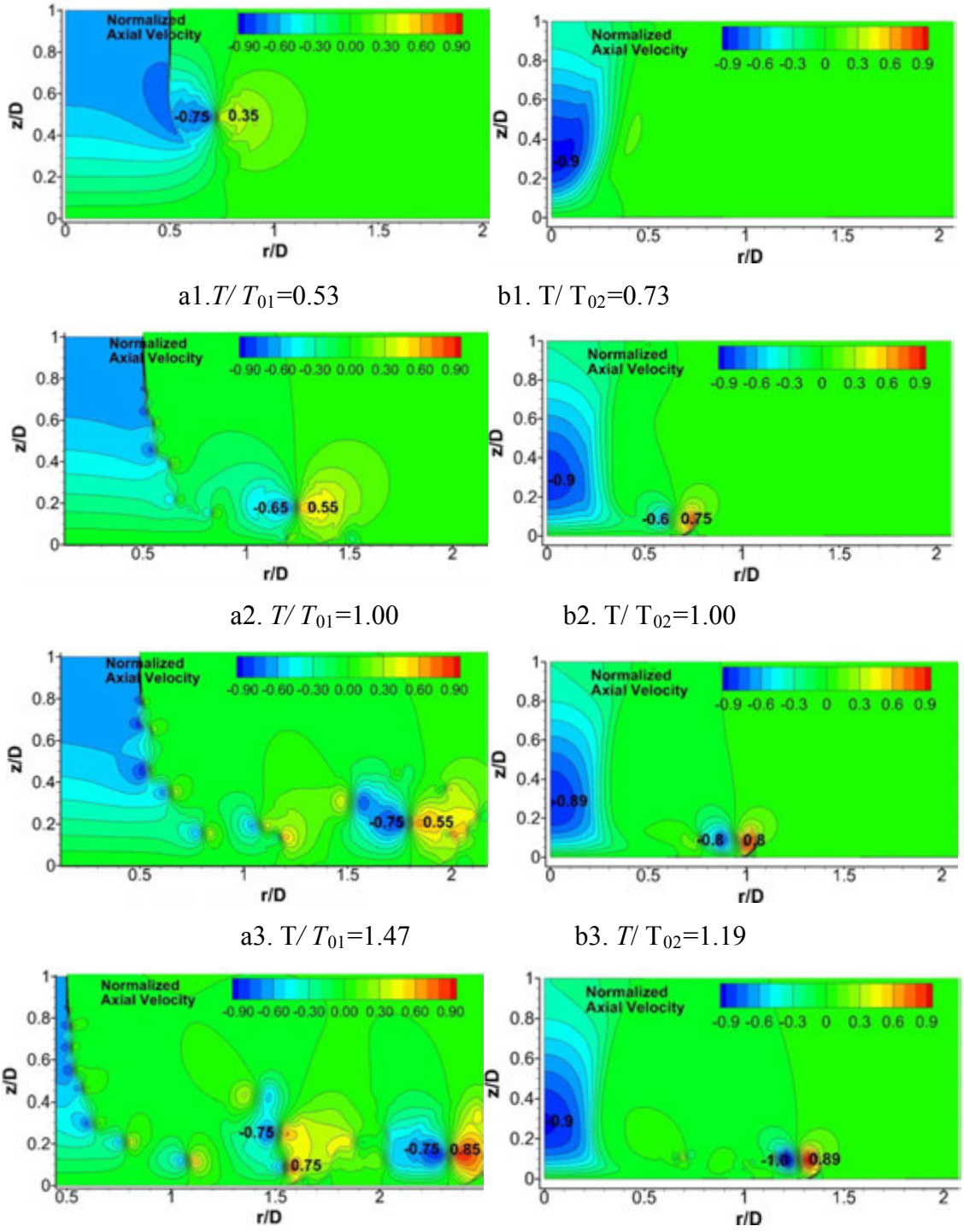

a1.T/T_{01}=0.53 b1. T/ T_{02}=0.73

a2. T/T_{01}=1.00 b2. T/ T_{02}=1.00

a3. T/ T_{01}=1.47 b3. T/ T_{02}=1.19

a4.T/ T_{01}=1.96 b4. T/ T_{02}=1.46

Figure 15. *Contour of normalized axial velocity (Numerical simulation)*

(a1-a4 impinging jet model; b1-b4 cooling source model

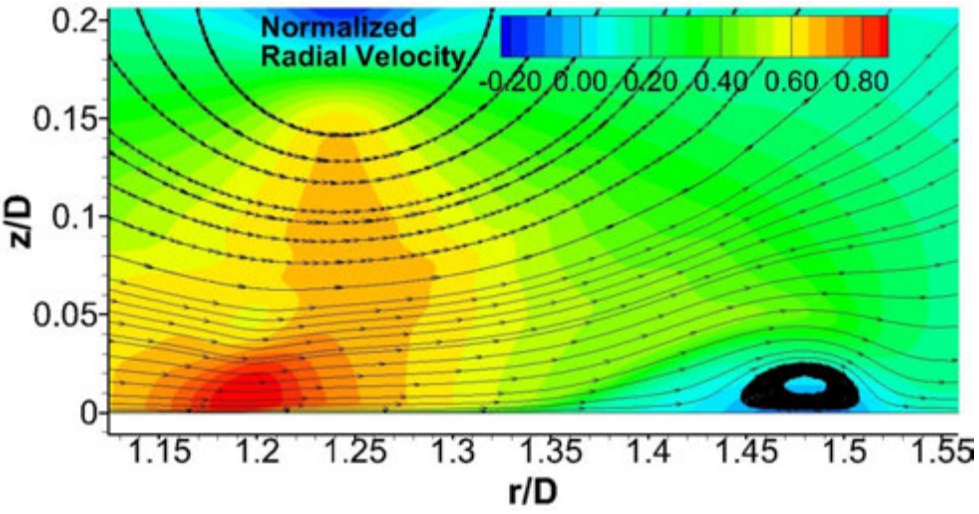

(a)

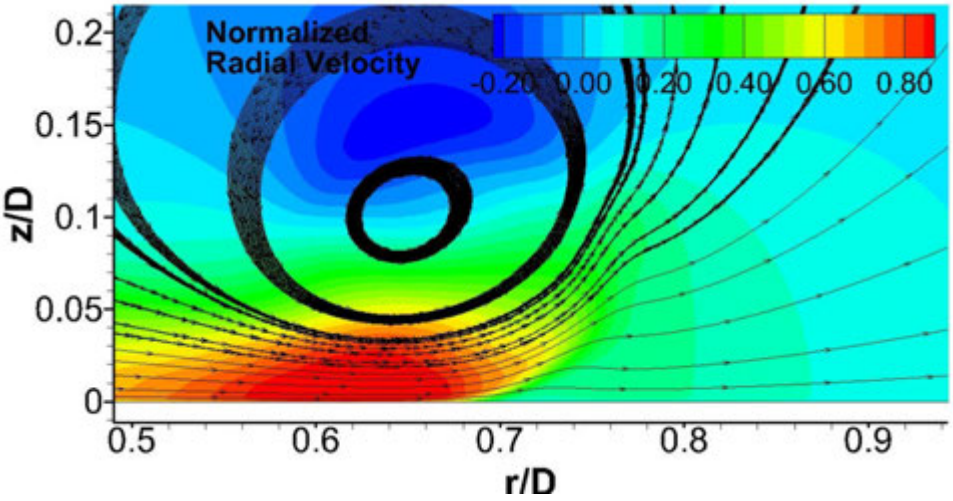

(b)

Figure 16. *Streamlines at the T/T_{01}=1.00 and T/T_{02}=1.00 (Numerical simulation)*

(a) impinging jet model; (b) cooling source model

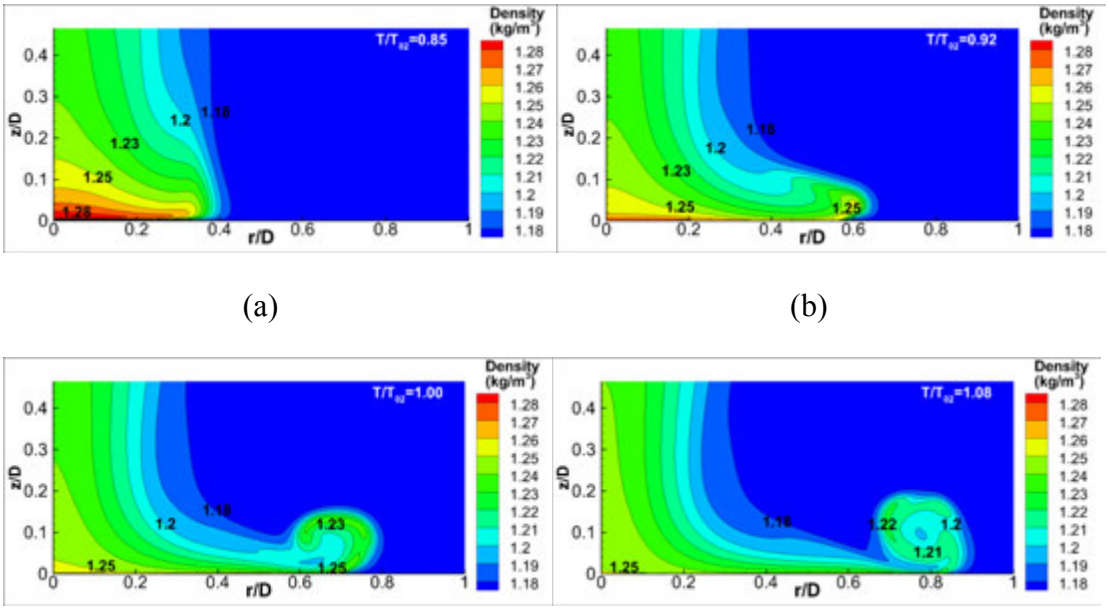

(a) (b)

(c) (d)

Figure 17. *Density contours at different time steps (Numerical simulation)*

(a)T/T_{02}=0.85; (b) T/T_{02}=0.92; (c) T/T_{02}=1.00; (d) T/T_{02}=1.08;

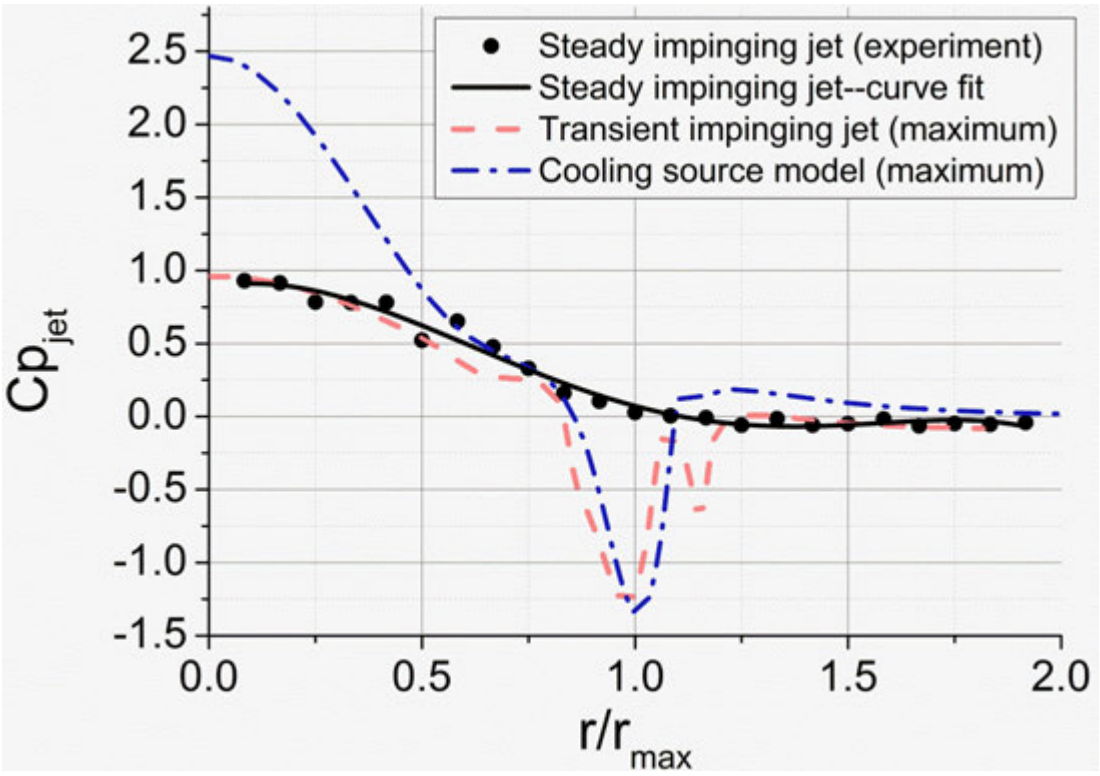

Figure 18. *Comparison of pressure distribution along radial direction*

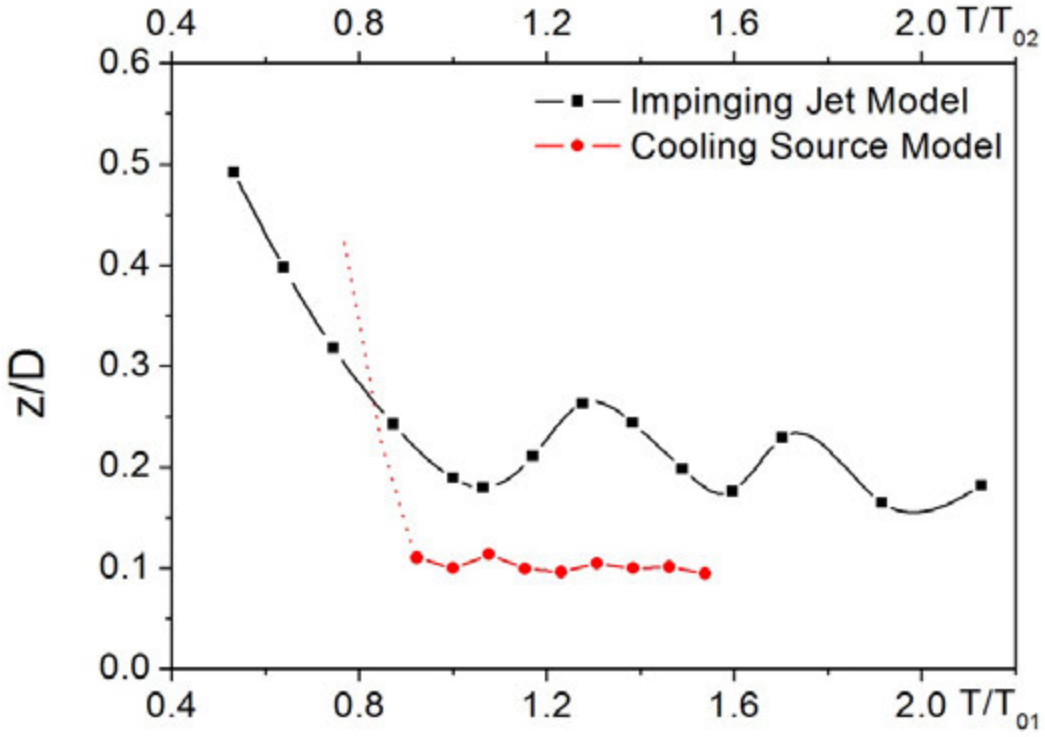

Figure 19. *Trajectories of the primary vortex cores of two models in axial direction (Numerical simulation)*

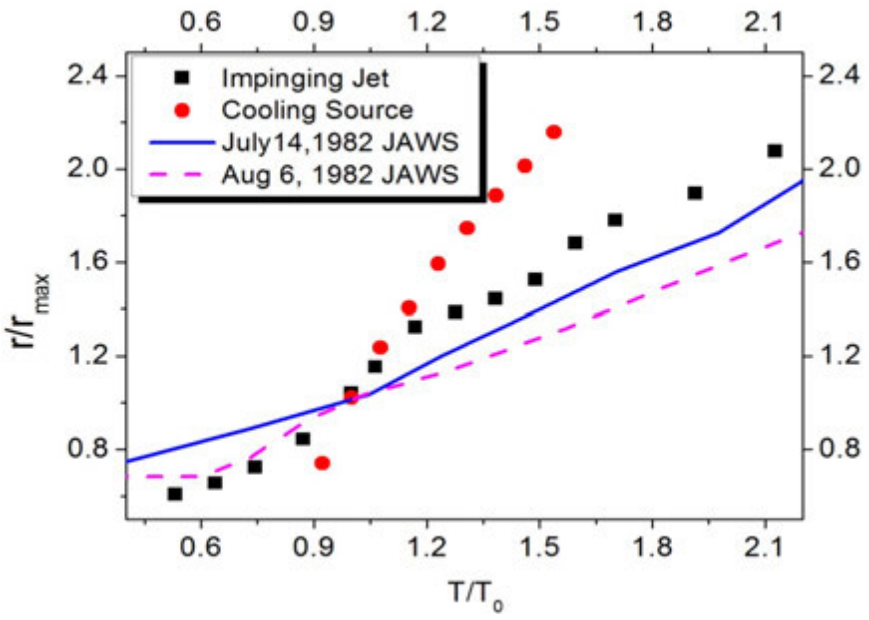

Figure 20. *Trajectories of the primary vortex cores of two models in radial direction (Numerical simulation; JAWS data provided by Hjelmfelt (1988)[5])*

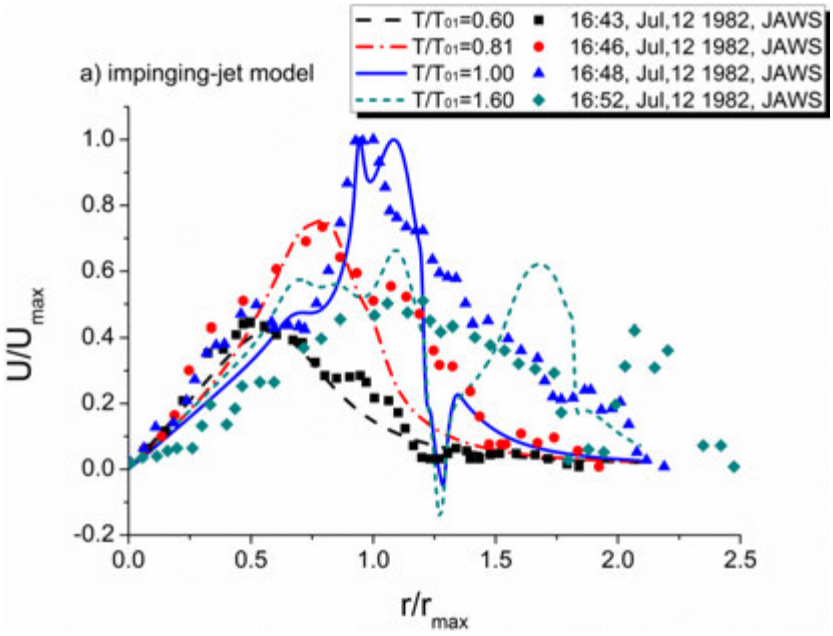

(a)

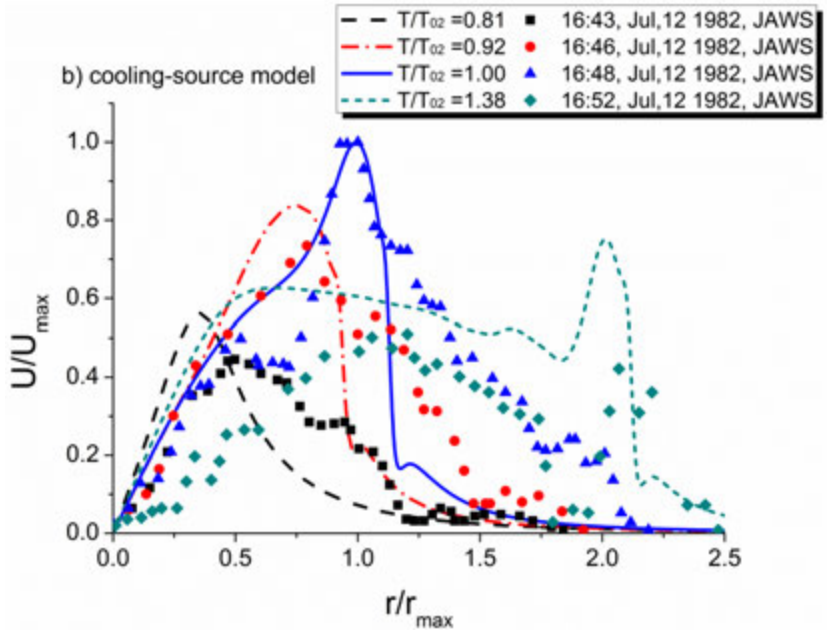

(b)

Figure 21. *Comparison of the time series of velocity profiles in radial direction (a) impinging jet model; (b) cooling source model (Numerical simulation; JAWS data provided by Hjelmfelt (1988)[5])*

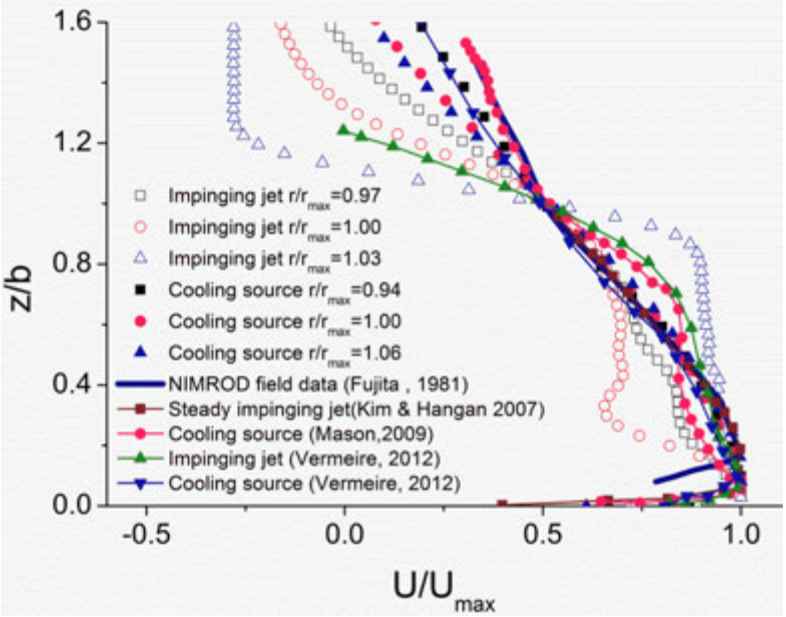

(a)

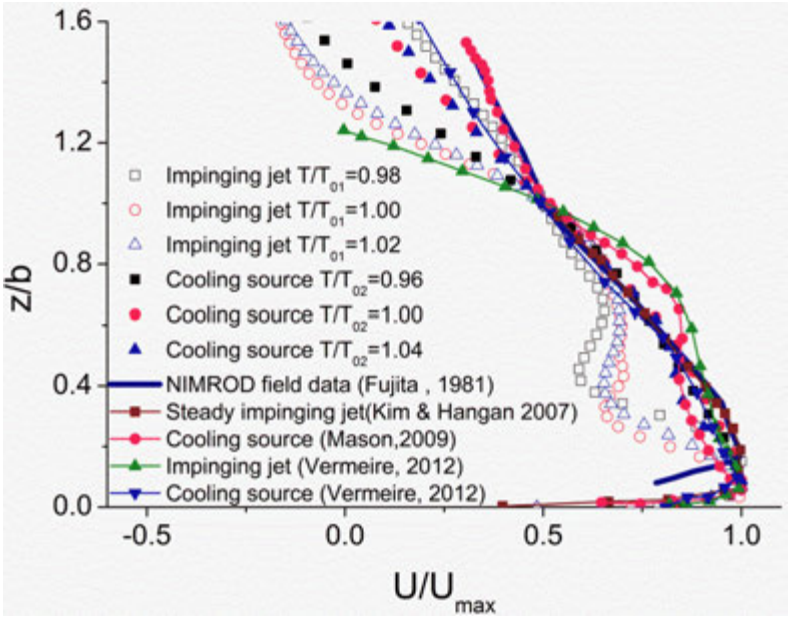

(b)

Figure 22. *Comparison of radial velocity profiles: (a) at the vicinity of the maximum velocity location at the time of its occurrence; (b) at the vicinity of the maximum velocity time (Numerical simulation)*

CHAPTER 3

AN EXPERIMENTAL STUDY OF FLOW FIELDS AND WIND LOADS ON GABLE-ROOF BUILDING MODELS IN MICROBURST-LIKE WIND

Yan Zhang, Partha Sarkar and Hui Hu

Department of Aerospace Engineering, Iowa State University, Ames, IA, 50011-2271

Abstract: An experimental study was conducted to quantify the flow characteristics of microburst-like wind and to assess the resultant wind loads acting on low-rise, gable-roof buildings induced by violent microburst-like winds compared with those in conventional atmospheric boundary layer (ABL) winds. The experimental work was conducted by using an impinging-jet-based microburst simulator in the Department of Aerospace Engineering, Iowa State University. Two gable-roof building models with the same base plan and mean roof height, but different roof angle, were used for a comparative study. In addition to measuring the surface pressure distributions to determine the resultant wind loads acting on the building models, a digital Particle Image Velocimetry (PIV) system was used to conduct flow field measurements to reveal the wake vortex and turbulence flow structures around the building models placed in the microburst-like wind. The effects of important parameters, such as the distance of the building from the center of the microburst, the roof angle of the building, and the orientation of the building with respect to radial outflow of the oncoming microburst-like wind, on the flow features such as the vortex structures and the surface pressure distributions around the building models as well as the resultant wind loads acting on the test models were assessed quantitatively. The measurement results reveal clearly that,

when the building models were mounted within the core region of the microburst-like wind, the surface pressure distributions on the building models were significantly higher than those predicted by ASCE 7-05 standard, thereby, induced considerably greater downward aerodynamic forces acting on the building models. When the building models were mounted in the outflow region of the microburst-like wind, the measured pressure distributions around the building models were found to reach a good correlation with ASCE 7-05 standard gradually as the test models were moved far away from the center of the microburst-like wind. It was also found that both the radial and vertical components of the aerodynamic forces acting on the building models would reach their maximum values when the models were mounted approximately one jet diameter away from the center of the microburst-like wind, while the maximum pressure fluctuations on the test models were found to occur at further downstream locations. Roof angles of the building models were found to play an important role in determining the flow features around the building models and resultant wind loads acting on the test models. The flow field measurements were found to correlate with the measured surface pressure distributions and the resultant wind loads (i.e., aerodynamic forces) acting on the building models well to elucidate the underlying physics of flow-structure interactions between the microburst-like winds and the gable-roof buildings in order to provide more accurate prediction of the damage potentials of the microburst wind.

1. Introduction

A downburst, which is characterized by a strong localized downdraft flow and an outburst of strong wind near the ground surface, occurs within a thunderstorm where the

weight of the precipitation and the cooling due to microphysical processes acts to accelerate the airflow downwards. Based on the 2001 Extreme Weather Sourcebook of National Center for Atmospheric Research (NCAR), approximately 5% of thunderstorms would produce a downburst that is primarily responsible for the estimated $1.4B of insured property loss each year in U.S. alone (data taken from 1950-1997). A microburst, as defined by Fujita (1985), is a strong downburst which produces an intense outburst of damaging wind with the radial extent being less than 4.0 kilometers, or else is defined as a macroburst. Although a "microburst" has a smaller size than its counterpart, "macroburst", it could induce a much stronger outflow with the maximum wind speed up to 270 km/h, i.e., 170 mph (Fujita, 1985).

As shown schematically in Figure 1, the flow characteristics of a microburst are dramatically different from those of conventional "straight-line" atmospheric boundary layer (ABL) winds (Kaimal and Finnigan, 1994) and other wind hazards of wide concerns, e.g., tornadoes and gust fronts. While a microburst is usually conceived as an upside-down tornado due to its basic flow pattern, in contrast to tornado-like winds (Bluestein and Golden 1993; Yang et al. 2011), microbursts produce negligible tangential-velocity components and behave more like purely straight-line winds in the outburst regions far away from the core regions of the microbursts. Unlike conventional ABL winds, a microburst can produce an impinging-jet-like outflow profile diverging from its center with the maximum velocity occurring at an altitude of less than 50 meters above ground (Hjelmfelt, 1988). Such extreme high wind speed and wind shear (i.e., velocity gradient) near the ground could produce a significantly greater damaging

potential to low-rise built structures compared to those of conventional ABL wind. Furthermore, in contrast to conventional ABL wind, microbursts could have strong vertical velocity components in both the core regions and the leading edges of the outburst, as shown in Figure 1, which can be extremely dangerous with respect to the safety of aircraft as well as to the built structures on the ground. As a result, it is highly desirable to characterize the flow features of the microburst wind in order to elucidate the underlying physics to provide more accurate prediction of the damage potentials of the microburst wind to both aviation industry and the low-rise built structures.

Initiated by a meteorological investigation of the 1976 Eastern 66 aircraft crash at New York City's JFK airport, several studies have been conducted by meteorologists as well as engineering researchers to quantify the flow characteristics of microburst wind. During 1970s and 1980s, two major research projects, the Northern Illinois Meteorological Research on Downburst (NIMROD, Chicago, IL) and the Joint Airport Weather Studies (JAWS, Denver, CO), were carried out to gather field data to quantify the microbursts occurring in nature. The field research efforts were documented in Fujita (1979), Wilson et al. (1984), Hjelmfelt (1987), and Hjelmfelt (1988). Meanwhile, a number of other field studies were also conducted at various locations. For example, Atlas et al. (2004) investigated the physical origin of a microburst occurring in the Amazonia region of South America by using a set of Doppler radar data. Vasiloff and Howard (2008) deployed two types of Radar systems to capture data from a severe microburst occurring near Phoenix, Arizona. While the field studies provided valuable measurement data to depict a vivid picture of microburst wind, only limited quantitative

information could be obtained through those field studies due to the technical challenges and intrinsic limitations of the Doppler Radar detection systems used in the field measurements (i.e., low scanning frequency and poor spatial resolution near ground). The limitations of field studies make laboratory experiments with microburst simulators and scaled test models essential tools to provide more detailed information about the flow characteristics of the microburst-like wind near the ground and their interactions with built civil structures in order to assess their destructive potentials.

While a typical microburst in nature is found to have a lifetime about 10 minutes, a steady impinging jet flow was found to resemble the major features of a microburst at its maximum strength reasonably well (Hjelmfelt, 1987). Therefore, steady impinging jet model has been widely adopted to simulate microburst-like wind in laboratory experiments due to its simplicity and ability to produce outflow velocity profiles resembling that of microburst wind. A number of numerical and experimental studies have been conducted in the past years to utilize the steady impinging jet model to investigate the flow characteristics of microburst-like wind. Silva and Holmes (1992) used a two-dimensional k-ε model to simulate an impinging jet flow to characterize the flow features of microburst-like winds. Holmes (1999) and Letchford & Illidge (1999) performed experimental studies using an air jet impinging onto a wall to investigate the topographic effects of a microburst on the outflow velocity profiles. Wood et al. (2001) studied the characteristics of microbursts over various terrains, both experimentally and numerically, by using an impinging jet model. Choi (2003) carried out both field and laboratory measurements to study on a series of Singapore thunderstorms. Terrain

sensitivity of microburst outflows was studied by comparing the microburst observations at different heights and impinging-jet experiments with different height-to-diameter ratios. The study produced similar trends, which confirms the good capability of impinging jet model to simulate microburst-like wind. Chay et al. (2005) conducted numerical simulations of impinging jet flows and obtained good agreements with the wind-tunnel measurement results of microburst-like wind. To physically capture transient features of microbursts, Mason et al. (2005) suggested a pulsed impinging-jet model to simulate transient microburst phenomena. Holmes and Oliver (2000) empirically combined wall-jet velocity and translational velocity and obtained a good representation of a travelling microburst that was well correlated with a microburst occurred at Andrews AFB in 1983. Kim and Hangan (2007) and Das et al., (2010) performed CFD studies to simulate both steady and transient microbursts using the impinging-jet model, producing reasonable radial-velocity profiles and good primary-vortex representation of microburst-like wind. In summary, the impinging jet model has been proved to be very effective to simulate microburst wind in laboratory experiments.

With the consideration of buildings as surface-mounted obstacles, extensive experimental and numerical studies have been carried out to investigate the flow-structure interactions between building models and turbulent surface winds as well as the resultant wind loads acting on the building models. Besides the studies using prismatic obstacles to represent cube-shaped buildings, several studies have also been conducted to consider more realistic residential building models with various gable roof shapes (Holmes 1993; Kanda and Maruta 1993; Peterka et al. 1998; Uematsu and Isyumov

1999; Stathopoulos et al. 2001; Sousa 2002; Sousa and Pereira 2004; Liu et al. 2009; Hu et al. 2011) to quantify the effects of the gable-roof shapes on the wake flow characteristics as well as the resultant wind loads acting on the building models. While many important findings have been obtained through the previous studies, most of those studies were conducted with the building models placed in conventional ABL wind.

As aforementioned, a microburst can produce an impinging jet-like outflow profile diverging from its center with the maximum velocity occurring at an altitude of less than 50 meters above the ground. It has also strong vertical velocity components in both the core region and the leading edge of the outburst flow. Such extreme surface winds and high velocity gradients near the ground could produce much greater damaging effects on low-rise buildings compared with conventional ABL wind. Due to the distinct features of the microburst-like wind, the current design standards of low-rise buildings may not be applicable to estimate the wind loads induced by microburst-like wind, the characteristics of the flow-structure interactions between the low-rise buildings and the devastating microburst wind would be very different from those with conventional ABL wind. Surprisingly, although microbursts are well-known natural hazards, only very few studies can be found in literature to specifically address the flow-structure interactions between microburst-like wind and buildings. Nicholls et al. (1993) conducted a Large Eddy Simulation (LES) study to investigate the flow structures around a cube-shaped building model in microburst-like wind. Savory et al. (2001) utilized an impinging-jet model to investigate the failure of a lattice transmission tower in microburst-like wind. Chay and Letchford (2002), Letchford and Chay (2002) investigated the pressure

distribution over a cube-shaped building model in steady and translating microburst-like wind by performing laboratory experiments with an impinging-jet model. More recently, Sengupta and Sarkar (2008) conducted an experimental study to quantify the transient loads acting on a cube-shaped building model with an impinging-jet-based microburst simulator. It should be noted that, while most of the previous studies on building models in microburst-like wind were conducted by measuring wind loads and/or surface pressure distributions on cube-shaped building models only, no study can be found in literature to provide flow field measurements to quantify the globe flow features of microburst-like winds and the flow-structure interactions between the microburst-like winds and low-rise buildings. Furthermore, while gable-roof building are the most common low-rise buildings, which are very vulnerable to microburst wind, many important aspects about the flow-structure interactions between microburst wind and gable-roof buildings as well as the resultant wind loads (e.g., aerodynamics forces) acting on gable-roof buildings induced by the microburst-like wind are still unclear.

In the present study, an experimental study was conducted to quantify the flow characteristics of microburst-like wind and to assess the fluid-structure interactions of gable-roof buildings in microburst-like wind using scaled models. The experimental work was conducted by using an impinging-jet-based microburst simulator located in the Aerospace Engineering Department of Iowa State University (ISU). Two low-rise gable-roof building models with the same base plan and mean-roof height but different roof angles were used for the comparative study. In addition to mapping the surface pressure distributions around the building models to determine the resultant wind loads

(i.e., aerodynamic forces) acting on the models in the microburst-like wind, a high-resolution Particle Image Velocimetry (PIV) system was used to conduct flow field measurements to reveal the flow features and wake vortex structures around the gable-roof building models in microburst-like wind. The flow field measurements were correlated with the surface pressure and resultant wind loads measurements in order to elucidate the underlying physics. The effects of important parameters, such as the distance of the building from the center of the microburst, the roof angle and orientation angle of the building with respect to the radial outflow of the oncoming microburst-like wind, on the flow field and surface pressure distributions on the building models (thereby, the resultant aerodynamic forces acting on the models) induced by the microburst-like wind were assessed quantitatively. The objective of the present study is to gain further insight into the underlying physics of the flow-structure interactions of low-rise gable-roof buildings and microburst-like wind for a better understanding of the damage potential of microburst-like wind to low-rise buildings.

2. Experimental Setup and ISU Microburst Simulator

2.1 ISU Microburst Simulator

The experimental study was conducted by using an impinging-jet-based microburst simulator located in the Aerospace Engineering Department of Iowa State University (ISU). As mentioned earlier, impinging jet model has been widely used to simulate microburst wind due to its simplicity to produce outflow profiles resembling microburst wind. Two methods are usually used in previous studies to generate impinging jet flows in laboratory experiments to investigate microburst-like winds. One method is to utilize

density difference between the core jets and ambient surrounding flows to form buoyancy-driven downdrafts, which is usually used to elucidate the underlying physics pertinent to the formation mechanism of microbursts (Alahyari and Longmire, 1995). The other method is to use fans/blowers to generate forced jet flows impinging onto ground plates, which was widely used to assess the global flow features of microburst-like winds and the microburst-induced wind loads acting on building models mounted on the ground plates (Sengupta and Sarkar, 2008). While the formation mechanism of microbursts is very complicated and worth further investigations, the assessments of the global flow feature of microburst-like wind and microburst-induced wind loads acting on buildings are very important topics in wind engineering community. While the main objective of the present study is to quantify the flow characteristics of microburst-like wind and to assess the microburst-induced wind loads acting on low-rise, gable-roof buildings, the second method was used to generate a forced impinging jet flow in the present study. Figure 2 shows the schematic and photo depicting the flow circuit and dimensions of ISU microburst simulator used in the present study. As shown in Figure 2, a downdraft flow is generated through an axial fan driven by a step motor. The exhaust nozzle diameter of ISU microburst simulator is 610 mm (i.e., D = 610mm). The distance between the nozzle exit and the ground plane (H) is adjustable up to 2.3 times the nozzle diameter. Honeycomb and screen structures are placed upstream of the nozzle exit in order to produce a uniform jet flow exhausted from ISU microburst simulator. During the experiments, a three-component cobra-probe (Turbulent Flow Instrumentation Pvt. Ltd.®), which is capable of simultaneously measuring all three components of the wind

velocity vector, was used to quantify the flow characteristics of the jet flow at the points of interest. It was found that the jet flow exhausted from ISU microburst simulator was quite uniform across the nozzle exit, and the turbulence level of the core jet flow was found to be within 1.0%. For most of the measurement results given in the present study, the ground floor was fixed at *2D* below the ISU microburst simulator (i.e., *H/D* = 2.0). The flow velocity at the nozzle exit of the ISU microburst simulator was set to 6.0m/s (i.e., $U_{jet}= 6.0\ m/s$), which corresponds to a Reynolds number of 2.4×10^5 based on the nozzle diameter, *D*, of the ISU microburst simulator. Further information about the design, construction, and performance of ISU microburst simulator as well as the quantitative comparisons of the microburst-like wind generated by using the simulator with the microbursts occurring in nature can be found in Zhang et al. (2012).

It should be noted that, dynamic similarity is one of the greatest challenges to conduct laboratory experiments to stimulate meteorological phenomena such as microbursts. It will be very difficult, if not impossible, to match the Reynolds numbers of the microbursts in nature with those of the impinging jet flows generated in the laboratories due to the significant scale difference of the two cases. It has been found that, although the Reynolds numbers of the laboratory experiments may not be able to match to those of microbursts in nature, the measurement results obtained from laboratory experiments are still very useful to reveal the flow characteristics of microburst-like winds and to predict the winds loads acting on test models induced by microburst-like wind as long as the Reynolds number of the laboratory experiments is high enough. Therefore, the findings derived from the present study are believed to be

very helpful to improve our understanding about the flow characteristics of microburst-like winds and flow-structure interactions between the microburst-like winds and the gable-roof buildings in order to provide more accurate prediction of the damage potentials of the microburst wind.

2.2 The gable-roof building models

Figure 3 shows the schematic of the two gable-roof building models used in the present study: one with a roof angle of 16 degree and the other with a roof angle of 35 degree. The two models were designed to have the same square shaped base plan and the same mean roof height. The primary design parameters of the test models (i.e., both the absolute values and non-dimensional values normalize by the diameter of the microburst simulator, *D*) are listed in Table 1. With the scale ratio of the 1:650, the test models used in the present study would represent gable-roof buildings with about 42m×42m in base plan and 23m in mean-roof-height interacting with a microburst of 400m in diameter.

As shown in Figure 3(b), each of the test models was equipped with 80 pressure taps for the surface pressure distribution measurements around the model. The pressure taps were connected to two ZOC pressure sensor systems (Scanivalve Corp.®) by using tygon tubing (1.5mm in diameter and 0.8m long) for the surface pressure data acquisition. The ZOC pressure sensor systems incorporate temperature compensated piezoresistive pressure sensors with a pneumatic calibration valve, RAM, 16 bit A/D converter, and a microprocessor in a compact self-contained module. The precision of the pressure acquisition system is ±0.2% of the full scale (±10 in. H2O). During the experiments, the

instantaneous surface pressure measurement data were acquired for 100s with data acquisition rate of 100 Hz for each test case.

During the experiments, the surface pressure distributions, $C_P = (P - P_{atm})/(0.5\rho U_{jet}^2)$, on the test models were measured with the models located at different radial distances from the center of the impinging jet, i.e., at r/D ≈ 0.0, 0.5, 1.0, 1.5, and 2.0. As shown in Figure 4, the test models were also mounted at three different orientation angles, i.e., 0 degree, 45 degree, and 90 degree, with respect to the oncoming microburst-like wind at each downstream location. The resultant wind loads (i.e., aerodynamic forces) acting on the test models were determined by integrating the surface pressure distributions around the test models.

In addition to the surface pressure distribution and resultant wind load measurements, a high-resolution Particle Image Velocimetry (PIV) system was used to quantify the flow characteristics of the microburst-like wind around the gable-roof building models. For the PIV measurements, the airflow was seeded with ~1 μm oil droplets by using a droplet generator. As shown in Fig 4, illumination was provided by a double-pulsed Nd:YAG laser (NewWave Gemini 200) adjusted at the second harmonic frequency and emitting two 200 mJ laser pulses at a wavelength of 532 nm and a repetition rate of 10 Hz. The laser beam was shaped into a laser sheet (thickness ~1 mm) by using a set of spherical and cylindrical lenses. A high-resolution charge-coupled device (CCD) camera (PCO1600, Cooke Corp.) was used for PIV image acquisition with its view axis perpendicular to the illuminating laser sheet. The CCD camera and the double-pulsed Nd:YAG lasers were connected to a workstation via a Digital Delay

Generator (Berkeley Nucleonics, Model 565), which controlled the timing of both the laser illumination and the image acquisition. Instantaneous PIV velocity vectors were obtained using a frame-to-frame cross-correlation technique involving successive frames of image patterns of particle images in an interrogation window of 32×32 pixels. An effective overlap of 50% of the interrogation windows was employed in PIV image processing. After the instantaneous velocity vectors were derived, time-averaged quantities, such as the mean velocity (V_r, V_z), turbulent velocity fluctuations (v_r', v_z') and the normalized turbulent kinetic energy (i.e., $T.K.E. = (\overline{v_r' v_r'} + \overline{v_z' v_z'}) / U_{jet}^2$) of the turbulent flow, were obtained from a time sequence of 1,000 frames of the instantaneous PIV measurement results for each test case. The uncertainty level for the instantaneous PIV measurements is estimated to be within 2.0%, and those of the turbulent velocity fluctuations and turbulent kinetics energy are about 5.0%.

In the present study, the size of each PIV measurement window was set to be about 210mm×160 mm in order to ensure a reasonable good spatial resolution of the PIV measurements (i.e., ~2.0mm). Since this measurement window is quite small compared with the dimension of ISU microburst simulator (D=0.61m), the PIV measurement results from 14 different measurement windows were combined to reveal the global features of the microburst-like wind generated by ISU microburst simulator more clearly. The layout of the 14 PIV measurement windows is illustrated in Fig 4 (b).

3. Results and Discussions

3.1 The Flow Characteristics of the Simulated Microburst-like Wind

In the present study, the flow characteristics of the microburst-like wind generated by ISU microburst simulator were quantified by using the high-resolution PIV system before the gable-roof building models were mounted on the ground plane. As described above, PIV measurement results from 14 different measurement windows were combined to reconstruct a large flow field (~ 0.4m×1.5m) in order to reveal the flow features of the microburst-like wind more clearly. Figure 5 shows the reconstructed flow field in the terms of the flow velocity vectors (only about 1.5% of the vectors are shown here), the contour maps of the radial and vertical velocity components (V_r, V_z), and the normalized turbulent kinetic energy (i.e., normalized T.K.E) as well as the streamlines of the microburst-like wind in the measurement windows. It can be seen clearly that, the streamlines of the jet flow exhausted from ISU microburst simulator are mainly vertical in downward direction before impinging onto the ground plane, as expected. As a result, the microburst-like wind was found to have a strong vertical component in the core region and the leading edge of the outburst region (i.e., r/D ≤ 0.5), which are dangerous to the safety of aircraft as well as built structures on the ground. Upon impinging onto the ground plane, the flow was found to turn right angle rapidly, and the corresponding streamlines were found to become horizontal lines in the outburst flow. While diverging away from the core center of the microburst-like wind, the flow was found to be accelerated at first, reach its maximum wind speed at the location of r/D ≈1.0, and then slow down gradually at further downstream. Since the radial velocity

component (i.e., V_r component) was found to become dominant in the outflow region of the microburst-like wind (i.e., r/D>0.50), the streamlines of the flow in the outburst flow were found to become parallel straight lines near the ground plane. It indicates that the microburst-like wind would behave more like a straight-line wind in the outflow region near the ground plane.

It should be noted that, even though the streamlines of the microburst-like wind in the outflow region were found to become parallel straight-lines, the flow characteristics of the microburst-like wind were still quite different from those in conventional ABL winds. As revealed clearly from the PIV measurement results given in Fig 5, after impinging onto the ground plane, the high-speed diverging airflow was found to concentrate within a thin layer very close to the surface of the ground plane (i.e., Z/D < 0.25). Unlike conventional ABL winds with the wind speed increasing monotonically above the ground, the microburst-like wind was found to reach its maximum wind speed at a height very close to the ground surface (i.e., Z/D≈0.06 for the present study), and then begin to decrease gradually as the height above the ground plate increases. Such extreme high-wind shear near the ground surface in microburst winds have been suggested to be the main reason to cause significant damages to low-rise civil structures on the ground.

From the measured normalized turbulent kinetic energy distribution shown in Fig 5(d), it can be seen clearly that the turbulence level within the core region of the microburst-like wind (i.e., r/D≤0.5) is quite low. The turbulence intensity was found to

increase greatly in the outflow region of the microburst-like wind (i.e., r/D>1.0). A region with very high turbulence intensity (i.e., much higher turbulent kinetic energy) was found to exist at the downstream location of r/D≈1.5~2.0. The high turbulence intensity in the region was found to be responsible for the significant surface pressure fluctuations and extreme wind load peaks acting on the building models when mounted in the region, which will be discussed later in the present study.

Figure 6 shows the quantitative comparisons of the measured outflow velocity profile of the microburst-like wind of the present study versus the NIMROD field measurement data of real microbursts occurring in nature along with the published data of previous studies. As suggested in previous studies, while the detailed flow features of each microburst may vary from case to case, all the microbursts were found to have a similar trend in terms of normalized outflow velocity profiles. The outflow velocity profiles given in Figure 6 were taken in the vicinity of the radial location where the maximum wind speeds in the microburst-like winds occur. As shown in Figure 6, while the radial velocity of the microburst-like wind was normalized by the maximum radial velocity $V_{r,max}$ (i.e., $V_r/V_{r,max}$), the height where half of the maximum radial velocity occurred (i.e., b≈170 mm for the present study) was used to normalize the vertical height in the microburst-like wind (i.e., z/b). It can be seen clearly that, even though the simulated microburst-like wind by using ISU microburst simulator and the real microbursts occurring in nature are significantly different in their size (e.g., the one generated by using ISU microburst simulator with a diameter of 0.6m vs. approximately 400 m ~ 4,000m for the real microbursts in nature), the unique features of the outburst

flows in microburst-like winds are captured reasonably well by using the impinging-jet-based ISU microburst simulator.

In the present study, the surface pressure distribution on the test ground plane induced by the microburst-like wind was also measured before the gable-roof building models were mounted on the ground plane. Figure 7 shows the measured surface pressure coefficients on the ground plate at three different Reynolds numbers (i.e., $Re=1.2\times10^5$; $Re=1.8\times10^5$, and 2.4×10^5 respectively) along with a polynomial curve fitting to the measurement data. It can be seen that, a high static pressure region (i.e., the region with higher positive C_p values), caused by the direct impinging of the core jet flow exhausted from ISU microburst simulator, exists on the ground plane near the core center of the microburst-like wind. The size of the high pressure region was found to be much greater than the diameter of the impinging core jet flow (i.e., $r/D < 0.5$), which almost reached to the radial location of $r/D \approx 1.0$. The surface pressures on the ground in the outburst flow further away from the core region of the microburst-like wind (i.e., $r/D \geq 1.0$) was found to be quite small with the pressure coefficients (i.e., C_p values) being negative (i.e., the local surface pressure is slightly smaller than the atmospheric pressure). The measured surface pressure distribution on the ground plane was found to agree with that reported in Sengupta and Sarkar (2008) well. Similar surface pressure distributions were also reported in the previous studies of Tu & Wood (1997) and Baydar (1999).

Based on the comparison of the measurement results at three Reynolds numbers, it can be seen that the pressure distribution pattern on the ground plane was almost

independent of the Reynolds number in the range used in the present study. The significant variations of the surface pressure on the ground plane induced by the microburst-like wind also indicate that the position of the building models (i.e., where the building models were mounted) with respect to the core center of the microburst-like wind will be an important factor to determine the surface pressure distributions and the resultant wind loads acting on the building models in the microburst-like wind.

In order to reveal the turbulent nature of the microburst-like wind more clearly, the fluctuation amplitudes of the surface pressure on the ground plate were also plotted in Figure 7, where $C_{p,stdev}$ is the standard deviation of measured pressure coefficients and $C_{p,avg,0}$ is the averaged pressure coefficient at the impinging center (i.e. r/D≈0). It can be seen clearly that, while the fluctuation amplitude of the surface pressure on the ground plate was found to be relatively small in the core region of the microburst-like wind, the fluctuation amplitude was found to increase rapidly in the outburst region of the microburst-like wind, and reach its maximum value at the downstream location of r/D≈1.5~2.0. Such distribution trend of the surface pressure fluctuation on the ground plate is believed to be closely related to the high turbulence intensity levels of the microburst-like wind in the outburst flow as revealed clearly in the PIV measurement results given in Figure 5. The significant fluctuation of the surface pressure on the ground plate in the outburst region would also imply that the surface pressure distributions on the building models would also fluctuate greatly when the test models were mounted in the outburst region of the microburst-like wind, which will be discussed later in the present study.

3.2 The Effects of the Locations of the Building Models with respect to the Core Center of the Microburst-like Wind

In the present study, the effects of the mounted locations of the gable-roof building models with respect to the core center of the microburst-like wind on the vortex structures and surface pressure distributions around the building models were also assessed quantitatively. While Figure 8 gives the PIV measurement results to reveal the flow structures around the building models as they were mounted at different radial locations away from the center of the microburst-like wind, Figure 9 shows the measured surface pressure coefficients around the building models at locations corresponding to the PIV measurements. For the measurement results given in the figures, the orientation angle of the models was set to be 0 degree, i.e., the oncoming microburst-like wind (radial outflow) would be perpendicular to the roof ridges of the building models along their centerlines as shown in Figure 4.

It can be seen clearly that the flow characteristics and the surface pressure distributions around the gable-roof building models (thereby, resultant wind loads) would depend greatly on the locations of the building models with respect to the center of the microburst-like winds. As revealed clearly from the PIV measurement results given in Figure 8(a), when the models were mounted near the core center of the microburst-like wind (i.e. $r/D \approx 0$), the vertically downward jet flow was found to be impinging directly onto the roofs of the models. As a result, the models were found to be completely wrapped by high positive pressures caused by the direct impingement of the jet flow, as shown clearly in Figure 9(a). The measured surface pressure distributions and flow features were found to be very similar for the two building models in spite of

the different roof angles of the models. Corresponding to the high surface pressures on the roofs of the building models, the resultant aerodynamic forces would push the roofs downward to potentially cause roof collapse when the building models were mounted inside the core region of the microburst-like wind. It should be noted that, the geometric center of ISU downburst simulator was identified before the PIV measurements were conducted, and the building models were tried to be mounted at the geometric center of ISU downburst simulator for the test cases of $r/D \approx 0$. However, as shown in Figure 8(a), the PIV measurement results reveal that the building models were actually mounted at a location about 2% off the center of the oncoming impinging jet flow for the test cases of $r/D \approx 0$. This is a systematic error, which was be caused by the measurement error in identifying the geometric center of ISU downburst simulator or/and the non-uniformity of the oncoming impinging jet flow driven by the fan at the top of microburst simulator. It should be noted that this small systematic error will not affect the general discussions and findings derived from the present study.

As the building models were moved outward to the leading edge of the outburst flow of the microburst-like wind (i.e., $r/D \approx 0.5$), the flow features around the building models were found to become quite different, as revealed clearly from the PIV results given in Figure 8(b). While the flow streamlines far away from the building models were still found to be tilted downward, the streamlines near the ground plane were found to become horizontal and parallel to the ground plane. For the building model with 16 degree roof angle, the flow was found to stay attached to both the windward and leeward roofs of the building model. A small recirculation region was found in the wake of the

model. For the model with 35 degree roof angle, the flow was found to separate from the leeward roof of the building model, which results in a much larger recirculation region in the wake of the model. While the surface pressures on roofs of the models were found to become much smaller when the models were moved away from the core center of the microburst-like wind, the effects of the roof angle can be seen easily from the surface pressure measurement results given in Figure 9(b). The surface pressures on both the windward and leeward roofs of the 35 degree roof model were found to be greater compared with those of the 16 degree roof model, which would result in a larger aerodynamic force to cause roof collapse for the 35 degree roof the model. It should also be noted that, the surface pressure coefficients around the models were still found to be positive when models were mounted at the leading edge of the outburst flow of the microburst-like wind (i.e., r/D≈0.5). Since the surface pressure coefficients on the back walls of the models (i.e., C_p ≈0.4) were found to become much smaller compared to those on the front walls (i.e., C_p ≈1.0) due to the existence of the recirculation zone in the wakes of the models, it is expected that the resultant aerodynamic force would push the models away from the center of the simulated microburst, as expected.

As seen in the PIV measurement results given in Figure 8(c), when the models were mounted in the outburst region at the location of r/D≈1.0, while the oncoming flow was seemingly attached on both the windward and leeward roofs of the 16 degree roof model and the windward roof of the 35 degree roof model, the flow was found to separate from the roof ridge for the 35 degree roof model, which results in a very large recirculation zone in the wake of the model. The recirculation zone over the leeward roof of the model

with 35 degree roof angle was found to become much greater than that of r/D≈0.5 case, which resulted in much lower pressures on the leeward roof and back wall of the model. As shown in Figure 9(c), for the model with 16 degree roof angle, while the surface pressure coefficients on the front wall were found to be positive due to the direct impinging of the oncoming flow onto the front wall, the surface pressure coefficients on both the windward and leeward roofs, two side walls and back wall were found to become negative as the model was mounted at r/D≈1.0. It indicates that the roof of the model would lift upward, instead of being pushed downward, when the model was mounted in the outburst flow of the microburst-like wind. For the model with 35 degree roof angle, the surface pressure coefficients on both the front wall and the windward roof were found to be positive. Corresponding to the much larger recirculation zone in the wake of the model, the pressure coefficients on the leeward roof and back wall were found to be lower for the model with 35 degree roof angle, compared to those of the model with16 degree roof angle.

As the building models were moved further away from the center of the microburst-like wind (i.e., at the locations of r/D ≈ 1.5 and 2.0), while the local wind speed was found to become smaller, the streamlines of the flow were found to become tilted upward slightly as shown in Figure 8(d) and Figure 8(e). It indicates that the airflow would have vertical upward velocity components in the outflow region far away from the core center of the microburst-like wind. As shown clearly in Figure 9(d) and Figure 9(e), while the flow patterns around the building models were found to be quite similar to those of the r/D≈1.0 cases, the absolute values of the surface pressure coefficients (for

both the positive and negative surface pressure coefficients) around the models were found to become much smaller, corresponding to the smaller local wind speed at the radial locations.

In order to reveal the characteristics of the surface pressure distributions on the building models induced by the microburst-like wind more clearly, the measured surface pressures on the test models were compared with those in conventional ABL winds. Figure 10 shows the measured surface pressure profiles along the mid-planes of the two gable-roof building models with the models mounted at 4 different downstream locations (i.e., r/D≈0.50, 1.0, 1.5 and 2.0) in the microburst-like wind. Since ASCE7-05 standard for minimum design loads (ASCE, 2005) is widely used for wind load estimation of gable-roof buildings in conventional ABL winds, the standard values of the surface pressures given by ASCE 7-05 for the same gable-roof building models are also given in the figures for comparison. For the standard values of the surface pressures given by ASCE 7-05 standard, the surface pressure coefficient is defined as $C_{ph} = (P - P_{atm})/(0.5\rho U_h^2)$, where U_h is the wind speed at mean-roof-height of the building models.

As shown in Figure 10, compared with those in conventional ABL winds as given by the ASCE 7-05 standard values, the surface pressures on the gable-roof building models would become much greater (almost twice) when the models were mounted near the leading edge of the outburst flow of the microburst-like wind (i.e., r/D ≈ 0.5). It indicates that, with the same gable-roof building and the same wind speed at the mean-roof-height, the gable-roof buildings are much more likely to be damaged in microburst-

like winds compared with the case in conventional ABL winds, due to the much higher surface pressure values (thereby, resultant wind loads) induced by the microburst winds.

As mentioned earlier, since the radial flow component would become dominant in the outburst flow with the corresponding streamlines becoming parallel straight-lines in the outflow region of the microburst-like wind, the characteristics of the outburst flow would become increasingly similar to a straight-line wind. As a result, when the gable-roof building models were mounted in the outflow region far away from the center of the microburst-like winds (i.e., r/D ≈1.0, 1.5 and 2.0), the measured surface pressure profiles on both the models were found to match with the ASCE 7-05 standard values reasonably well.

It should also be noted that, unlike conventional ABL winds with the wind speed increasing monotonically above the ground, a microburst would produce an impinging-jet-like outflow profile with the maximum wind speed occurring at a much lower height close to the ground. As a result, when the 16 degree roof building model was mounted in the outflow region of the microburst-like wind, the measured surface pressures on the windward roof were found to be consistently lower, while the surface pressures on the leeward roof and back wall were found to be slightly higher, compared with the ASCE 7-05 standard values. The differences between the measured surface pressures and the ASCE 7-05 standard values were found to be much smaller for the building model with 35 degree roof angle.

3.3 The Effects of the Orientation Angles of the Building Models with respect to the Oncoming Microburst-like Wind

An experimental study was also conducted to assess the effects of the orientation angles (OA) of the gable-roof building models with respect to the oncoming microburst-like wind on the flow characteristics and the surface pressure distributions around the building models in the microburst-like wind. Figure 11 shows the measured surface pressure distributions on the two building models for OA of approximately 0.0, 45.0, and 90.0 degree, respectively. For the measurement results given in the figure, the building models were mounted in the outflow region of the microburst-like wind at r/D≈1.0. As mentioned earlier, when the model with 16 degree roof angle was mounted in the microburst-like wind at OA ≈ 0.0 deg., the surface pressure coefficients on all the surfaces of the model except the front wall were found to be negative (i.e., the local surface pressures are lower than the atmospheric pressure). The surface pressures coefficients on the windward roof of the model with 35 degree roof angle were found to be positive in addition to the front wall, due to the direct impinging of the oncoming flow onto the roof with steeper angle. Corresponding to the much larger recirculation zone over the leeward roof of the model as revealed from the PIV measurement given in Figure 8, the surface pressure coefficients on the leeward roof and rear wall of the 35 degree roof model were found to be much larger in magnitude compared with those of the building model with 16 degree roof angle.

When the building model with 16 degree roof angle was mounted at OA ≈ 45 degree with respect to the oncoming microburst-like wind, the surface pressure distribution on the windward roof of the building model was found to have a conical

shape, which is similar to that of a building with a flat roof in a conventional ABL wind at an oblique angle, as described in Banks and Meroney (2001). According to Banks and Meroney (2001), due to the suction of the strong conical roof vortices, the roof corners are the most vulnerable to damage when the oncoming flow is at an oblique angle with respect to the building axis. However, for the model with 35 degree roof angle, such conical-shaped pressure distribution could not be observed from the measured surface pressure distribution. Compared with those of the case with OA ≈ 0 degree having positive surface pressure coefficients on the windward roof, the surface pressure coefficients on the windward roof of the 35 degree roof building model were found to become negative when the building model was mounted at OA ≈ 45 degree with respect to the oncoming microburst-like wind.

When the two models were mounted at OA ≈ 90 degree with respect to the microburst-like wind, the oncoming flow would strike directly onto the gable-ended wall of the models, which results in the high pressure coefficient values (i.e., $C_p \approx 0.8 \sim 1.0$) on the windward walls. After impinging onto the gable-ended wall, the flow would separate at the roof edges along the joint between the roof and the walls. As a result, well-defined low pressure bands were found on the roofs of the building models. Since the roof ridges of the models were aligned with the oncoming flow at OA ≈ 90 deg., the surface pressure distributions on the roofs as well as the side and back walls of the two models were found to be very similar in spite of different roof angles of the two building models.

Figure 12 shows some typical examples of the PIV measurement results to illustrate the flow features around the 35 degree roof model at OA ≈ 0 degree and 45 degree with respect to the oncoming flow in the microburst-like wind. For the PIV measurement results, the laser illumination plane was set within a horizontal plane at the half eaves height of the building model. It can be seen that, when the model was mounted at OA ≈ 0 degree, the oncoming flow would strike onto the front wall of the model directly, and then separate at the sharp corners of the building model, as expected. A recirculation zone was found to form in the wake of the model. The flow features and vortex structures around the gable-roof building model were found to be very similar to those reported by Hu et al. (2011) with a gable-roof building model placed in a conventional ABL wind. For the case with the building model mounted in the microburst-like wind at OA≈45 degree, the oncoming flow was found to flow smoothly along the two side walls of the building model and then separate from the rear corners of the model, generating two very large recirculation bubbles in the wake. It should be noted that the two recirculation bubbles in the wake are similar to the sectional view of the two legs of a complicated 3D wake vortex formed in the wake of gable-roof buildings as revealed in Sousa and Pereira (2004). Since the flow features around the model for the case of OA≈90 degree were found to be quite similar to those of the OA≈0 degree case in the PIV measurement plane, the PIV measurement results for those cases are not presented here.

3.4 The Characteristics of the Resultant Aerodynamic Forces acting on the Gable-roof Building Models in Microburst-like Wind

Based on the measured surface pressure distributions around the building models described above, the resultant wind loads (i.e., aerodynamic forces) acting on the models were determined by integrating the measured pressure distributions on the surfaces of the building models. Figure 13 and Figure 14 give the radial and vertical components of the resultant aerodynamic forces acting on the building models as a function of the building location with respect to the center of the impinging jet. In the present study, the mean aerodynamic force coefficients, CF_r and CF_Z, are defined as $CF_r = F_X/(0.5\rho U_{jet}^2 A_r)$ and $CF_Z = F_Z/(0.5\rho U_{jet}^2 A_Z)$, where F_r and F_Z are the mean values of radial and vertical components of the resultant aerodynamic forces acting on the models. A_r and A_Z are the projected areas of the models in *r* and *Z* directions as defined in Figure 4. Since the azimuthal components of the resultant aerodynamic forces were found to be always insignificant due to the axis-symmetric nature of the oncoming microburst-like wind and the symmetry of the building models relative to the oncoming flows, thereby, the measurement results are not presented here.

From the measurement results shown in Figure 13, it can be seen that the variations of the radial components of the aerodynamic forces (i.e. F_r) acting on the models have a very similar trend for all the test cases. Since the streamlines of the airflow within the core region of the microburst-like wind were mainly vertically downward, the radial components of the resultant aerodynamic forces (i.e. F_r) were found to be very small when the models were mounted near the core center of the microburst-like wind. As

revealed from the PIV measurements given in Figure 5, the radial flow velocity component would increase rapidly as the distance from the core center of the microburst-like wind increases, and become dominant in the outburst region (r/D>0.5) of the microburst-like wind. The flow velocity was found to reach its maximum value at the location of r/D≈1.0, and then decrease slowly with increasing radial distance from the core center of the microburst-like wind. As a result, the radial components of the aerodynamic forces acting on the building models (i.e. F_r) were found to increase rapidly, reach their peak values at the downstream location of r/D≈1.0, and then decrease gradually due to the decreasing wind speed at the further downstream locations.

The effects of the roof angle on the resultant radial aerodynamic forces acting on the building models are also revealed clearly from the comparison of the measurement results given in Figure 13. When the models were mounted at OA≈0 degree with respect to the oncoming flow, the model with a larger roof angle (i.e. 35 degree roof building) was found to experience a greater radial aerodynamic force in the outwardly direction. As the orientation angle increases (i.e. for cases with OA ≈ 45 degree and 90 deg.), the differences in the radial components of the resultant aerodynamic forces between the two building models with different roof angles were found to become smaller and smaller.

As shown from the measured surface pressure distributions given in Figure 9(a), the two gable-roof building models would experience high positive pressures over their envelopes (i.e. $C_P \approx 1.0$) when the models were mounted near the core center of the

microburst-like wind (r/D≈0.0), due to the direct impinging of the downdraft onto the models. Corresponding to the high surface pressures on the roofs, the vertical components (i.e. F_Z) of the resultant aerodynamic forces acting on the models were found to be quite significant, i.e., CF_Z≈-0.9 ~ -1.0, as shown in Figure 14. The negative sign of CF_Z indicates that the resultant loads on the roof would be downward that would potentially cause collapse of the roof by pushing it down.

The variations of the vertical aerodynamic forces acting on the building models as a function of the position of the models are found to be closely related to the unique features of the microburst-like wind. As shown in Figure 5, the surface pressures on the ground plane would decrease with the increasing radial distance away from the core center of the microburst-like wind. As a result, the magnitude of the resultant downward aerodynamic forces acting on the models were found to decrease rapidly as the building models were moved away from the core center the microburst-like wind. As shown in Figure 14, when the models were moved into the outburst region of the microburst-like wind (i.e., at the radial position r/D ≥ 0.75), the coefficients of the vertical aerodynamic forces, CF_Z , were found to change their signs from negative to positive, which indicates that the resultant aerodynamic forces acting on the roof would be uplift. The uplift forces acting on the models were found to reach the peak values at the radial location of r/D≈1.0, and then decrease slowly as the models were mounted further away from the core center of the microburst-like wind.

The effects of the roof angle and orientation angle of the building models on the vertical- components of the resultant aerodynamic forces acting on the test models can

also be seen clearly from the comparisons of the measurement results given in Figure 14. It can been seen clearly that, when the models were placed near the core center of the microburst-like wind (r/D≈0.0), the vertical aerodynamic force coefficients of the two models, CF_Z , were found to be almost the same (i.e., $CF_Z \approx$-1.0) in spite of the different roof angles. As the building models were moved away from the core region into the outflow region of the microburst-like wind, the uplift forces acting on the model with smaller roof angle was found to be much greater than those with a larger roof angle when the models were mounted at OA ≈ 0 degree with respect to the oncoming microburst-like wind. The differences in the uplift forces were found to become smaller and smaller as the orientation angle increases.

In the present study, a set of experiments were also conducted to quantify the resultant wind loads acting on the building models at different Reynolds numbers of the microburst-like wind (i.e., Re = 1.2×10^5 ~ 2.4×10^5) by changing the velocity of the impinging jet flow exhausted from the microburst simulator. It was found that the characteristics of both radial and vertical aerodynamics forces acting on the models were be almost independent of the Reynolds number levels of the microburst-like wind within the range of the present study.

3.5 The Fluctuations of the Surface Pressures on the Gable-roof Building Models in Microburst-like Wind

While the time-averaged pressure measurement results given above are very helpful to reveal the global features of the wind loads acting on gable-roof buildings induced by violent microburst-like wind, it would be very insightful and essential to take the

turbulent nature of the microburst-like wind into account in order to assess its damage potential more accurately. In the present study, the fluctuations of the surface pressures on the gable-roof models were also investigated for a better understanding of the turbulent of the microburst-like wind.

Figure 15(a) shows the time series of the instantaneous surface pressure measurement results obtained from the same pressure tap on the windward roof of the 16 degree roof model (i.e. the selected point #1 shown in Figure 15(b)) as the building model was mounted at different radial locations in the microburst-like wind. It can be seen clearly that the instantaneous surface pressures at the same pressure tap would fluctuate much more significantly as the model was moved away from the core region into the outburst region of the microburst-like wind.

The fluctuation amplitudes of the instantaneous surface pressures at two typical positions on the building model as a function of the radial location of the model with respect to the core center of the microburst-like wind are given in Figure 15(b). In this figure, P_{stdev} denotes the standard deviations of the instantaneous surface pressure data; $P_{avg,0}$ represents the time-averaged values of the surface pressure at the selected points when the model was mounted at the core center of the microburst-like wind (i.e. $r/D \approx 0$). The turbulence kinetic energy level of the microburst-like wind at the mean roof height were also plotted in Figure 15(b) in order to elucidate the close relationship between the characteristics of the surface pressure fluctuations on the building model and the variations of the turbulence level in the microburst-like wind. As revealed clearly in Figure 15(b), the fluctuation amplitudes of the surface pressures at the selected points

were found to be quite small when the building model was mounted within the core region of the microburst-like wind, corresponding to the low turbulence level in the core region of the microburst-like wind. The amplitudes of the surface pressure fluctuations were found to increase very rapidly as the building model was moved away from the core region into the outburst region of the microburst-like wind, and reach their maximum values at r/D≈1.5 due to the highest turbulence intensity at the downstream location. The pressure fluctuation amplitudes were then found to decrease as the model was moved further downstream, corresponding to the decreasing turbulence intensity level in the outflow region further away from the center of the microburst-like wind. From the comparison of the measurement results at the two selected points, it is interesting to note that the surface pressure fluctuations on the windward roof of the building model (i.e. Point #1) were found to be always greater than those on the leeward roof (i.e. Point #2). The observation was also believed to be closely related to the vortex structures and turbulent characteristics of the flow field around the building models in the microburst-like wind. Since Point #1 was located at the leading edge of the windward roof, the fluctuation of the surface pressure at this point was mainly determined by the turbulence intensity level of the oncoming microburst-like wind. However, since flow separation was found to occur over the ridge of the building model to form a large separation bubble sitting over the leeward roof as shown clearly in Figure 8, the fluctuation of the surface pressure at Point #2 would be decoupled from the oncoming flow and affected mainly by the separation bubble on the leeward roof. A completely different outcome would be expected for the same building model when

placed in a conventional ABL wind due to the significant difference in the flow characteristics of the oncoming flow (Hu et al. 2011). It should be noted that, larger fluctuation amplitude of the surface pressures on the same building model would imply a higher peak wind load acting on the building model, which would increase the damage potential of the gable-roof building in microburst-like wind. Since the characteristics of the surface pressure fluctuations on the building model with 35 degree roof angle were found to be very similar to those of the 16 degree roof angle model described above, the measurement results for the 35 degree roof model are not presented here.

4. Conclusions

An experimental study was conducted to investigate the flow characteristics of microburst-like wind and to assess the resultant wind loads acting on low-rise gable-roof buildings induced by the microburst-like wind. The experiments were carried out by using an impinging-jet-based microburst simulator in the Department of Aerospace Engineering of Iowa State University with two gable-roof building models of different roof angles for the comparative study. In addition to measuring the surface pressure distributions (thereby, the resultant aerodynamic forces) around the building models, a high-resolution digital Particle Image Velocimetry (PIV) system was used to conduct flow field measurements to reveal the vortex structures and turbulent flow characteristics around the test models in the microburst-like wind. The effects of important parameters, such as the distance between the center of the microburst-like winds and the models, the roof angle and the orientation angles of the building models with respect to the oncoming microburst-like wind, and the Reynolds numbers of the microburst-like flow,

on the characteristics of the flow fields and the surface pressure distributions around the building models as well as the resultant aerodynamic forces acting on the test models were assessed quantitatively.

The PIV measurements reveal clearly that, the flow streams in the core region of the microburst-like wind, which are mainly vertical pointing downward before impinging onto the ground plane, would turn rapidly at right angle after impinging onto the ground plane. The flow streamlines were found to become parallel to the ground plane in the outflow region with high-speed flow concentrated within a layer close to the ground plate. While diverging from the core center of the microburst-like wind, the outburst flow was found to accelerate at first, reach its maximum wind speed at the location of $r/D \approx 1.0$, and then slow down gradually further downstream. While the turbulence intensity level inside the core region of the microburst-like wind was found to be quite small, the turbulence intensity was found to increase rapidly in the outburst flow region with highest turbulence intensity occurring at the location of $r/D \approx 1.5$. The high turbulence level in the outburst flow was found to be responsible for the significant fluctuations of the surface pressures on the building models when the models were mounted in the outflow region of the microburst-like wind.

It was also found that the surface pressure distributions and the resultant wind loads (i.e., aerodynamic forces) acting on the models would change significantly depending on the roof angles, the orientation angles, and the locations of the building models with respect to the core center of the microburst-like wind. When mounted within the core region of the microburst-like wind ($r/D \leq 0.5$), the building models were found to

experience high positive pressures on the entire envelope due to the direct impinging of the vertically-downward core jet flow onto the test models. The resultant aerodynamic force was found to be acting vertically-downward on the roof. As the building models were moved away from the core region toward the outflow region of the microburst-like wind, while the vertical components of the resultant aerodynamic forces were found to decrease rapidly, the horizontal components of the aerodynamic forces were found to become bigger and bigger until reaching the peak values at r/D≈1.0. When the building models were moved further downstream (i.e. r/D≥1.0), while the magnitude of the aerodynamic forces acting on the models were found to decrease gradually corresponding to the decreasing wind speed, the vertical components of the resultant aerodynamic forces were found to become uplift forces. Compared with those in conventional atmospheric boundary layer (ABL) winds as specified in ASCE 7-05, the gable-roof building models were found to experience much higher (i.e. almost double) surface pressures, thereby, much larger wind loads when the test models were mounted at the leading edge of the outburst flow of the microburst-like wind (i.e. r/D ≈ 0.50). Since the flow characteristics of the microburst-like wind in the outflow region would become increasingly similar to conventional ABL winds, the measured surface pressure profiles on the building models were found to agree with the ASCE 7-05 standard values reasonably well when the test models were mounted in the outflow region far away from the core center of the microburst-like wind.

In addition to the time-averaged measurement results that revealed the global features of the microburst-like wind and the resultant wind loads acting on the building models

induced by the microburst-like wind, the standard deviations of the measured instantaneous surface pressures on the building models were used to assess the turbulent nature of the microburst-like wind. It was found that, corresponding to the high turbulence levels in the outburst flow of the microburst-like wind, the surface pressures on the models were found to fluctuate significantly as the models were mounted in the outflow region. The large fluctuation amplitudes of the surface pressures on the test models would imply significant peak wind loads acting on the building models, which would greatly increase the damage potential of low-rise gable-roof buildings subject to microburst-like wind.

Acknowledgments

The project is funded by National Science Foundation (NSF) under award number CMMI-1000198. The authors also want to thank Mr. Bill Rickard of Iowa State University for his help in manufacturing the test models and setting of the experiments.

References

ASCE 7-05 (2005). ASCE Standard, Minimum Design Loads for Buildings and Other Structures ASCE 7-05, American Society of Civil Engineers (ASCE), New York, USA, 2005.

Alahyari A, Longmire EK (1995) "Dynamics of Experimentally Simulated Microbursts," *AIAA Journal,* 33(11): 2128-2136.

Atlas D, Ulbrich CW, Williams CR (2004) Physical Origin of a Wet Microburst: Observations and Theory. J Atmos Sci, 61: 1186-1196

Banks D, Meroney RN (2001) A model of roof top surface pressure produced by conical vortices: model development. Wind and Structure, 4(3): 227-246

Baydar E (1999) Confined impinging air jet at low Reynolds numbers. Experimental Thermal and Fluid Science 19:27-33

Bluestein HB, Golden JH, (1993). A review of tornado observations. The Tornado: Its Structure, Dynamics, Prediction and Hazards, Geophysics Monogram, vol. 79, American Geophysics Union, p.19.

Chay MT, Albermani F, Wilson R. (2005) Numerical and analytical simulation of downburst wind loads. Eng Struct 28: 240-254.

Chay MT, Letchford, CW (2002) Pressure distributions on a cube in a simulated thunderstorm downburst, Part A: stationary downburst observations. J Wind Eng Ind Aerod 90: 711-732.

Choi ECC (2004) Field measurement and experimental study of wind speed profile during thunderstorms. J. Wind Eng. 92: 275-290

Das KK, Ghosh AK, Sinhamahapatra KP (2010) Investigation of the axisymmetric microburst flow field. J Wind Eng Ind Aerod 7: 1-15.

Fujita TT (1979) Objectives, operations and results of project NIMROD. Preprint, 11th conf. on Severe Local Storms. Kansas City. Amer. Meteor. Society;

Fujita TT (1985) The Downburst: Microburst and Macroburst. University of Chicago Press, Chicago

Hjelmfelt MR (1987) The microbursts of 22 June 1982 in JAWS. J Atmos Sci 44(12):1646-1665;

Hjelmfelt MR (1988) Structure and life cycle of microburst outflows observed in Colorado. J Appl Meteorol 27(8): 900-927

Holmes JD (1999) Modeling of Extreme Thunderstorm Winds for Wind Loading of Structures and Risk Assessment. Wind Engineering into the 21st Century, Proc. of the 10th Intl. Conf. on Wind Eng. eds. A. Larsen et al, Denmark, June 1999, 1409−1415

Holmes JD, Oliver, SE (2000) An empirical model of a downburst. Eng Struct 22: 1167-1172.

Hu H, Yang Z, Sarkar P, Haan F (2011) Characterization of the Wind Loads and Flow Fields around a Gable-roof Building Model in Tornado-like Winds. Experiments in Fluids, Vol.51, No.3, pp 835-851.

Kaimal JC, Finnigan JJ (1994) Atmospheric Boundary Layer Flows: Their Structure and Measurement. Oxford University Press, Inc., 10-16

Kanda M, Maruta E (1993) Characteristics of fluctuating wind pressure on long low-rise buildings with gable roofs. J Wind Eng Ind Aerodyn 50:173–182.

Kim J, Hangan H (2007) Numerical simulation of impinging jets with application to downbursts. J Wind Eng Ind Aerod 95: 279-298

Krishna P (1995) Wind loads on low rise buildings – A review. J Wind Eng Ind. Aerod.54/55:383-396

Letchford CW, Chay MT (2002) Pressure distributions on a cube in a simulated thunderstorm downburst, Part B: moving downburst observations. J Wind Eng Ind Aerod 90: 733–753.

Letchford CW, Illidge G (1999) Turbulence and Topographic effects in Simulated Thunderstorm Downdrafts by Wind Tunnel Jet. Wind Engineering into the 21st Century, Proceedings of the Tenth International Conference on Wind Engineering. eds. A. Larsen G. L. Larose and F. M. Livesey, Denmark, June 1999, 1907-1912.

Liu Z, Prevatt DO, Aponte-Bermudez LD, Gurley K, Reinhold T, Akins RE (2009) Field measurement and wind tunnel simulation of hurricane wind loads on a single family dwelling. Eng. Struct 31(10):2265–2274.

Mason MS, Letchford CW, James DL (2005) Pulsed wall jet simulation of a stationary thunderstorm downburst, Part A: Physical structure and flow field characterization. J Wind Eng Ind Aerod 93: 557-580.

Nicholls M, Pielke R, Meroney R (1993) Large eddy simulation of microburst winds flowing around a building. J Wind Eng Ind Aerod 46: 229-237.

Peterka JA, Hosoya N, Dodge S, Cochran L, Cermak JE (1998) Area average peak pressures in a gable roof vortex region. J Wind Eng Ind Aerodyn 77–78(1):205–215

Savory E Parke GAR, Zeinoddini M, Disney P (2001) Modelling of tornado and microburst-induced wind loading and failure of a lattic transmission tower. EngStruct. 23: 365-375.

Selvam, R.P., Holmes, J.D. (1992) Numerical simulation of thunderstorm downdrafts. J Wind EngIndAerod 44: 2817-2825.

Sengupta A, Sarkar P (2008) Experimental measurement and numerical simulation of an impinging jet with application to thunderstorm microburst winds. J Wind Eng Ind Aerod 96: 345-365.

Sousa JMM (2002) Turbulent flow around a surface-mounted obstacle using 2D–3C DPIV. Exp Fluids 33:854–862.

Sousa JMM, Pereira JCF (2004) DPIV study of the effect of a gable roof on the flow structure around a surface-mounted cubic obstacle. Exp Fluids 37:409–418.

Stathopoulos T, Wank K, Wu H (2001) Wind pressure provisions for gable roofs of intermediate roof slope. Wind Struct 4:119–130

Tu CV, Wood DH (1996) Wall Pressure and Shear Stress Measurements Beneath an Impinging Jet. Experimental Thermal and Fluid Science 13: 264-373.

Uematsu Y, Isyumov N (1999) Wind pressures acting on low-rise buildings. J Wind Eng Ind Aerod82: 1-25.

Vasiloff S, Howard K (2008) Investigation of a Severe Downburst Storm near Arizona, as Seen by a Mobile Doppler Radar and the KIWA WSR-88D. Weather and Forecasting; 24, 856-867.

Wilson JW, Roberts RD, Kenssiger C, McCarthy J (1984) Microburst wind structure and evaluation of Doppler radar for airport wind shear detection. J Clim Appl Meteorol 23: 898-915.

Wood GS, Kwok CS, Motteram NA, Fletcher DF (2001) Physical and numerical modelling of thunderstorm downbursts. J Wind Eng Ind Aerod 89: 535–552.

Yang Z, Sarkar P, Hu H (2011) "An experimental study of flow field around a high-rise building model in tornado-like winds", *Journal of Fluids and Structures,* 27(4): pp471-486.

Zhang Y, Sarkar PP, Hu H (2012) Experimental and Numerical Investigations on the Flow Characteristics of Microburst-like Winds. 50th AIAA Aerospace Sciences Meeting including the New Horizons Forum and Aerospace Exposition 09 - 12 January 2012, Nashville, Tennessee, AIAA 20121197

Table 1. *Primary design parameters of the building models used in present study*

Test Model	Model #1 with 16 deg. roof angle		Model #1 with 35 deg. roof angle	
	Absolute value (mm)	Non-dimensional value (L/D)	Absolute value (mm)	Non-dimensional value (L/D)
Mean roof height of the test model	36.0	0.059	36.0	0.059
Eave height of the test model	31.0	0.051	25.0	0.041
Total height of the test model	38.5	0.063	41.5	0.068
Base size of the test model	65.0	0.107	65.0	0.107
Mounted location of the model relative to the microburst simulator center	r/D ≈ 0, 0.5, 1.0, 1.5, 2.0		r/D ≈ 0, 0.5, 1.0, 1.5, 2.0	

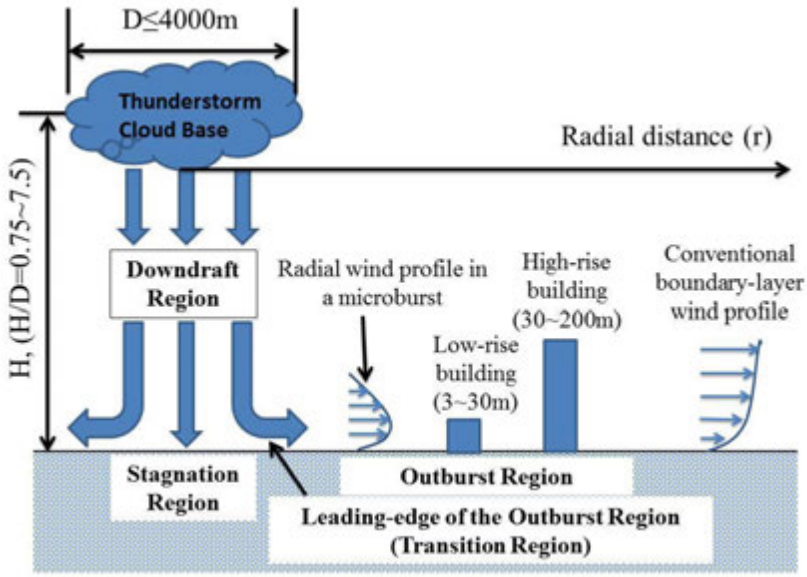

Figure 1. *Schematic of a microburst*

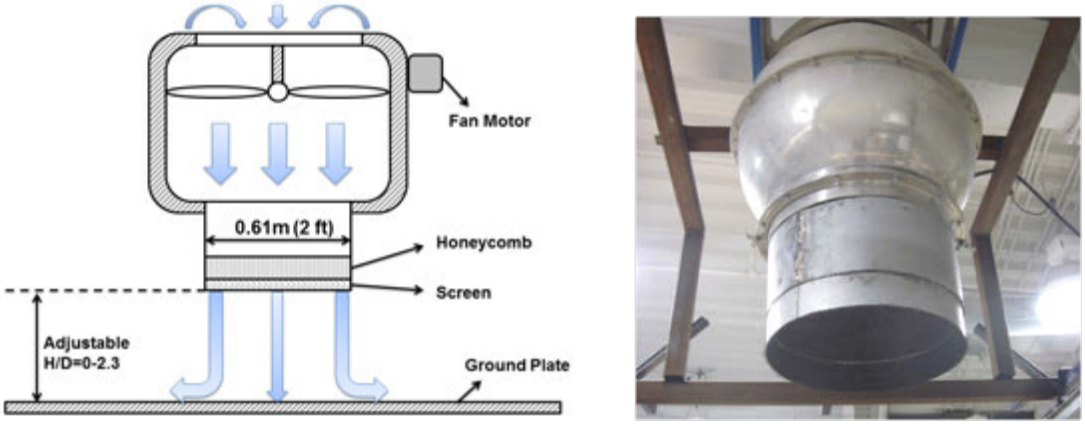

Figure 2. *A schematic and photo of ISU microburst simulator*

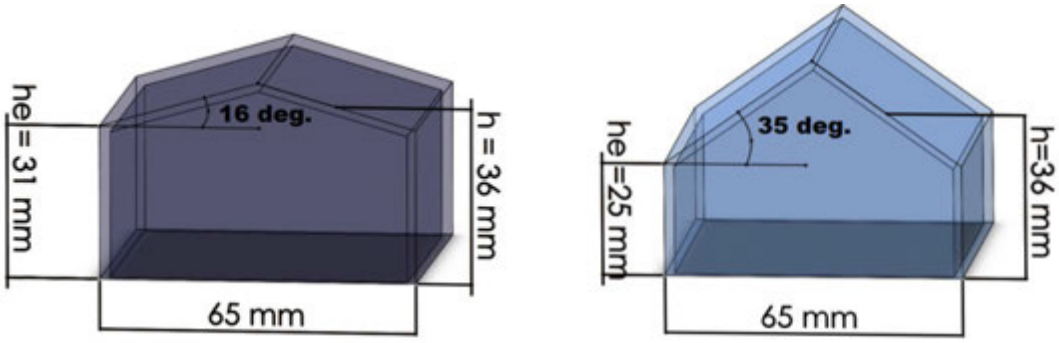

(a). Prospective views of the two gable-roof building models

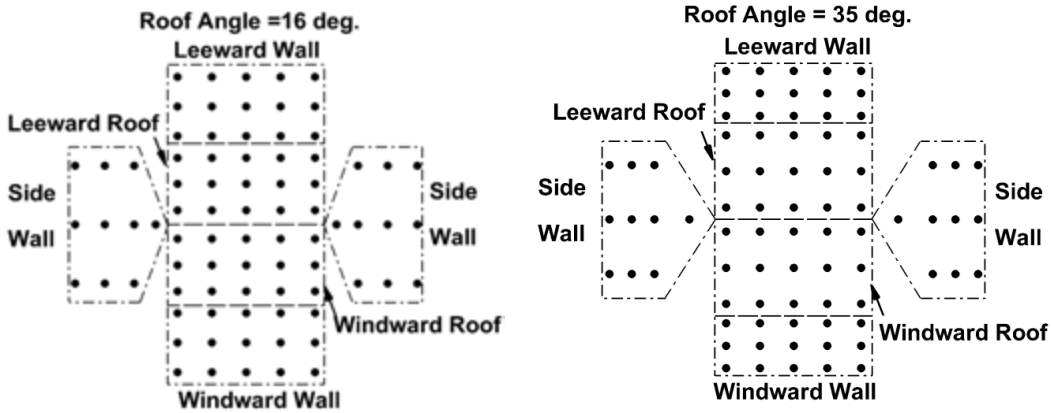

(b). Stretched-out view of the building models to show the locations of the pressure taps

Figure 3. *The schematic of the two gable-roof building models used in the present study*

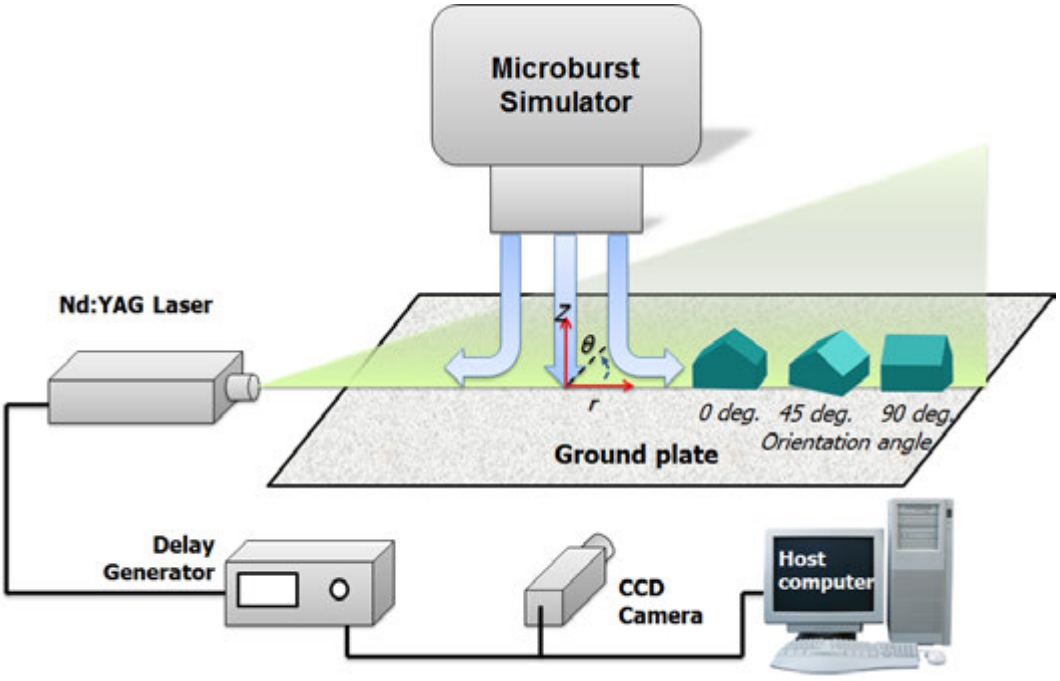

(a). The experimental setup for PIV measurements

(b). Layout of the PIV measurement windows

Figure 4. *Schematic of the experimental setup used in the present study*

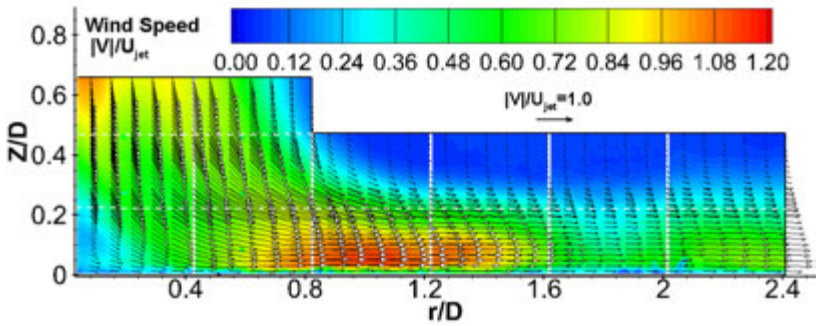

(a). Time-averaged flow velocity vectors

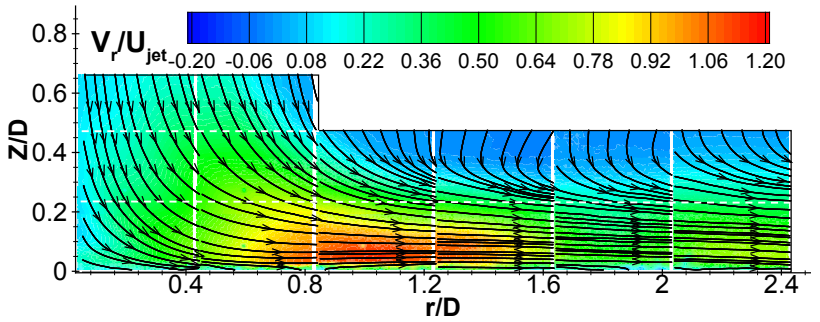

(b). Distribution of radial velocity, V

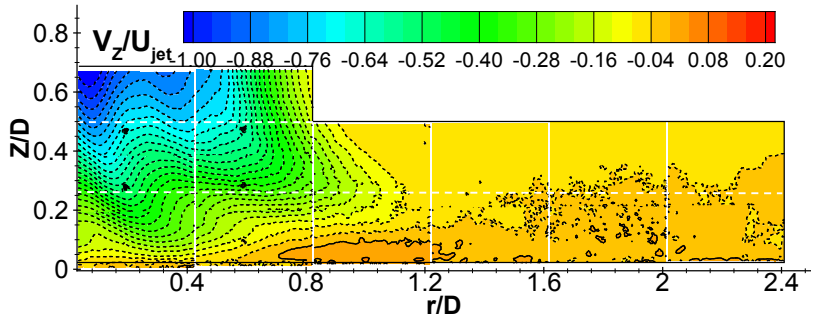

(c). Distribution of vertical velocity, V_Z

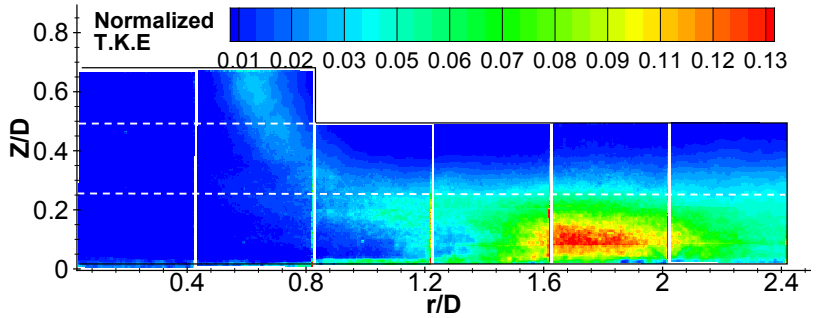

(d). Distribution of turbulence kinetic energy (T.K.E)

Figure 5. *PIV measurement results of the microburst-like wind*

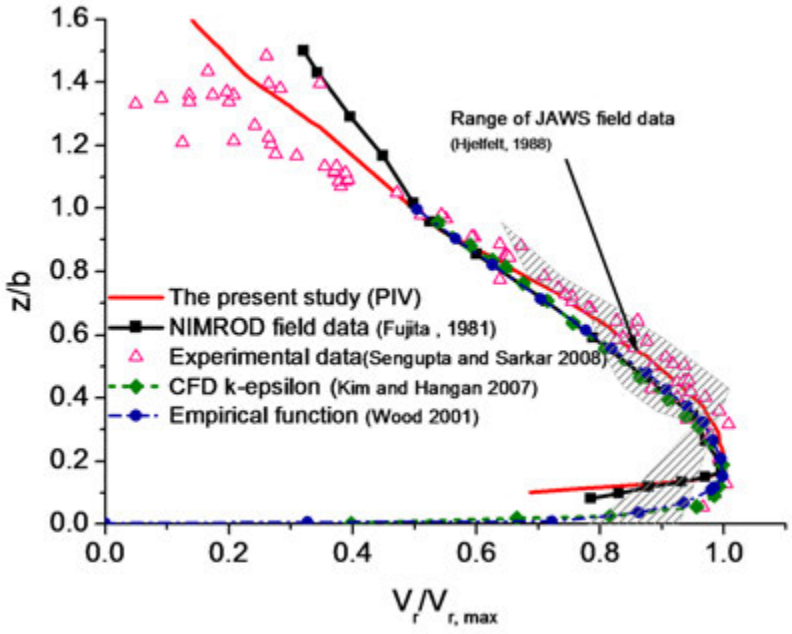

Figure 6. *The measured outflow velocity profile versus the field measurement data of microbursts occurring in nature and the published results of previous studies*

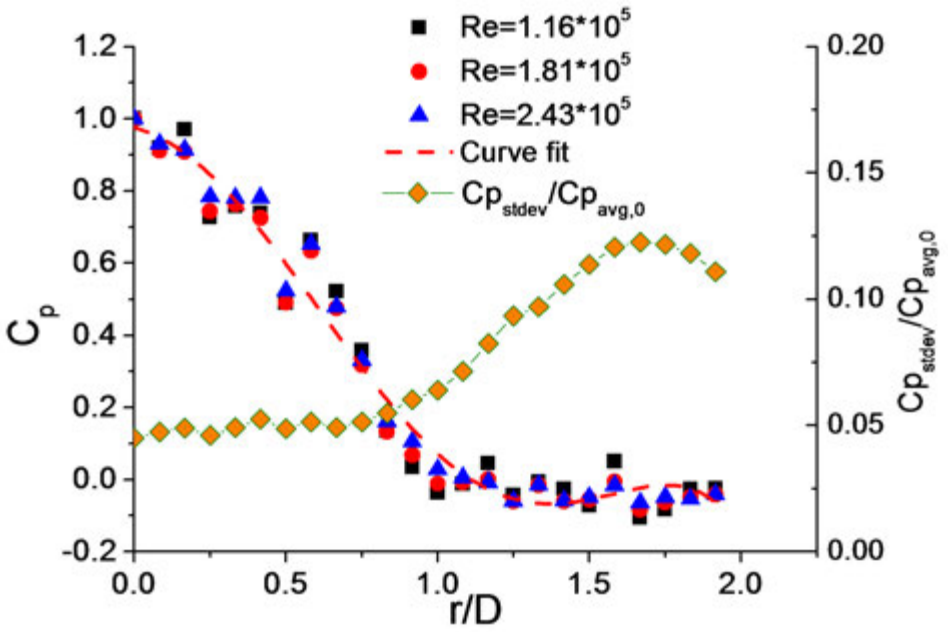

Figure 7. *The measured surface pressure distributions on the ground plane*

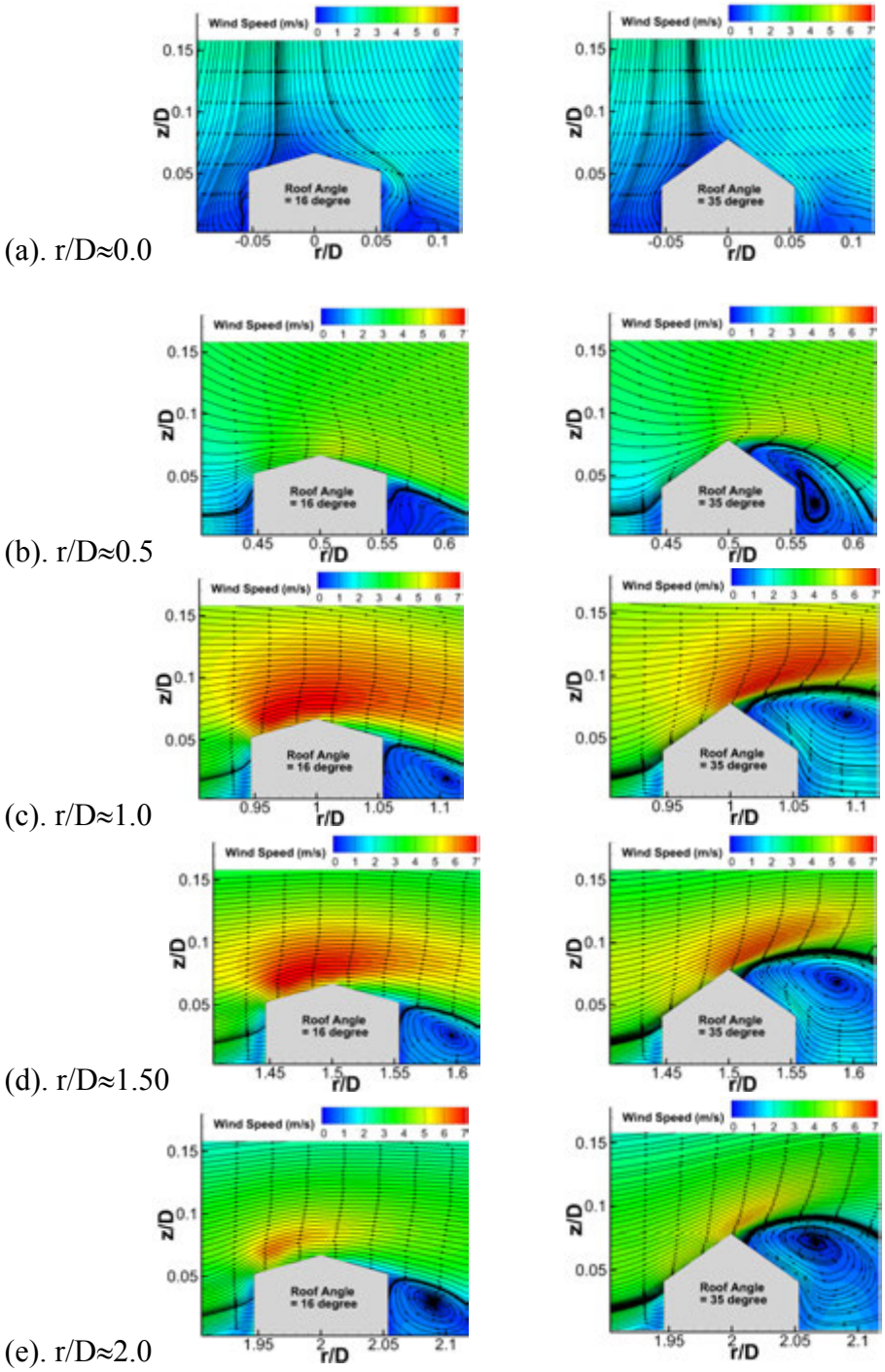

Figure 8. *PIV measurement results with the building models mounted at different locations (left: building model with 16 degree roof angle; right: building model with 35 degree roof angle)*

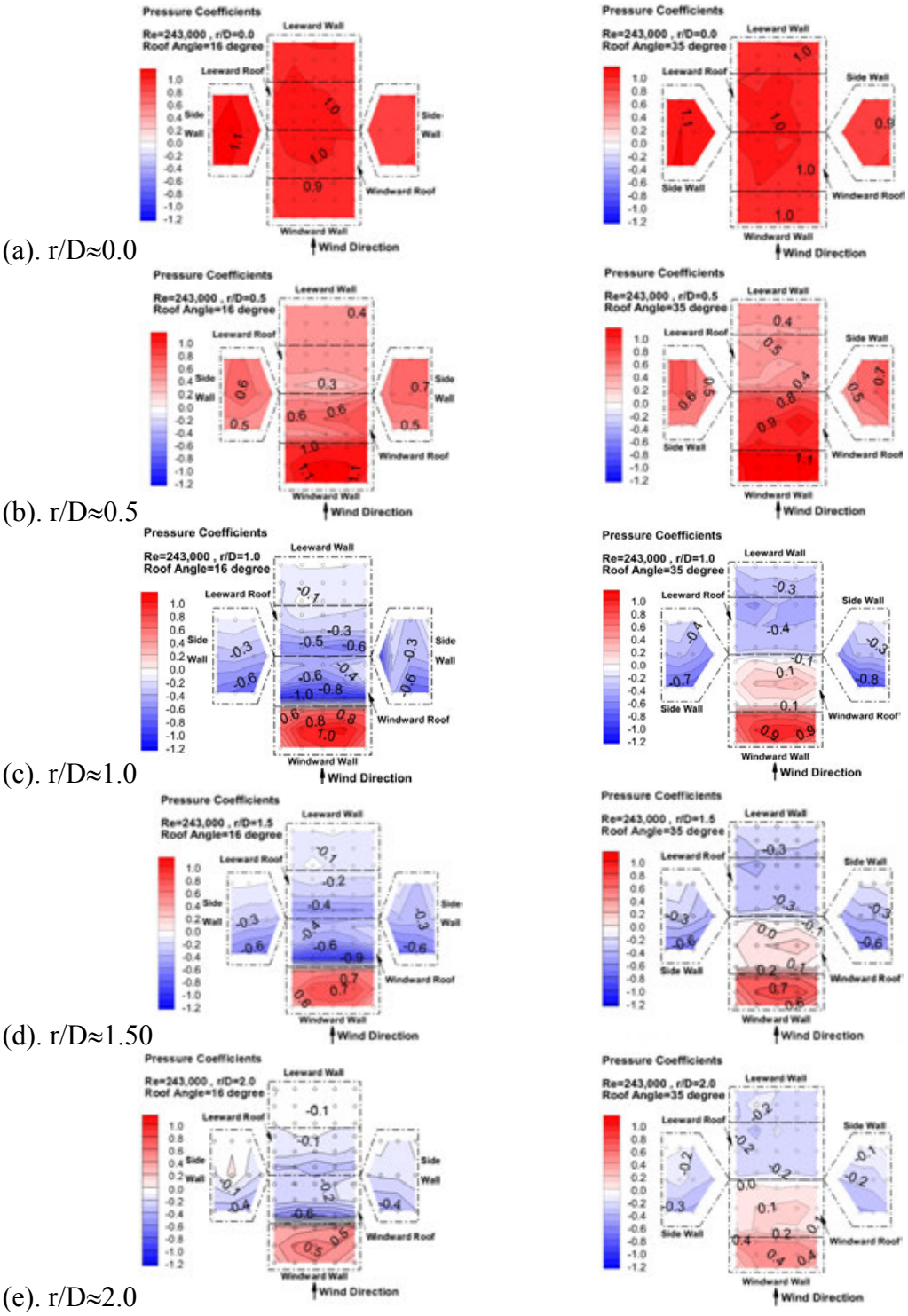

(a). r/D≈0.0

(b). r/D≈0.5

(c). r/D≈1.0

(d). r/D≈1.50

(e). r/D≈2.0

Figure 9. *Surface pressure distributions with the building models mounted at different locations (left: building model with 16 degree roof angle; right: building model with 35 degree roof angle)*

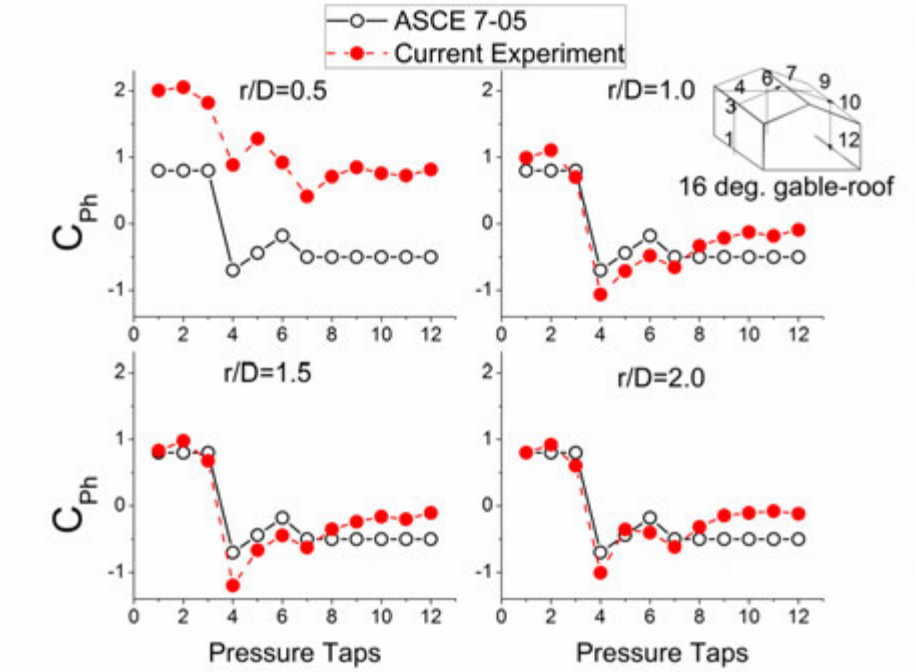

(a). the building model with 16 degree roof angle

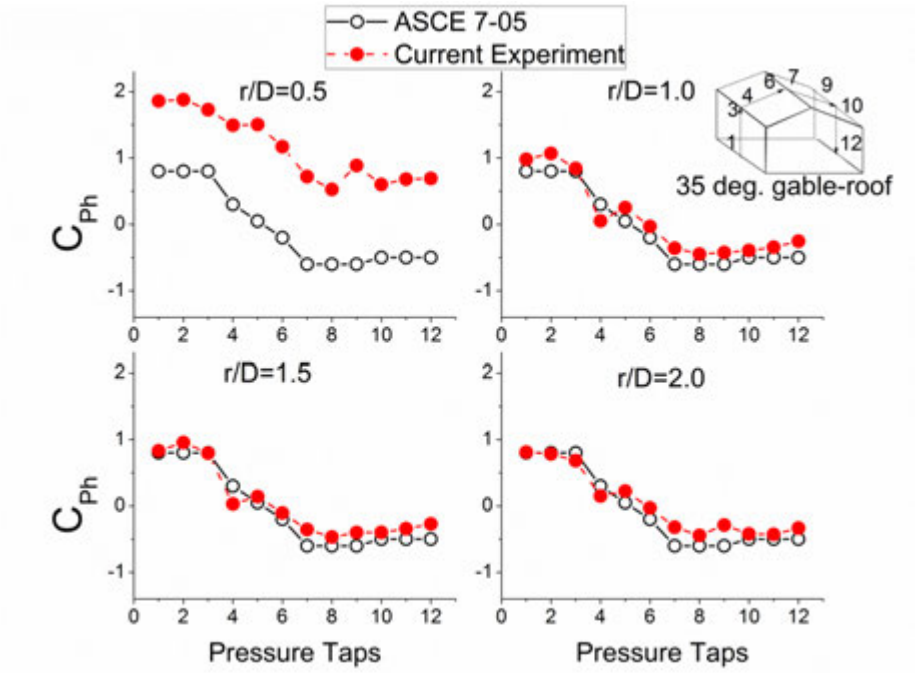

(b). the building model with 35 degree roof angle

Figure 10. *The measured surface pressure coefficient Profiles along the centerlines of the building models in microburst-like wind versus the standard values of ASCE 7-05.*

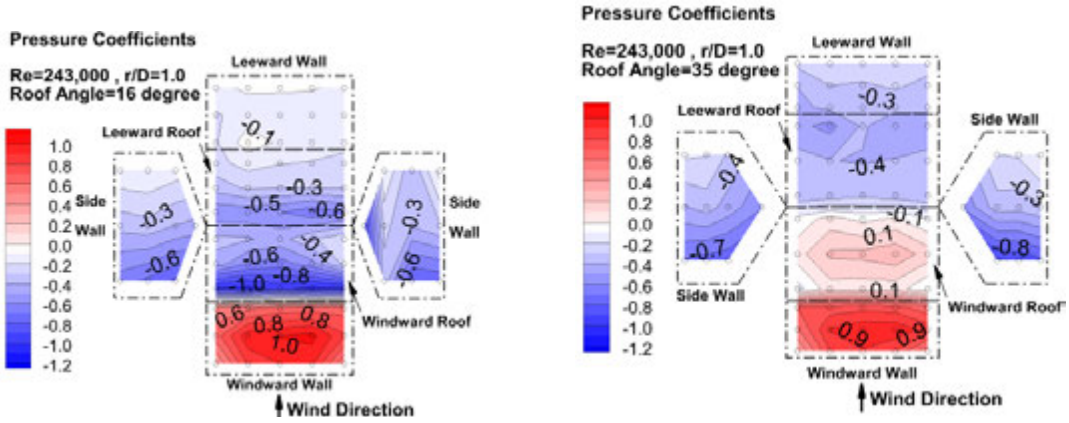

(a). OA≈ 0 deg.

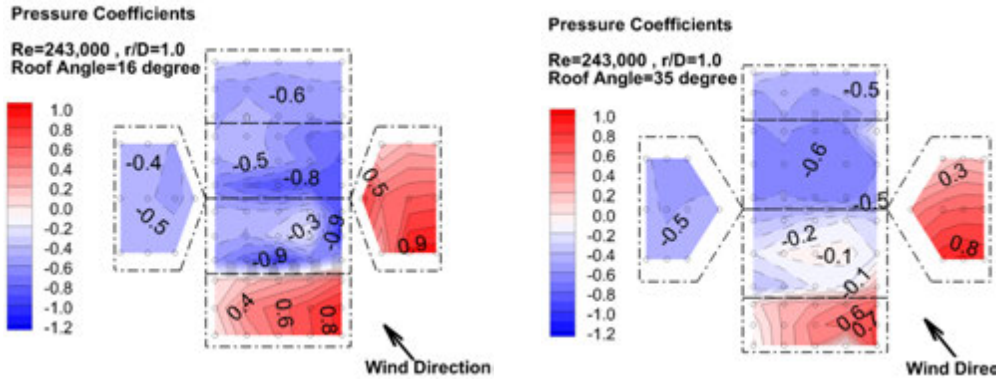

(b). OA≈45 deg.

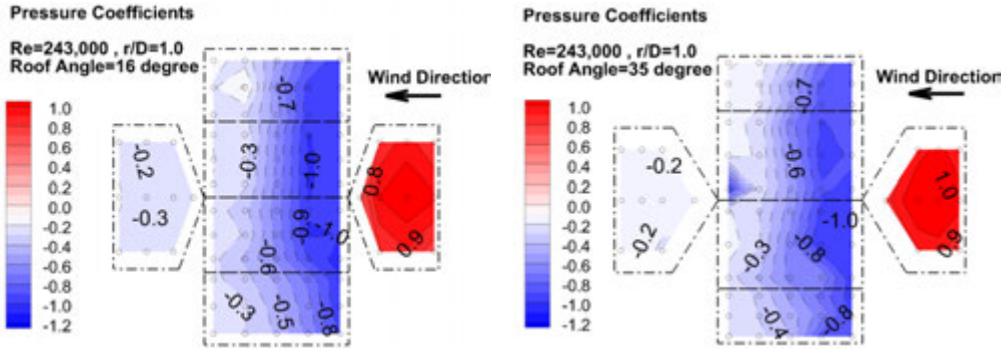

(c). OA≈ 90 deg.

Figure 11. *The pressure distributions around the building models at different orientation angles. (left: building model with 16 degree roof angle; right: building model with 35 degree roof angle)*

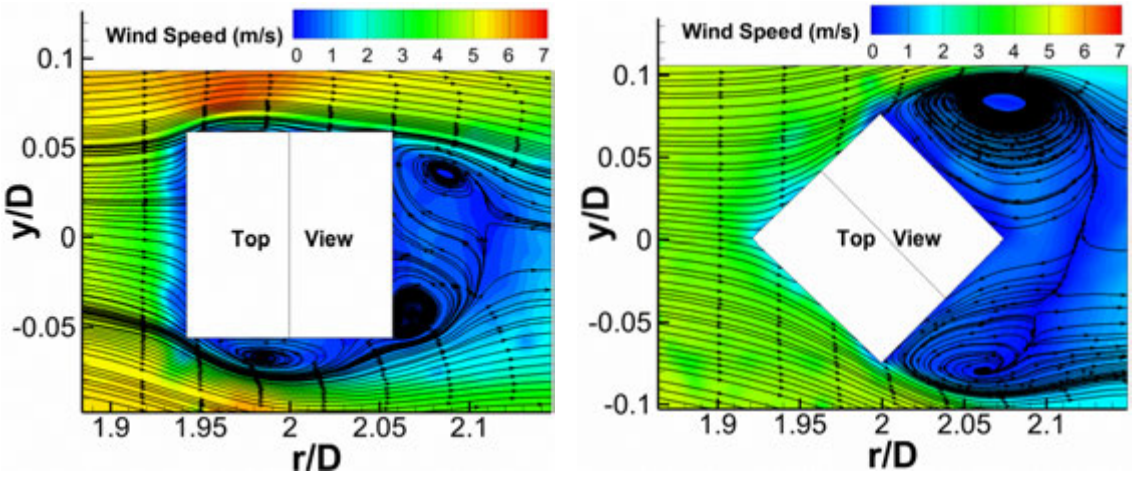

(a). **OA≈** 0 deg. (b). **OA≈** 45 deg.

Figure 12. *Flow field around the 35 degree roof building model at different orientation angles with respect to the oncoming microburst-like wind.*

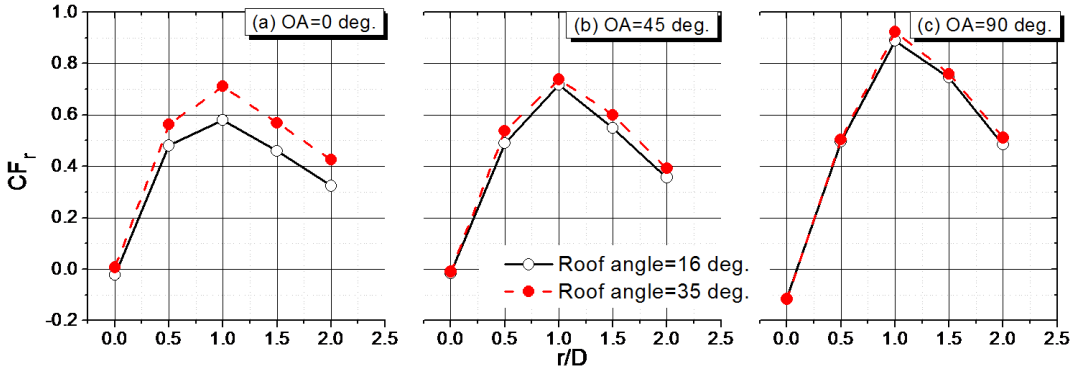

Figure 13. *Measured radial components of the aerodynamic forces acting on the building models*

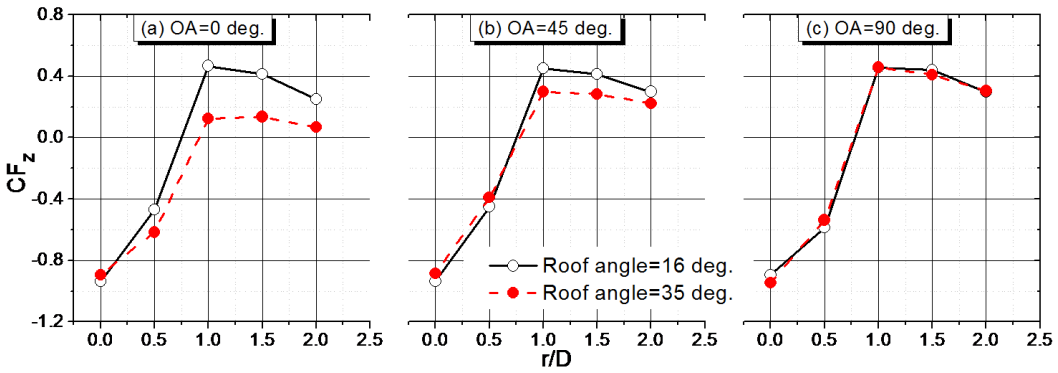

Figure 14. *Measured vertical components of the aerodynamic forces acting on the building models*

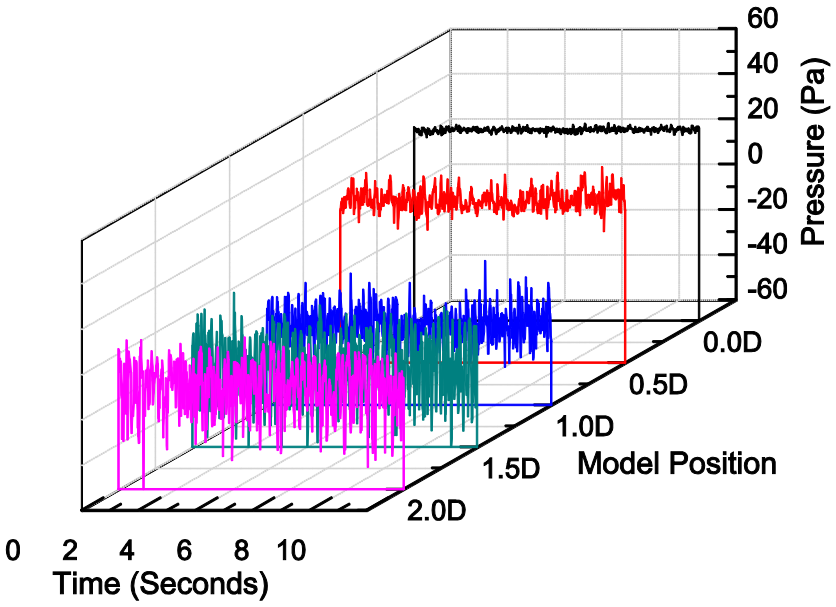

(a). Time series of the instantaneous surface pressure measurement results

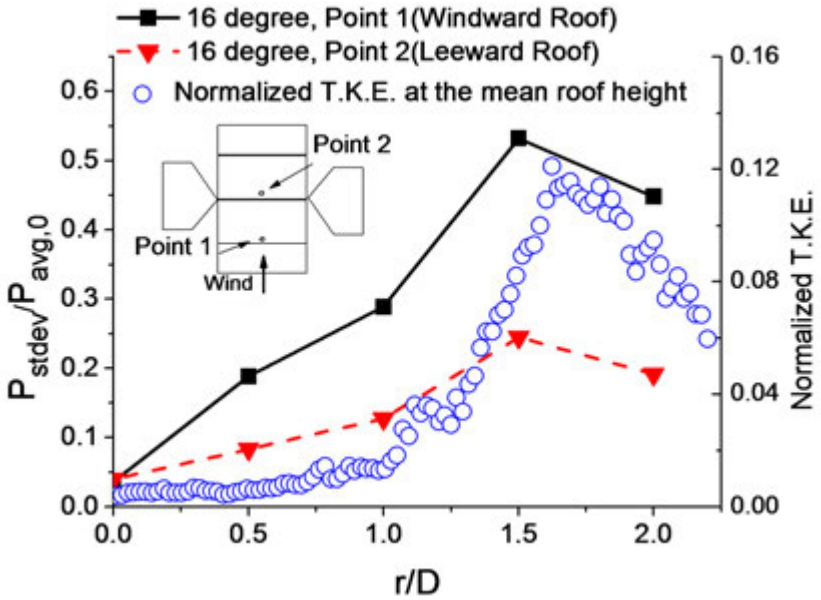

(b). The fluctuation amplitudes of the surface pressures at two selected points

Figure 15. *Fluctuation of the surface pressures on the building model with 16 degree roof angle in the microburst-like wind.*

CHAPTER 4

STUDY OF MICROBURST-WIND LOADS ON LOW-RISE BUILDING MODELS WITH DIFFERENT GEOMETRIC SHAPES

Yan Zhang, Hui Hu, Partha P. Sarkar

Department of Aerospace Engineering, Iowa State University, Ames, Iowa, 50010

Abstract: Microburst can produce downdraft and strong divergent outflow wind, whose characteristics are distinct from the atmospheric boundary layer (ABL) wind. In the present study, microburst-wind loading effects on a cube-shaped building, a grain bin and two gable-roofed building models are evaluated and compared by performing laboratory tests. Velocity and turbulence intensity profiles at selected locations are revealed. The distribution of mean and root-mean-square pressure coefficients are shown for selected cases. Results suggested that the wind loading effects changed significantly as the radial location and geometric shape changed. At or near the center of the microburst, high external pressure was found for all building models, resulting in a large downward force on the roof. In the outburst region, the distribution of pressure coefficients was similar to those found in the ABL wind, though actual wind loads may be much larger in the microburst wind. In the outburst regions, different geometric shapes of the roof and cross-section also resulted in the different pressure distributions and overall wind loads. These differences in wind loading effects were not obvious when the models were at the center of the microburst, where high static pressure made the major contribution to wind loads. Comparison suggests that in the outburst region, the streamlined roof and circular cross-section are helpful to reduce the overall drag.

However, a small-angled or conical roof result in large suction areas and therefore experience larger uplift.

1. Introduction

A microburst is a small-size and intense downdraft that impinges on the ground resulting in a divergent outburst wind with the radial extent being less than 4.0 kilometers [1]. This damaging outburst wind can sometimes reach up to 168 mph [2] with the maximum velocity very close to the ground surface. The flow field of a developed microburst is significantly different from that of the conventional atmospheric boundary layer (ABL) wind. Statistical summarization of the meteorological studies suggests that the flow field of a microburst at its maximum-wind producing status shares many similarities with the laboratory impinging jet flow [3]. Besides the wall-jet-like outburst flow, the microburst also produces high static pressure in the core and large turbulence in the divergent outflow. Because of these unique flow features, the microburst wind could be potentially dangerous to civil structures which are normally designed to resist the conventional ABL wind.

Low-rise structures, such as houses, grain bin silos, warehouses and etc., spread widely over rural and suburban areas within the United States. Low-rise buildings are particularly more vulnerable to extreme wind loads than engineered structures. Over past few decades, many studies have been conducted to investigate wind loading effects on various types of low-rise structures, through either wind tunnel tests or full-scale field studies. A limited number of citations are referred here because their data is used here for comparison [4-6]. Due to the strong near-ground wind and unique flow

characteristics, microburst winds are supposed to have distinct wind loading effects on low-rise structures. Current building codes and standards do not provide provision for estimation of wing loads of structures in a microburst for wind loads. Therefore, a better understanding of the microburst-wind loading effects is warranted, particularly in thunderstorm-prone areas. To date, several studies have been conducted to investigate the microburst wind loads on basic cubic models. Nicholls et al. [7] studied the flow structures around a cube-shaped house model in microburst-like winds. Chay and Letchford [8] investigated the pressure distribution over a cube induced by a simulated microburst wind in a laboratory study. Sengupta and Sarkar [9] conducted an experimental study to quantify the transient loads acting on a cube with an impinging-jet-based microburst simulator. Since the total number of related research is very limited, a lot of work is still needed to quantify the microburst-induced wind loads on different structures.

In the present study, the microburst wind loading effects on a set of low-rise building models have been investigated. The microburst wind was simulated by using a steady-impinging jet in WiST (Wind Simulation and Test) lab of Department of Aerospace Engineering at Iowa State University. A steady impinging jet flow was used to simulate a steady microburst at its maximum-wind producing status, ignoring the time-domain evolution of the microburst flow field. The studied models include a cube, a conical-roofed grain bin model, and two gable-roofed building models. The purpose of this study is to establish the initial database of microburst wind loads for a few basic low-rise structures. By exploring the uniqueness and characteristics of the microburst wind

loading, the authors hope that the results of the present study may help improve the wind loading design of the low-rise structures in thunderstorm-prone areas.

2. Experimental Setup

Figure 1 shows the schematic of the steady impinging-jet flow simulator in the WiST Lab at Iowa State University, which generated the flow field for the present study. The jet flow is produced constantly by a fan on the top and impinges on a wooden ground plane to form a steady wall-jet flow field. The diameter of the nozzle (D) is about 0.6m (2 feet). The distance between the nozzle exit and the ground plane (H) was set to be 2 diameters of the nozzle (H/D=2). A honeycomb and several screens are placed at the exit of the nozzle to produce uniform velocity across the exit and reduce the turbulence of the issuing jet (approximately 2%). Velocity was measured using a Cobra probe (TFI Pvt. Ltd.), which has the ability to measure three velocity components at the same time. The velocity data was taken for 30 seconds with a frequency of 1250 Hz at each measurement point and the measurement uncertainty of the Cobra probe was within ±0.5m/s. The flow velocity at the nozzle exit of the ISU microburst simulator was set to 13 m/s (i.e., $V_{jet}\approx 13$ m/s). The corresponding Reynolds number of the flow was 5.2×10^5 based on the diameter of the jet nozzle. In Zhang et al. [10], the velocity profile generated by this simulator was compared with existing data from the field and laboratory studies and reasonable agreement was found. Therefore, this steady impinging jet has been proven to be a valid model for laboratory study.

Figure 2 presents the geometry of low-rise structural models used in the present study. All of these models were precisely fabricated using a 3D rapid prototyping machine located in the Department of Aerospace Engineering at Iowa State University. The two gable-roofed house models are the same models used for the previous study [10]. To compare the effects of different shaped roofs, the mean roof height of the grain bin model was kept the same as that of the gable-roofed models. Detailed dimensions of all models are listed in Table 1. Pressure taps were uniformly distributed over these models. These pressure taps were connected to DSA3217 pressure scanners (Digital Sensor Array, Scanivalve Corp.®) using tygon tubing (1.5mm in diameter and 0.3m long) for the surface pressure data acquisition. The pressure data were averaged over 10,000 data points collected with a frequency of 100 Hz. Since the tubing is trimmed equally short and no restrictors were included in the entire pressure acquisition system, the magnitude and phase distortion of the pressure fluctuation were insignificant [11] and hence neglected in the present study. Both the velocity and pressure measurements were taken at five radial locations within the flow field, namely r/D≈0.0, 0.5, 1.0, 1.5, and 2.0 as shown in Figure 1.

Table 1 Detailed dimension of the building models

Dimensions	**Cube**	**Grain Bin**	**Gable-roofed building 16deg.**	**Gable-roofed building 35deg.**
Mean roof height (mm)	45	36	36	36
Eave height (mm)	45	29	31	25
Total height (mm)	45	44	39	42
Roof angle (degree)	0	30	16	35
Base plan (mm)	45×45	Φ=50	65×65	65×65

3. Results and Discussions

3.1 Velocity and Turbulence Intensity

The flow field of the steady impinging jet generally has greater complexity than the conventional ABL wind. As discussed in the PIV results of the previous study [10], the velocity and turbulence showed great variations spatially within the flow field, accompanied with significant variation of the static pressure as illustrated in Figure 3. The entire picture of the microburst flow field can be depicted as follows. At the center of the microburst, a region of calm wind and high static pressure, namely the stagnation region, is formed due to the impact of the jet flow. From the center to approximately r/D≈1.0, the effects of the static pressure field gradually diminish and the flow transitions from downdraft to radial outburst flow. At r/D≥1, which is named as outburst region in the present study, the radial velocity profile resembles a wall jet and the maximum velocity decreased significantly in radial direction.

These characteristics and trends are presented in Figure 4 by using point measurements. In Figure 4, the radial velocity shown at four radial locations was normalized by the same jet velocity (V_{jet}≈13m/s) and the turbulence intensity was calculated by dividing the root-mean-square of local fluctuation by the local mean velocity. The normalized mean-roof-height of the building models and the edge length of the cube are indicated in this figure as solid and dashed lines, respectively. It can be seen that the height of low-rise building models were much lower than the height of the shear layer where velocity and turbulence intensity changed dramatically. All the building models were immersed in the high outburst wind where velocity was uniformly high and

turbulence was relatively low compared with those in the shear layer (at larger z/D). It should be noted that at r/D≈0.5, the radial velocity near the ground is much smaller ($V_r/V_{jet} \approx 0.62$) than those found in the outburst region. However, the radial velocity above z/D≈0.2 is significant, which is a direct reflection of the transitioning flow from downdraft to radial outburst. The maximum radial velocity is found to be $V_r/V_{jet} \approx 1$ at r/D≈1.0, which decreases slightly at r/D≈1.5. At r/D≈2.0, the maximum radial velocity is much smaller ($V_r/V_{jet} \approx 0.8$) due to the turbulence mixing and dissipation. In general, the maximum radial velocity occurs at the mean-roof-height or lower of the model tested. The local turbulence intensity near the ground was found to increase monotonically from approximately 10% to 25% as the radial location changed from r/D≈0.5 to 2.0. The maximum local turbulence intensity (normalized by the mean local radial velocity) occurred at r/D≈2.0. However, the maximum turbulence intensity at the mean-roof-height or lower, if normalized by the same velocity value, occurred at r/D≈1.5 since the radial velocity decreased significantly at r/D≈2.0.

3.2 Mean and RMS Pressure Coefficients as a Function of Radial Locations

The mean pressure distribution on the building surfaces depend on the radial location of the building in the microburst flow field. The overall trend was found to be similar for all the low-rise building models and therefore only the contours for the grain bin models are shown in the present paper. In Figure 5, the expanded view of mean pressure distribution is shown at different radial locations. The pressure coefficients were calculated using the velocity at the jet exit ($V_{jet} \approx 13 m/s$). It can be seen that at the center of the microburst, the pressure coefficient is uniformly almost 1.0 all around the

grain bin model due to the local high static pressure in the stagnation region. At r/D≈0.5, though the surface pressure on the leeward side is reduced by half due to the flow-structure interaction, the entire surface experiences positive pressure. It indicates that the structure would experience considerable positive external pressure when the microburst occurs near the structure. This situation would be potentially dangerous for structures like grain bin silos, which are normally sealed for storage purpose. At r/D≥1.0, the pressure distributions were not significantly different from those found in the ABL wind [5-6]. Related to change of the local wind speed and turbulence intensity, the magnitude of the positive pressure on the windward side of the wall and the negative pressure on roof and the side of the wall was found to decrease as r/D increased from 1.0 to 2.0.

Figure 6 shows the root-mean-square of the fluctuating pressure coefficients at different radial locations. Generally, the pressure fluctuation is small when the grain bin model is at or near the center of the microburst, i.e. r/D≈0.0 and 0.5. At r/D≥1.0, high pressure fluctuations are found on the windward sides of the roof and side wall. The pressure fluctuation reaches the maximum when the model is at r/D≈1.5. At r/D≈2.0, the pressure fluctuation decreases slightly but is still larger than that found at r/D≈1.0. The result implies that the fluctuating surface pressure is directly linked to the fluctuation of wind speed at these radial locations. At r/D≈2.0, although the local turbulence intensity is higher than that at r/D≈1.5, the root-mean-square of the fluctuating velocity was actually smaller due to the decrease of mean velocity.

3.3 Comparison of Wind Loads on Different Structures

Low-rise building is a large category of civil structures and usually designed with various geometric shapes for different functions. Different geometric shapes trigger different types of flow-structure interaction and therefore require different standards for minimum wind load design. In microbursts, the geometric shape of the low-rise building will play an even more important role since the near-ground wind and turbulence are more significant than the conventional situation of the ABL wind. In this study, the four building models covered several key factors for low-rise building design, including different roofs (flat, conical, and gable) and cross-sections (square and circle).

Figure 7 presents the comparison of the mean pressure distribution of different building models when they are at r/D≈1.0, where the maximum radial velocity is found. First, it can be seen that the pressure distribution over building roofs varies considerably among different building models. For sharp-corner structures, such as the cube and the 16 degree gable-roofed model, high suction (minimum negative pressure) is observed at the windward edges due to the local separation bubble caused by flow separation. For the conical roof of the grain bin model, a small positive pressure region is observed on the windward side along the centerline, which implies that no severe separation occurred at the leading edge even with the larger roof angle (30 degree). However, a large negative pressure region is seen starting from approximately 45 degree with respect to the wind direction as shown in Figure 7 (b). The negative pressure region apparently covered larger portion of the roof than other models, indicating that the conical roof may suffer more uplift force. Compared with 16 degree gable-roofed building, no negative

pressure is seen at the windward edge of the 35-degree building. Pressure on the leeward side of the building is negative but distributed more uniformly implying the flow had completely separated over the roof ridge. Meanwhile, the circular cross-section of the grain bin model resulted in a different distribution on the wall. It can be seen that the area covered by high positive pressure on the wall is significantly reduced by the curvature of the grain bin model. The area covered by low negative pressure is also reduced on left and right sides of the circular wall compared with the other three models.

Figure 8 shows the root-mean-square of pressure coefficient fluctuation of the four building models at r/D≈1.5, where the maximum turbulence intensity occurred. Generally, the high RMS pressure region corresponded to those where large suction occurred as shown in Figure 7. It is interesting to note that the pressure fluctuation on the roof of the cube is much smaller than that on the sidewalls in Figure 8 (a). This may be related to the decrease of velocity over the height of the cube as shown in Figure 4 (c). The 35-degree gable-roofed building model experienced the smallest pressure fluctuation on the roof, while the 16-degree gable-roofed building and grain bin models experienced large RMS pressure coefficients up to approximately 0.6 on the windward roof. The pressure fluctuations on the sidewalls of all models are observed to be significant. Although the circular cross-section reduced the magnitude of the negative pressure on the sidewall of the grain bin model, the pressure fluctuation on both sides is still considerable. The maximum pressure fluctuation on the windward wall, which depends only on the oncoming flow turbulence, is found to be similar for all the four models.

3.4 Comparison with Previous Studies

The pressure coefficients along the centerline of the cube were extracted and compared in Figure 9. In Figure 9 (a), the distribution was compared within the present study and the pressure coefficient was calculated using the jet velocity as the reference velocity. Pressure distributions at r/D≈0.0 and 0.5 were completely different from those found in the outburst region, i.e. r/D≈1.0-2.0. At or near the center of the microburst, the local static pressure contributed to the positive external pressure over the building surface. In the outburst region (r/D≥1.0), the pressure coefficient distribution is found to be similar to those obtained in ABL wind. In Figure 9 (b), the pressure coefficient at r/D≈1.0 was compared with those found in the previous studies, including different types of wind, i.e. microburst, ABL, and uniform winds. To validate this comparison, pressure coefficients were calculated using the eave height velocity, i.e. $C_p = (P - P_{atm})/0.5\rho U_{eave}^2$. Generally, it is found that the pressure on the windward wall induced by a microburst wind is higher than those expected in ABL wind because of the wall-jet-like wind profile. Among the results of microburst wind studies, a very good agreement is found between the present study and the previous studies of Chay and Letchford [8] and Sengupta [12]. It should be noted that the jet diameter (D) and model size (B) used in these studies were not the same, which were D=0.51m/B=30mm and D=0.20m/B=12.7mm, respectively. This difference of scale and blockage ratio could be responsible for the slight differences found in this comparison. Meanwhile, it was also suggested by Castro and Robins [4] that the pressure distribution over the roof and leeward wall was also closely related to the local turbulence intensity.

Available pressure data for the grain bin model was relatively scarce. The circumferential pressure distribution around the wall of grain bin silos at a height of 2/3 to 5/6 eaves height were documented in Cook and Redfearn [5] and MacDonald et al. [6], by taking full scale and wind tunnel measurements respectively. The pressure data at r/D≈1.5, where maximum pressure fluctuation occurred, was extracted to compare with the data from the above studies in Figure 10. The pressure was normalized again by the wind speed at eaves height of each model. As suggested by McDonald et al. [6], a factor of 1.35 was applied to the data of Cook and Redfearn [5] since the pressure coefficient was calculated using wind speed at 10m as the reference velocity. It can be seen that both the mean and RMS pressure coefficients followed the trends of the previous studies, particularly for the full scale ABL wind study. The minimum mean pressure in the present study is found to be smaller, while the maximum RMS of pressure fluctuation is larger compared to the other studies. This discrepancy may result from the greater turbulence intensity in the present study, which was 22%~25% at r/D≈1.5, compared with that found in MacDonald et al.[6] (around 15%~20%) and Cook and Redfearn [5] (not clear).

The comparison of the pressure distribution on the gable-roofed building models was included in Zhang et al. [10], and will not be discussed here. In conclusion, the mean and fluctuating pressure acting on the low-rise buildings in a microburst behaves quite differently from that in the normal ABL wind. At or near the center of the microburst, high static pressure plays an important role for the external pressure over the low-rise buildings. In the outburst region, the pressure distribution on the low-rise buildings is

generally similar to that in the conventional ABL wind, though minor difference was still observed. These differences, including higher pressure on the windward wall and larger pressure fluctuations on the sidewalls, may result from the unique characteristics of the outburst flow, such as the wall-jet-shape wind profile and high turbulence intensity. It also should be noted that the actual pressure loadings on the buildings could be much higher than the standard design for ABL winds, as the pressure coefficients were calculated using different reference velocity.

3.5 Comparison of Overall Mean Wind Loads

The overall mean wind loads were calculated by integrating the pressure over the entire surface of building models. The mean radial and vertical force coefficients were then normalized by using the jet velocity and corresponding projection area as references. As shown in Figure 11, both radial (drag) and vertical (uplift) direction force coefficients changed significantly as a function of building geometry and radial location. For all building models, the force coefficients changed in a similar fashion as the radial location changed. At or near the center of the microburst, radial direction force acting on the low-rise buildings was almost zero or relatively small. However, the downward pushing force acting on the building roof was much more significant. This unique situation induced by downdraft flow is usually not considered in the current design standards and therefore potentially dangerous for the safety of structures, particularly for a sealed structure. In the outburst region, i.e. $r/D \geq 1.0$, drag coefficient became more significant and vertical force coefficient became positive indicating uplift force on the

building roofs. The maximum drag and uplift for all models could be expected at r/D≈1.0, where the maximum velocity was seen within the microburst flow field.

Building geometry also plays an important role in determining the overall mean wind loads. In Figure 11, it can be seen that the difference among all tested models was not significant when they are at or near the center of the microburst. It implies again that the high static pressure, instead of the flow-structure interaction, has a greater contribution to the overall wind loads in these areas. In the outburst region, i.e. r/D≥1.0, the drag coefficient of the cube was the largest among all building models due to the large positive pressure on the windward wall (Figure 7). The 35 degree gable-roofed building model suffered a larger drag than its 16 degree counterpart due to the blockage effect of the steeper roof. However, it is interesting to note that even though the roof angle of the grain bin model was not the smallest (30 degree), it actually suffered the smallest drag among all the building models due to the circular cross-section, which corresponds well with the observation of the pressure distribution. Nevertheless, it can be seen, in Figure 11 (b), the uplift force coefficient acting on the conical roof of the grain bin was the largest, corresponding well with the large portion of suction area on the conical roof observed in Figure 7 (b). The 16 degree gable-roofed building and the cube also suffered large uplift in the outburst region due to the large suction area at the windward corner. The uplift force coefficient for the 35 degree gable-roofed building model was much smaller than those of other models corresponding well with the pressure distribution in Figure 7.

4. Conclusions

A laboratory study was conducted to investigate the microburst-wind loading effects on low-rise buildings with various geometric shapes, including a cube, a grain bin model, and two gable-roofed building models. A steady impinging jet flow was employed generated by a microburst simulator located at Iowa State University. Velocity and turbulence intensity profiles were measured to reveal the complicated flow characteristics within the microburst-like wind. These flow field characteristics were then combined with the surface pressure measurements to show the microburst-wind loading effects on different building models, when they were mounted at different radial locations. Both the mean pressure and root-mean-square of the fluctuating pressure coefficients were studied and compared with those of the previous studies. Finally, the overall mean wind loads for all building models were summarized by integrating the surface pressure. The effects of different geometric shapes on the microburst-wind loading were summarized.

In conclusion, microburst-wind loading effects were more complicated than that was normally expected in normal ABL winds due to the complex flow regime. It is suggested that low-rise buildings would suffer high external pressure and large downward force if a microburst occurs near the location of building, such as $r/D \approx 0.0$ and 0.5 in the present study. In the outburst region, the distribution of pressure coefficients was basically similar to those obtained in ABL wind. However, some differences, such as higher mean pressure on the windward wall and higher pressure fluctuation on the sidewalls, are observed because of the wall-jet-like profile and high turbulence intensity of the outburst

flow. Generally, the maximum mean pressure was found at r/D≈1.0 and the maximum pressure fluctuation was found at r/D≈1.5. Since the microburst winds are usually more violent than normal ABL winds, the magnitude of the actual pressure and force would be expected to be much more significant.

Geometric shape of the low-rise building also plays a key role, when the building models were in the outburst region. Pressure distributions suggested that flat, low-angle, and conical roof resulted in large suction areas and large pressure fluctuations on the roof due to the flow separation and reattachment. The circular cross-section of the grain bin model significantly reduced the area of high positive pressure on the windward side and negative pressure on the sidewall. Comparison of the overall mean wind loads revealed that the streamlined roof and circular cross-section helped reduce the drag when they were in the outburst region. However, a small-angle roof or conical roof also resulted in large uplift force on the roof.

The goal of the present study is to establish a general understanding on microburst-wind loading effects on different low-rise structures. In future studies, it is suggested that entire life-cycle of the microburst flow field should be considered to resolve the time-domain variations of the microburst wind loading effects. A larger scale microburst simulator is also suggested to obtain better resolution of pressure measurement, particularly at regions with most research interests.

References

[1] Fujita T. T., 1985. The Downburst: Microburst and Macroburst. University of Chicago Press, Chicago

[2] National Weather Service, http://www.erh.noaa.gov/cae/svrwx/downburst.htm

[3] Hjelmfelt M.R., 1988. Structure and life cycle of microburst outflows observed in Colorado. J. Appl. Meteorol. 27(8), 900-927.

[4] Castro I.P., Robins A.G., 1977. The flow around a surface-mounted cube in uniform and turbulent streams. J. Fluid Mech. 79 (2), 307–335.

[5] Cook N.J., Redfearn, D., 1980. Full scale wind pressure measurements on cylindrical silos: a preliminary report, Dep. Environment Note No. N103/80, Building Research Establishment, September 1980.

[6] MacDonald P.A., Kwok K.C.S., Holmes J.D., 1988. Wind loads on circular storage bins, silos and tanks: I. Point pressure measurements on isolated structures. J. Wind. Eng. Ind. Aerodyn. 31, 165–188.

[7] Nicholls M., Pielke R., Meroney R., 1993. Large eddy simulation of microburst winds flowing around a building. J. Wind Eng. Ind. Aerodyn. 46, 229-237.

[8] Chay M.T., Letchford C.W., 2002. Pressure distributions on a cube in a simulated thunderstorm downburst, Part A: stationary downburst observations. J. Wind Eng. Ind. Aerodyn. 90, 711-732.

[9] Sengupta A., Sarkar P.P., 2008. Experimental measurement and numerical simulation of an impinging jet with application to thunderstorm microburst winds. J. Wind Eng. Ind. Aerodyn. 96, 345-365.

[10] Zhang Y., Sarkar P.P., Hu H., 2012. An Experimental Study of Microburst-wind Loads on Gable-roofed Houses, AIAA-2012-2831, 30th AIAA Applied Aerodynamics Conference, New Orleans, Louisiana, 25-28 June, 2012.

[11] Irwin H.P.A.H., Cooper K.R., Girard R., 1979. Correction of distortion effects caused by tubing systems in measurements of fluctuating pressures. Journal of Industrial Aerodynamics, 5, 93-107.

[12] Sengupta A., 2007. Study of microburst-induced wind flow and its effects on cube-shaped buildings using numerical and experimental simulations of an impinging jet. Ph.D. dissertation, Iowa State University.

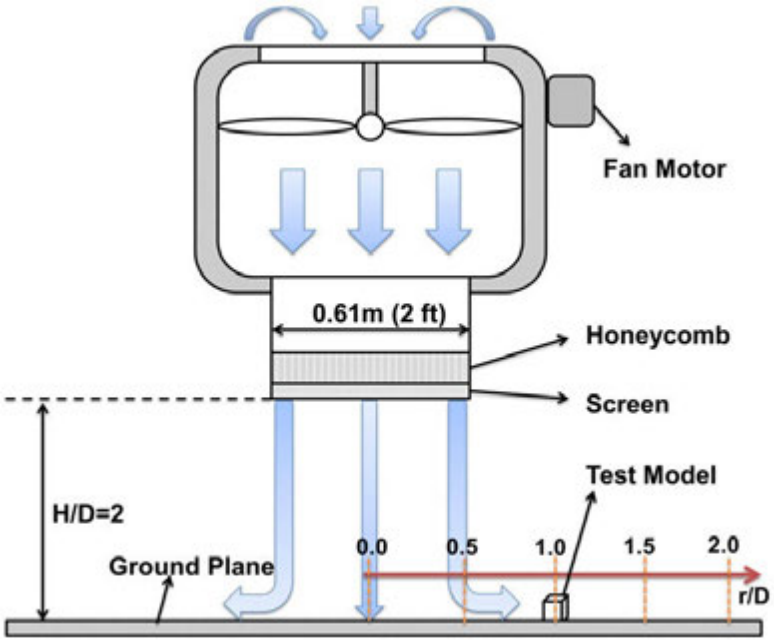

Figure 1. *Schematic of microburst simulator*

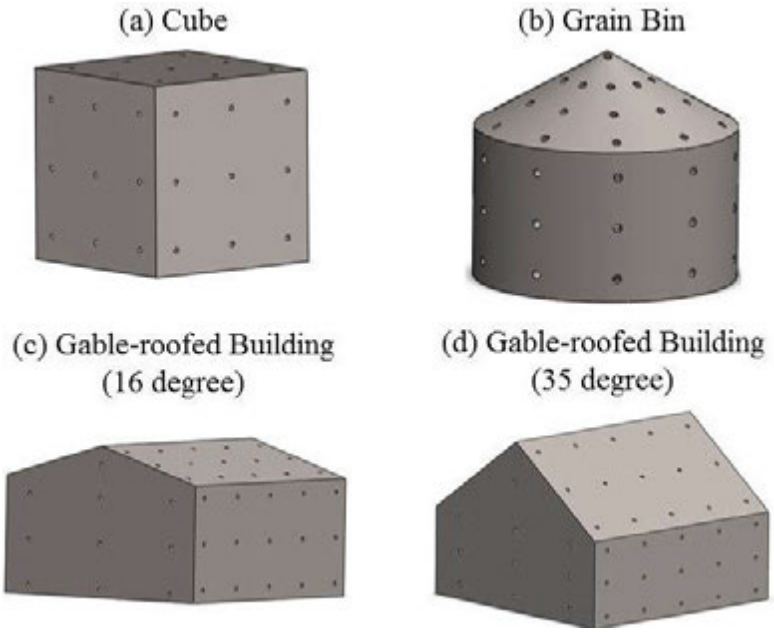

Figure 2. *Geometry of the building models*

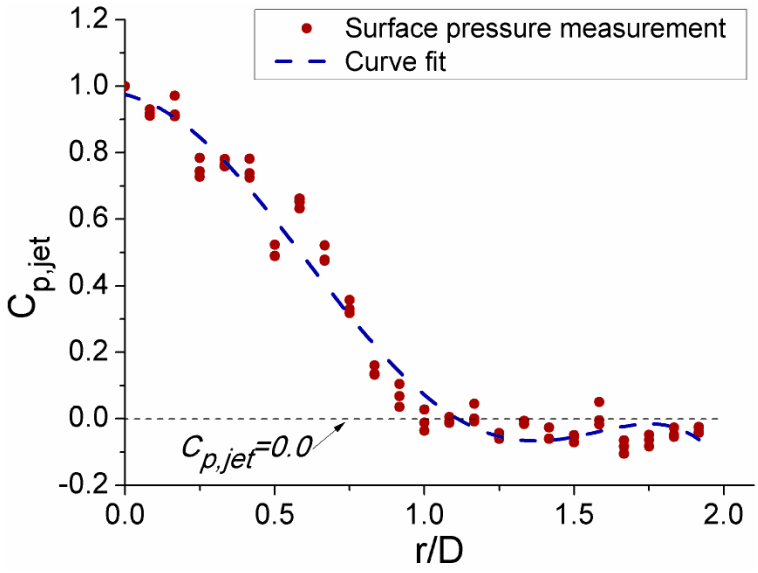

Figure 3. *Distribution of surface pressure coefficient*

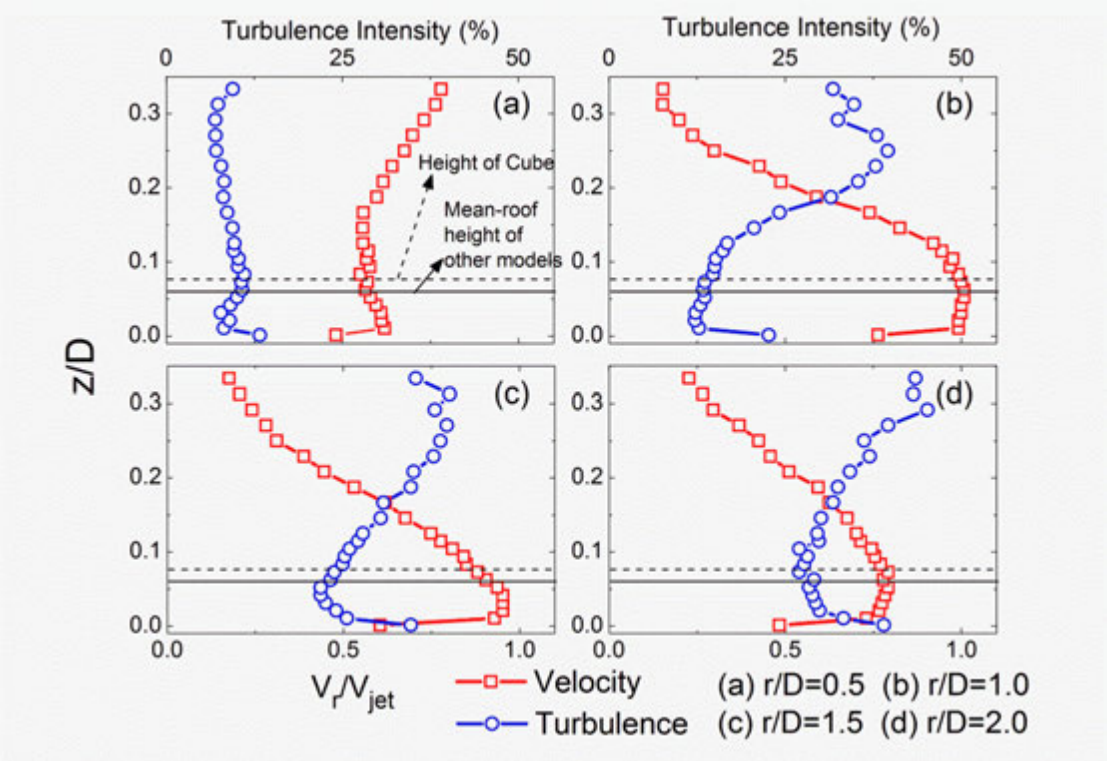

Figure 4. *Normalized radial velocity and longitudinal turbulence intensity profiles at different radial locations*

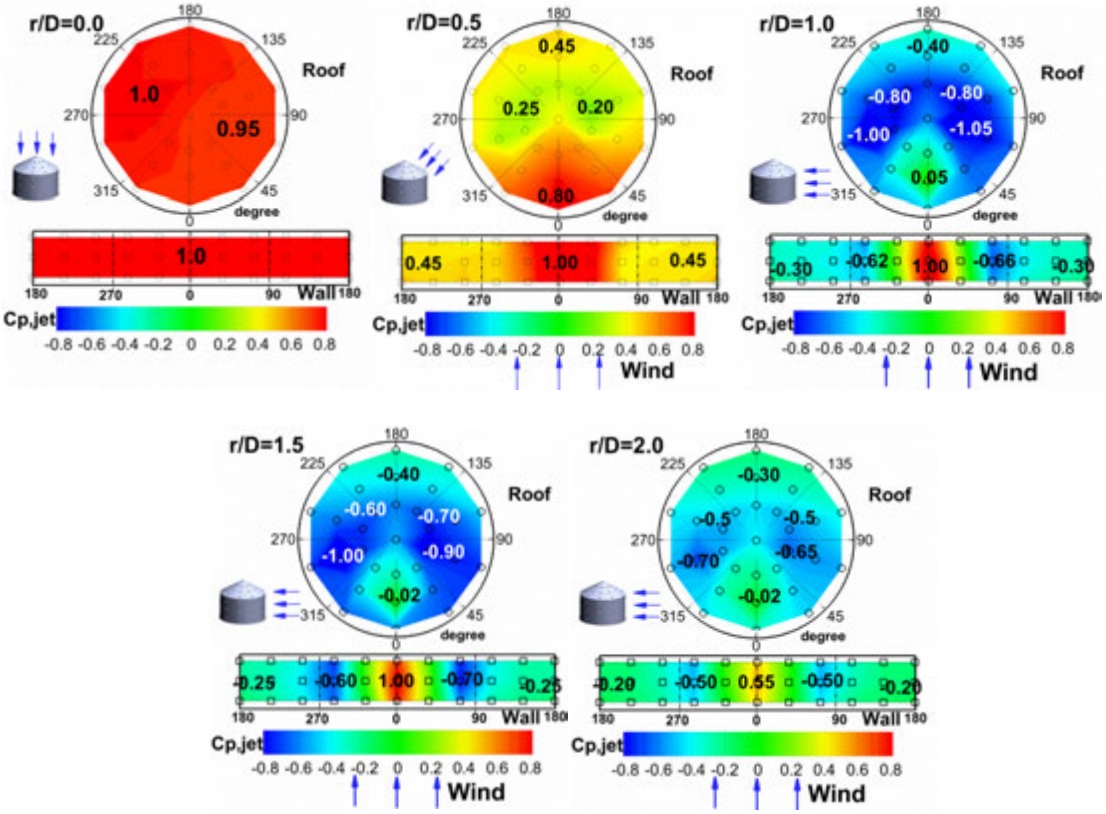

Figure 5. *Mean pressure coefficients over the grain bin model*

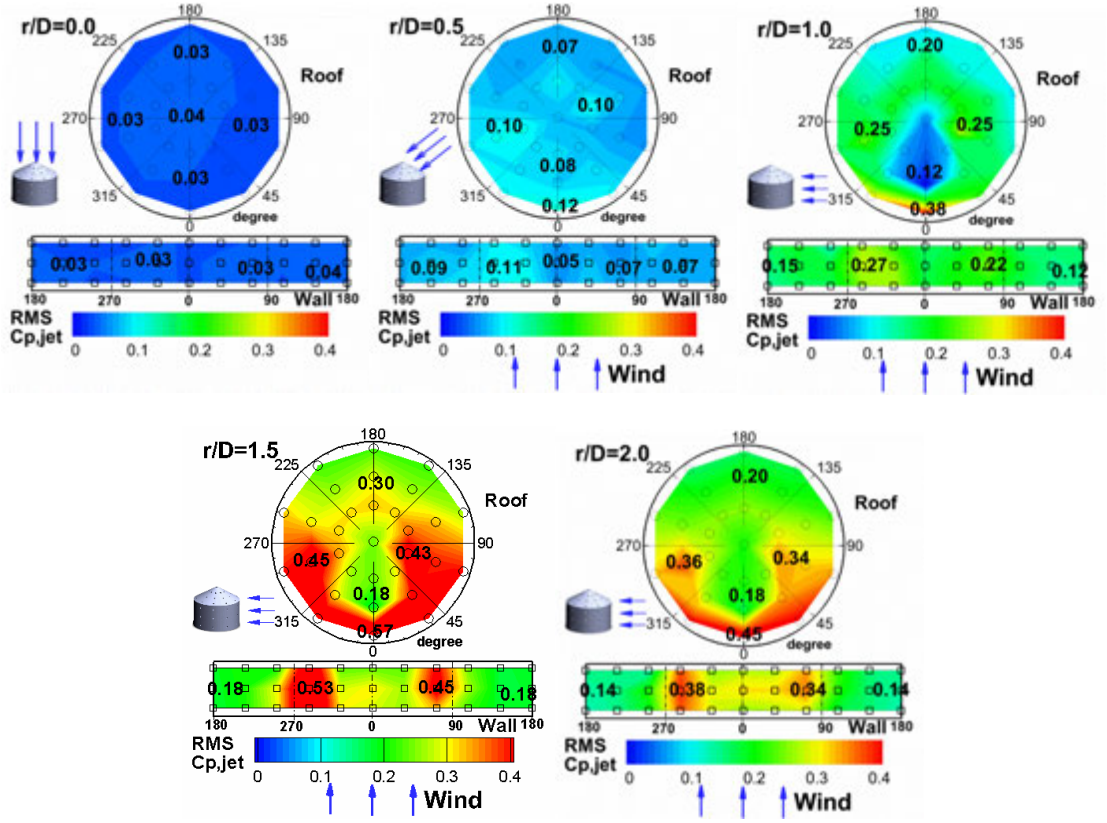

Figure 6. *Root-mean-square of fluctuating pressure coefficients over the grain bin model*

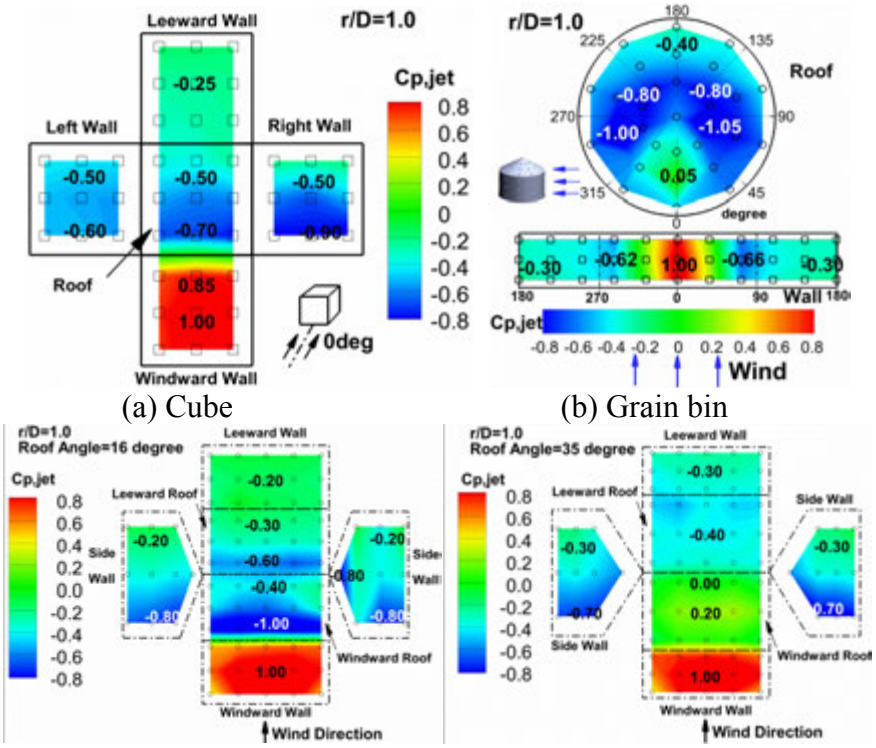

(a) Cube (b) Grain bin

(c) Gable-roofed 16 degree (d) Gable-roofed 35 degree

Figure 7. *Comparison of mean pressure coefficient at r/D≈1.0*

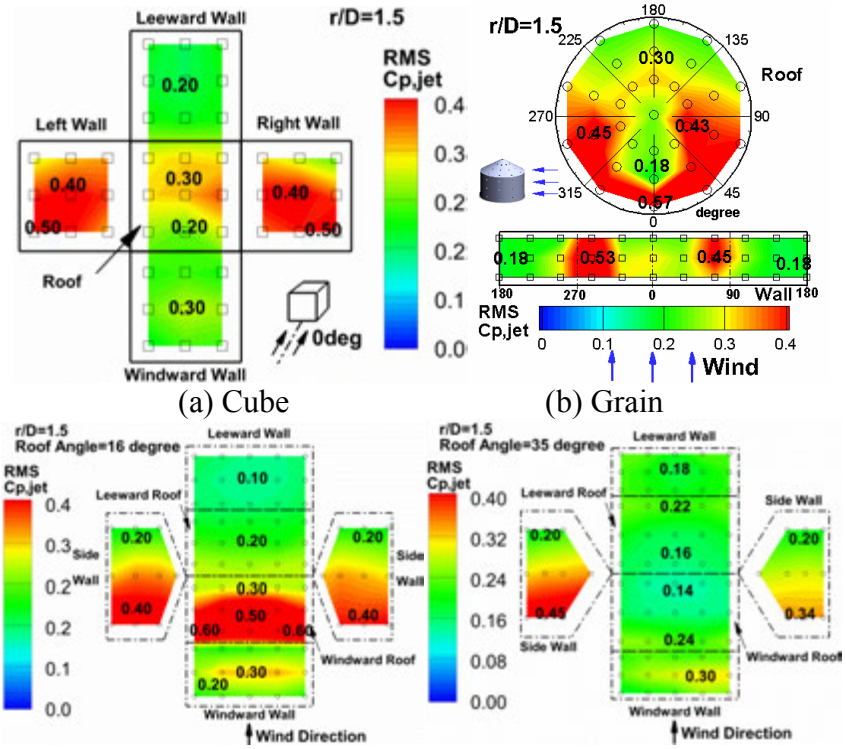

(a) Cube (b) Grain

(c) Gable-roofed 16 degree (d) Gable-roofed 35 degree

Figure 8. *Comparison of RMS pressure coefficient at r/D≈1.5*

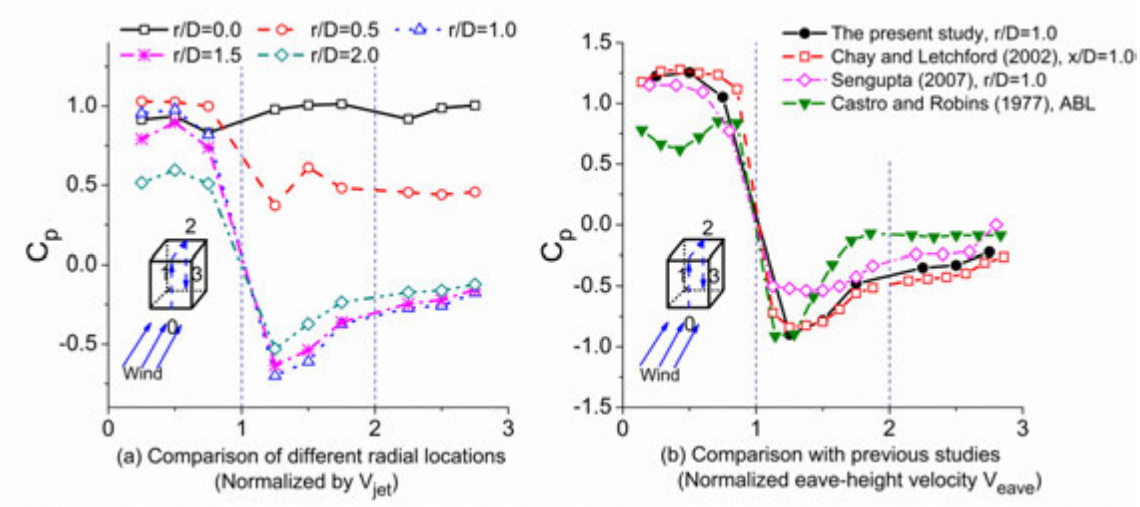

Figure 9. *Comparison of mean pressure coefficient along the centerline of the cube*

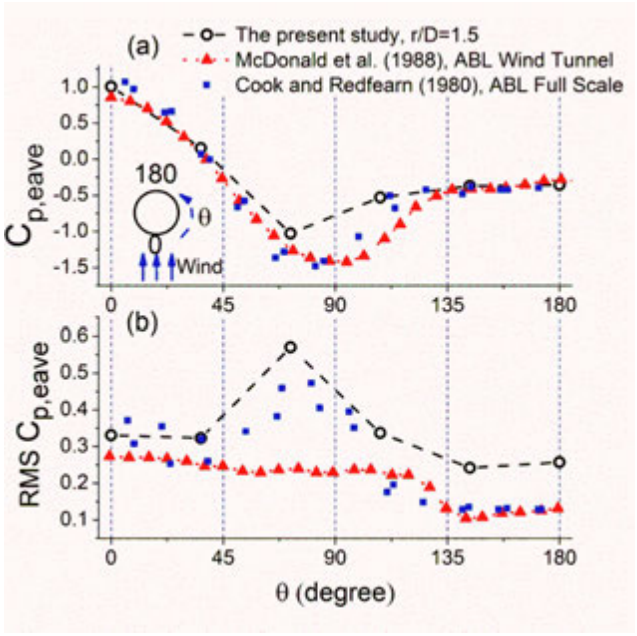

Figure 10. *Comparison of mean and RMS pressure coefficient along circumferences of the grain bin model (Reference velocity V_{eave})*

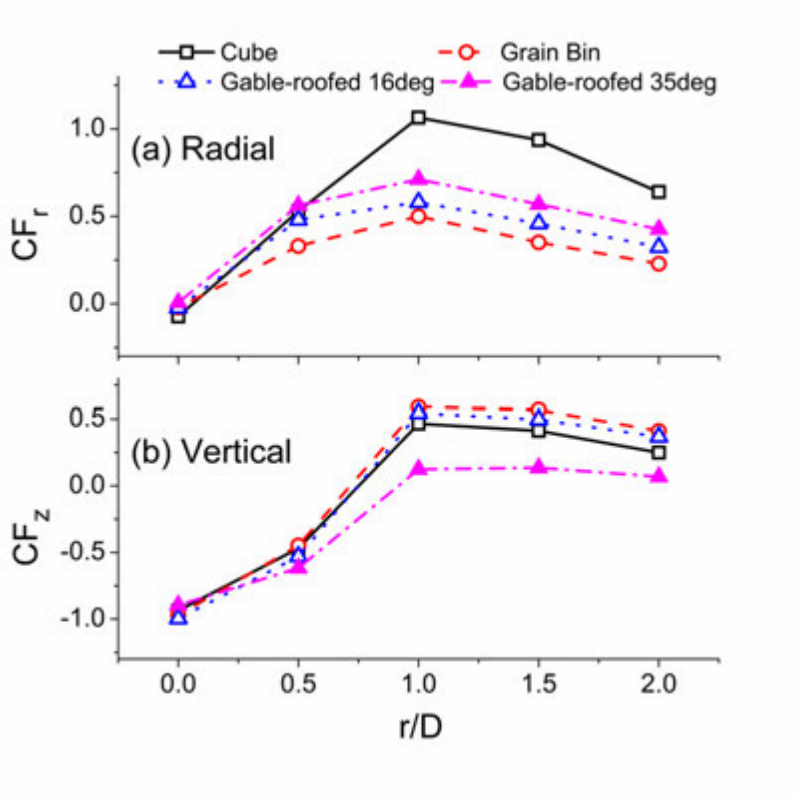

Figure 11. *Comparison of overall mean wind loads*

CHAPTER 5

A LABORATORY STUDY OF MICROBURST-WIND LOADING EFFECTS ON A HIGH-RISE BUILDING MODEL

Yan Zhang, Partha P. Sarkar, Hui Hu

Department of Aerospace Engineering, Iowa State University, Ames, Iowa, 50010

Abstract: Microbursts have unique flow characteristics and may result in distinct wind loading effects on high-rise buildings, compared to the normal atmospheric boundary layer (ABL) wind. A laboratory study has been conducted to investigate the mean and dynamic features of microburst-wind loads on a high-rise building model. The microburst was simulated using an impinging-jet-based microburst simulator. First, velocity and turbulence intensity profiles were measured to study the flow field characteristics. The mean and dynamic wind loads induced by the simulated microburst were then studied in detail by taking both pressure and force measurements. Results suggest that the characteristics of wind loads acting on the high-rise building model are dramatically different from those obtained in the ABL wind. Both the mean and dynamic wind loads were found to depend on the radial location and the orientation of the high-rise building within a microburst flow field. Power spectrum densities of the velocity and force coefficient fluctuations were also calculated which revealed different frequency components of the dynamic wind loads. It was found that the along-wind and across-wind force fluctuations were better correlated in the outburst wind than those in the ABL wind. Evidence suggested that the dynamic wind loads were influenced by the low-frequency movement of primary vortices and the high turbulence in the outburst

region. In general, the wind loading effect on a high-rise building is found to be more complex and dynamics than its counterpart ABL wind. Results presented here may be helpful for the design of high-rise building in the thunderstorm-prone areas.

1. Introduction

High-rise buildings are commonly designed to resist extreme wind conditions with long return periods. Although catastrophic structural failure induced by wind is almost unlikely to occur, research regarding detailed wind loading effects on high-rise buildings is still more than necessary from serviceability and economic point of view. Figure 1 shows the damages of two tall buildings during Hurricane Alicia in 1982 and Hurricane Wilma in 2003 [1]. Broken glass could be seen around the building possibly due to either the external pressure fluctuations or wind-borne debris during the hurricane. To better understand the mechanisms of wind-induced static and dynamic loads and reduce the risk of damage, wind tunnel test has been carried out by many researchers and proven to be an effective tool for the study of wind loads on high-rise buildings. For example, Melbourne [2] compared the results of pressure distributions and responses on the Commonwealth Advisory Aeronautical Research Council Coordinators (CAARC) standard rectangular tall building model [3] from six establishments and obtained quite good consistency among research groups. Following this research, Tanaka and Lawen [4] studied the same building model with a different scale (1:1000) and concluded that almost no deficit could be found due to the exaggerated small length scale. Lin et al. [5] conducted extensive experiments to study the local wind loads on nine building models with different rectangular cross-sections and revealed different parametric effects on

wind loading. These studies provided a solid database for comparison in the present study. Besides, fruitful research accomplishments have been achieved over past few decades covering a wide variety of interesting topics, such as across-wind response of tall building [6-9], mitigation of across-wind response by aerodynamic modifications [10-12], interference effects on wind loads among multiple tall buildings [13-16], etc. While most of the previous field or wind tunnel studies were performed by applying atmospheric boundary layer (ABL) wind, a great amount of wind hazard, however, could be contributed by other non-standard winds. Chen and Letchford [17] evaluated and compared the maximum dynamic magnification factor (MDMF) of the CAARC building model induced by standard wind profile and conceptual generic downburst wind profiles. Sengupta et al. [18] performed laboratory test to study the transient loads of a cubic building in a translating tornado and microburst flow field. Both tornado and microburst loads were found to exceed the design standard of ASCE 7-05. Yang et al. [19] studied the flow structures around a high-rise building model and the wind loads in a tornado-like wind. Nevertheless, related research is still scarce and "the impact of these 'non-standard' wind profiles on tall buildings needs further research" [20].

Extreme wind can be produced either by a tropical cyclonic system, such as typhoon and hurricane or by a localized severe weather condition, such as thunderstorm and tornado. Compared with the tropical storms, local wind storms are usually more devastating to the affected area and difficult to predict due to the small length scale and short lifespan. Downburst is one kind of such local storms hidden within a thunderstorm, whose flow regime is analogous to a "reversed tornado". As a tornado causes a low-

pressure core and sucks air inwards and upwards, a downburst, originated from an intense downdraft of air, usually produces radial outburst winds due to the high pressure in the core. Specifically, Fujita [21] defined that a microburst is a MISO-scale downburst which extends less than 4 kilometers radially. It could cause damaging outburst wind speed as high as 168 mph [22]. Basically, the flow field can be divided into three regions according to different flow regimes as demonstrated in Figure 2, i.e. downdraft region, stagnation region, and outburst region. The microburst wind usually has many unique characteristics:

1. High static pressure in the stagnation region. This is often referred as “pressure nose” which is opposite to the pressure drop in the tornado core.
2. Jet-like flow in outburst region. The maximum wind speed could be expected very close to the ground and the velocity profile no longer follows the log law of the ABL wind.
3. Large turbulence and wind shear. Due to the strong shear at the jet-ambient interface, turbulence level in the outburst flow could be much higher than that of the ABL wind.

The relative scale of a low-rise and high-rise building was also schematically compared with the outburst profile in Figure 2. Since the height of a tall building is normally higher than the depth of outburst velocity flow in most cases, the wind loading effects might be influenced by all the wind characteristics listed above. Therefore, even though the microburst wind is often more catastrophic for a low-rise building due to the near-ground extreme wind, the wind loads acting on a high-rise building could be more

complicated. In this paper, laboratory experiments were carried out to study the steady and dynamic wind loads acting on a high-rise building model with a square plan in a simulated microburst flow field. Both pressure and force measurements were performed to quantify the wind loading effects. Results were also compared with those of previous wind tunnel tests to emphasize the uniqueness of microburst wind loads which has not been covered by the existing building design standard.

2. Experimental Setup

The experimental study was conducted by using an impinging-jet-based microburst simulator located in the Department of Aerospace Engineering at Iowa State University (ISU). As shown in Figure 3, a downdraft flow is generated through an axial fan driven by a step motor. The exhaust nozzle diameter of ISU microburst simulator is 610 mm (D). A geometric scale of approximately 1:650 was reached if comparing this diameter to a small-size microburst with 400m diameter. The distance between the nozzle exit and the ground plane (H_{jet}) was set to be 2 times of the jet diameter ($H_{jet}/D=2$), which falls into a reasonable range of microburst in nature ($H_{jet}/D=0.75\text{-}7.5$). Honeycomb and screen structures were placed upstream of the nozzle exit in order to produce a uniform jet flow exhausted from ISU microburst simulator. During the experiments, a three-component cobra-probe (Turbulent Flow Instrumentation Pvt. Ltd.), which is capable of simultaneously measuring all three components of the flow velocity vector, was used to quantify the flow characteristics of the jet flow at the points of interest. The velocity data were recorded for 30 seconds with a sampling frequency of 1250 Hz at each measurement point. The measurement uncertainty of the cobra-probe was within

±0.5m/s. It was found that the jet flow exhausted from ISU microburst simulator was quite uniform across the nozzle exit, and the turbulence level of the core jet flow was found to be within 2.0%. The flow velocity at the nozzle exit of the ISU microburst simulator was set to 13 m/s (V_{jet}), and the corresponding Reynolds number of the microburst-like wind is 5.2×10^5 based on the nozzle diameter of the ISU microburst simulator. Further information about the design, construction, and performance of ISU microburst simulator as well as the quantitative comparisons of the microburst-like wind generated by using ISU microburst simulator with the microbursts occurring in nature can be found at Zhang et al. [23].

The tested high-rise building model, also shown in Figure 3, has a 45mm×45mm (B×B) square cross-section and a total height of 180mm (H=4B). According to the 1:650 scale ratio of the microburst flow field, the test model used in the present study represents a high-rise building with a 29m×29m square cross section and a 117m total height. The building height fits well with the extent of the flow field generated by the microburst simulator as can be seen later. During the entire experiment, steady wind loads on the model were measured at five radial locations with respect to the microburst center, namely r/D=0.0, 0.5, 1.0, 1.5, and 2.0. To measure the pressure distribution over the model surface, 30 pressure taps were distributed in a 3×10 grid-pattern on each of four side walls and 9 were distributed in 3×3 grid-pattern on the roof of the building model. These pressure taps were connected to DSA3217 pressure scanners (Digital Sensor Array, Scanivalve Corp.®) using tygon tubing (1.5mm in diameter and 0.3m long) for the surface pressure data acquisition. The pressure data were averaged over

10,000 data points collected with a frequency of 100 Hz. Since all tubing lengths were equal but short and without any restrictors, the magnitude and phase distortion of the pressure fluctuation were insignificant [24] and hence neglected in the present study. Resultant wind loads were also measured using a high-sensitivity force-moment sensor (JR3, model 30E12A-I40). The JR3 load cell is capable of measuring forces in three directions and the moment (torque) about each axis. For each test run, 15,000 data points were taken with a sampling frequency of 1,000 Hz. The measurement uncertainty of the sensor is ±0.25% of the full range (40 N).

3. Flow Field Characteristics

Based on statistical summarization of a series of field studies, Hjelmfelt [25] suggested that the microburst flow field at its maximum velocity producing phase (status) resembles a well-developed impinging jet flow. This similarity was later proven by many researchers who successfully used the impinging jet model to produce outburst wind profiles similar to the field data. Moreover, the maximum status of a microburst represented by the steady impinging jet is also the most critical situation for the study of wind loading effects. Therefore, even though the steady impinging jet is significantly simplified model of a microburst, which is a complicated natural phenomenon, it is still a faithful and popular modeling method for wind engineering studies.

The flow field of steady impinging jet used in the present study was comprehensively studied by conducting both point and PIV measurements and verified by comparing results with field study data. The detailed discussions were documented in Zhang et al. [23]. To give a clear visual illustration of the whole flow field and its

relative dimension compared with the test model, the normalized average wind speed contour of the steady impinging jet flow obtained in the previous study combined with the high-rise building model are shown in Figure 4 schematically. The overall wind speed ($|V| = \sqrt{V_r^2 + V_z^2}$, where V_r is the radial velocity component and V_z is the axial/vertical velocity component) was non-dimensionalized by the mean jet velocity V_{jet}. It can be observed that the average wind speed distribution has a large variation spatially. Because of the stagnated flow, the wind speed is calm within the core. The high core pressure and the continuous impinging jet then force the airflow to accelerate in the radial direction and forms a high wind speed region around r/D≈1.0. Finally, the wind speed decays as the air flow moves further away from the center. The wind speed also varies significantly in the vertical direction. As shown schematically in Figure 4, the wind speed increases and then decreases from the ground plane to the roof height (white dashed line, z/D≈0.3) of the building model in the outburst region. Different from a low-rise building whose height is typically lower than the height of maximum wind speed, the high-rise building covers a much wider range vertically and hence may experience more complicated wind loading effects.

Figure 5 shows the velocity and turbulence intensity profiles measured by the cobra-probe, at the center (r/D=0) and four radial locations (r/D=0.5, 1, 1.5, and 2.0). At the center of the simulated microburst, the axial velocity V_z starts to decrease from $V_z/V_{jet} = 1$ around z/H≈3.4 (≈0.5H_{jet}), i.e. 3.4 times of the building height. It should be noted that this deceleration towards the ground plane gives rise to the high pressure dome around the stagnation region. Therefore, the high-rise building could be completely

immersed in the high pressure dome when it is located at the center of the microburst. The turbulence level at the center is around 2% which is much less than that of the outburst region. At r/D=0.5, the radial velocity increases as the distance from the ground increases, which differs from the profiles at other radial locations. It also should be noted that the downdraft velocity component (negative V_z) is still significant at this point since the flow was transitioning from the downdraft to the radial outburst flow. The turbulence intensity was found to be greater than that at the center, but still smaller than those at further radial locations. At r/D=1.0, 1.5, and 2.0, radial velocity profiles shows similar wall-jet shapes with maximum velocity occurring below half of the building height. The maximum radial velocity decreases as r/D increases. Meanwhile, the vertical velocity component V_z is negligible compared with that at the center and r/D$\approx$0.5. Turbulence was found to be much larger in the outburst region (>10%) compared with the core region. Due to the strong instability in the shear layer, turbulence intensity was found to increase sharply as the vertical distance from z/H=0.5 to the roof height of the building model (indicated by the black dashed lined) at these radial locations. This substantial variation of turbulence level over the building height may add more complexity to the wind loads acting on the building.

4. Mean Wind Loads

4.1 Mean Pressure Distribution

As aforementioned, the steady impinging jet can be seen as a model to describe a microburst flow field at maximum strength. Therefore, studying the mean wind loads

induced by the steady impinging jet, akin to evaluating the "worst-case scenario" when a microburst occurs at different distances from the high-rise building, is of great importance for guiding building design.

Figure 6 presents the distributions of mean pressure coefficients around the building surface, when the high-rise building model was mounted at five different radial locations. The pressure coefficient was calculated using the jet velocity, i.e. $C_p = (\mathrm{P} - P_{atm})/0.5\rho V_{jet}^2$, because the $\mathrm{V_{max}}$ is almost equal to $\mathrm{V_{jet}}$. Apparently, the mean pressure distribution pattern changed remarkably as the relative location of the high-rise building model changed. When the high-rise building was at the center, the downdraft flow impinged on the roof of the building and local pressure coefficient reached approximately 1. Because the airflow was not directly stagnated at four walls, pressure coefficients on the sidewalls were less than 1, though a relatively high value about 0.75 covered most of area. Since the entire building was immersed into this high-pressure stagnation region, the pressure difference between external and internal pressure may pose some potential safety problems for a sealed high-rise building. It also should be noted that the stagnation point shifted slightly to the left and caused a $\mathrm{C_p} \approx 0.95$ region at the bottom of the left wall. This was caused by either the systematic uncertainty of identifying the geometric center of the jet or the slight non-uniformity of the jet velocity profile. However, this trivial systematic error does not affect the overall discussion of this study. At $\mathrm{r/D} \approx 0.5$, high positive pressure was found on the windward wall, which could be attributed to both the local high static pressure and the stagnation of the expanding outburst flow. The local high static pressure also covered most of the regions

on the leeward wall and sidewalls, though flow separation reduced the positive pressure at sidewall corners and the upper half of the leeward wall. Therefore, it can be concluded that when the microburst center is near the location of the high-rise building, both the airflow itself and the local high static pressure contribute to the external pressure distribution on the building surface. It is exactly the opposite situation of a tornado wind, in which the pressure drop is the major concern.

When the high-rise building was located further away from the microburst center, i.e. at r/D≈1.0, 1.5, and 2.0, the effects of the local static pressure vanished and the external pressure distribution was mainly determined by the local wind profile. Because the maximum wind speed was found near ground at these locations, the high positive pressure on the windward wall was only found at lower levels, i.e. z/H<0.5, and gradually decreased towards the roof-height. The stagnation point on the windward wall was found very close to the ground instead of around z/H≈0.7 in the ABL wind and the overall distribution on the windward wall showed an "upside-down" pattern of those observed in boundary layer winds [26-27]. As a function of radial location, the high positive pressure was also found to decrease as the high-rise building moved from r/D≈1.0 to 2.0. Negative pressure was found at both sidewalls due to the flow separation at the leading edges, which could also be expected in the normal ABL wind. It was interesting to note that the minimum negative pressure on the sidewall also occurred at r/D≈1.0, but at a higher level (z/H≈0.7-0.8) compared with that of the maximum positive pressure on the windward wall. At the level of the minimum negative pressure, C_p≈-0.57 was found near the leading edge and then recovered quickly on downstream side,

indicating the flow reattached at the rear sidewalls and the "separation bubble" formed at the minimum pressure location. On the contrary, negative pressure at the lower level of the sidewalls, away from the ground, had a relatively smaller absolute value but distributed more uniformly, suggesting that the separated flow did not reattach to the sidewall. This difference of flow separation regime was closely related to the difference of wind speed and turbulence level between the upper and lower parts of the building model, as shown in Figure 5. While low wind speed and high turbulence helped flow reattach on the sidewall at higher levels, high wind speed and low turbulence forced the flow to separate completely at lower levels. As the velocity and turbulence distribution got more uniform vertically at r/D≈1.5 and 2.0, the height of minimum negative pressure gradually decreased to the same height of the maximum positive pressure found at the windward wall.

4.2 Comparison with the ABL Wind

In this section, data were extracted and plotted in both vertical and circumferential direction at five radial locations and compared with those obtained in ABL wind. It should be noted that since the non-dimensionalization was based on different reference velocity in the microburst wind (V_{jet}) and the ABL wind (U_H, longitudinal velocity at building roof height), the pressure and force coefficients could only be used for the comparison of distribution patterns of the mean wind loads. It is reasonable to expect much larger mean wind loads acting on the building due to the commonly higher wind speed produced in the microburst flow field.

Figure 7 (a) shows the comparisons of the local drag coefficient when high-rise building was at different radial locations with 0 degree orientation (wall normal to the wind direction). The local drag coefficient was computed by averaging the pressure difference between windward and leeward wall at each of 10 elevations where pressure taps were placed. At the center, local drag coefficient is around zero. At r/D≈0.5, the local drag coefficient was slightly higher at z/H>0.5 but quite uniform over the building. In the outburst region, i.e. at r/D=1.0, 1.5, and 2.0, the lower half of the building (z/H<0.5) experiences larger local drag. These results and trends all correspond well with the previous observation in Figure 6. Figure 7 (b) presents a comparison between result at r/D=1/0 in the present study and the wind tunnel testing results obtained by Lin et al. [5] and Kim and Kanda [12] in the ABL wind tunnel. Either of these studies included a square high-rise building model with the same H/B ratio of 4. The local drag coefficients were compared based on similar normalization parameter, namely the maximum velocity in each case. In present study, the maximum radial velocity was expected at r/D=1.0, which is approximately equal to V_{jet}. In the previous two studies, the local drag coefficients were also calculated using the maximum wind speed experienced by the building, namely the wind speed at the roof height U_H. In the conventional boundary layer wind, the along-wind force coefficient is found to increase monotonically before it reached maximum at the stagnation point around z/H≈0.85. Apparently, the distribution induced by the microburst outburst flow showed an overall opposite trend as compared with the normal ABL wind. This kind of distribution could pose more along-wind load on lower elevations of the high-rise buildings, but less

overall bending moment on the building than that produced by an equivalently strong boundary layer winds. Calculation shows that the bending moment at r/D=1.0 in the present study is approximately 57% and 62% of that produced by conventional boundary layer winds simulated by Lin et al. and Kim and Kanda, respectively.

Figure 8 compares the circumferential distribution of pressure coefficients at two heights, i.e. H/3 and 2H/3, with those obtained by Melbourne [2], and Tanaka and Lawen [4] in the ABL wind. Both of these two previous studies used the CAARC building which has the same H/B ratio of 4 but not square cross-section (aspect ratio≈1.5). The short depth of the CAARC building model resulted in a complete flow separation without reattachment the sidewalls as demonstrated by the flat pressure distribution between point 1 and 2. Again the pressure coefficient in the previous data was calculated using roof-height wind speed U_H, while the jet velocity V_{jet} was used here in the present study. Generally, it can be seen that the pressure distribution on the windward wall at H/3 has a better correlation with the date at 2H/3 in the previous study. This again proves the microburst outburst wind could induce an "upside-down" positive pressure distribution on the windward side of the high-rise building. Except for the z=H/3 case at r/D=1.0, negative pressure on sidewalls was found to gradually recover from point 1 to point 2, suggesting a flow reattachment at the rear portion of the sidewalls. It should also be noted that the absolute value of negative pressure on both sidewalls and leeward walls were constantly smaller than those found in ABL wind. This difference may arise from the higher turbulence in the outburst flow. Similar discrepancies among different ABL wind tunnel testing results were also discussed in

Huang et al. [26]. It was suggested that the negative pressure on the sidewalls and leeward wall was quite sensitive to a number of laboratory conditions, such as blockage ration, surface roughness, turbulence level, and etc., while positive pressure on the windward wall was less sensitive to these factors.

4.3 Overall Mean Wind Loads

The overall along-wind and across-wind force acting on the entire high-rise building model were obtained using two methods, by integrating the surface pressure and directly using the force balance transducer. Figure 9 presents these two types of force coefficients measured at five different radial locations corresponding to three different orientation angles with respect to the oncoming flow, i.e. 0 degree (wind normal to the wall), 22.5 degree, and 45 degree. Both these two force coefficients were normalized using jet velocity, i.e. $CF = F/(0.5\rho V_{jet}^2 A)$, where the reference area was held constant as A=B×H to compare the relative magnitude of different orientation cases. The results calculated by pressure integration are shown as hollow dots, while the force balance measurement results are shown as solid dots. It can be seen that the pressure integration method reasonably reproduced the overall wind loads comparing with the direct measurements using load cells, even though the spatial density of the pressure taps was limited.

The along-wind force coefficient in Figure 9 (a) generally showed an increasing and then decreasing trend as the distance from the center increased from r/D=0.0 to 2.0. This result infers that the high-rise building would experience the maximum along-wind force if a microburst occurs 0.5D to 1.0D away from it. These results and trends are closely

related to the variation of the flow field as discussed in previous sections. It is interesting to note that the along-wind force coefficient is found to be dependent on orientation of the building at r/D=0.5, while this difference was not obvious in outburst region, i.e. r/D $\geqslant$ 1.0. This can be explained by showing the change in pressure distribution with building orientation in Figure 10. The overall along-wind force is a function of both the surface pressure and the projection area. At r/D=0.5, the area with high positive pressure increased significantly as the orientation changed from 0 to 45 degree, causing the increase of the along-wind force. However, in the outburst region e.g. r/D=1.0, the effect of increasing projection area was balanced by the decreasing, positive pressure on the windward side due to the inclined surface toward the wind at non-zero orientation cases.

The mean across-wind force coefficients are shown in Figure 9 (b). Since the flow field was essentially axisymmetric, the mean across-wind force was expected to be negligible when the building model was mounted in a symmetric way, for example, 0 degree and 45 degree. At 22.5 degree orientation, the pressure distribution became asymmetric as shown in Figure 10. The maximum mean across-wind force coefficient was found to be about -0.2 at r/D=0.5, while it was quite small in the outburst region. In general, the mean across-wind force is much smaller than the along-wind force and would not be a serious concern for the safety of a high-rise building with a similar square plan.

5. Dynamic Wind Loads

5.1 RMS Pressure Distribution

The distribution of RMS pressure coefficient, which is defined as the root-mean-square of the fluctuating pressure coefficient, is shown in Figure 11. These results correspond to five radial locations (r/D) discussed in previous sections. At the center, the pressure fluctuation is quite small all over the surface, though mean pressure is high as observed in Figure 6. At r/D=0.5, a slightly higher fluctuation results perhaps from the flow separation expected at the upper edge of the sidewall and the mid-level of the leeward wall. These distribution patterns were produced by the unique flow and pressure characteristics of the microburst wind and normally not seen in the ABL wind situation. At r/D>1.0, higher pressure fluctuations were found on the sidewalls due to the flow separation, which is similar with the ABL wind induced pressure fluctuation [2] [4]. The maximum pressure fluctuation typically occurred at where the minimum negative pressure was found in Figure 6. It was also found that pressure fluctuation on sidewalls at r/D=1.5 and 2.0 was greater than that at r/D=1.0, even though the wind was found stronger at r/D=1.0. Meanwhile, the pressure fluctuation on the windward wall, which was considered to be directly related to the turbulence level of the oncoming wind, was also found to increase as the radial distance increased to r/D=1.5 and 2.0.

The local RMS force coefficients were again calculated and compared with those obtained in the ABL wind by Lin et al [5]. Figure 12 and Figure 13 present the local RMS along-wind and across-wind force coefficients at five radial locations and the comparisons. Generally, the local force fluctuation in both directions was closely related

to the local turbulence level displayed in Figure 5. First of all, the turbulence developed along radial direction and hence fluctuations at r/D=1.5 and 2.0 were apparently larger than at other radial locations. Second, strong turbulence also formed within the shear layer above z/H≈0.5 as shown in Figure 5. Therefore, the local force fluctuation at high levels of the building model was generally higher, particularly at r/D=0.5 and 1.0, as hypothesized. It was also found that the fluctuation of local across-wind force coefficients was commonly greater than the along-wind force. This corresponded to the large pressure fluctuation on the sidewalls induced by flow separation, as revealed in Figure 11. The local force fluctuation in the ABL wind showed relatively simpler distributions in Figure 12 (b) and Figure 13 (b). The along-wind force fluctuation increased monotonically along the building height, while the across-wind increased slightly before it decreased towards the roof height. This comparison implies that a greater complexity of the dynamic wind loads could be expected in a microburst wind than in the ABL wind. Again, as aforementioned, the comparison of RMS force coefficients does not imply the relative strength of the force fluctuation due to the different normalization parameter used in the present study. Since the microburst wind is normally stronger, the local force fluctuation could exceed those expected in normal ABL wind in most cases.

5.2 Overall RMS Wind Loads

The root-mean-squares of fluctuating force coefficients acting on the high-rise building are summarized in Table 1. It can be seen that the overall force fluctuation is also dependent on both the radial location and the building orientation. Generally, the

across-wind force fluctuation is larger than its along-wind counterpart, at r/D≥0.5. At the same radial location, it is found that the building would suffer the largest force fluctuations when it is oriented with 0 degree towards the winds. Based on the unique turbulence development in the microburst flow field, the RMS force coefficients also depend on its relative location with respect to the microburst center. For all orientation cases, the maximum force fluctuation is seen when the building is located at r/D≈1.5. It should be noted that this location does not coincide with the location where maximum mean wind load occurs (r/D≈1.0). This result indicates that due to the complexity of the microburst flow field, maximum mean wind loads and fluctuating loads may not simultaneously occur during a microburst event. Attentions should be paid to both of these effects, respectively, for the safety of a high-rise building.

5.3 Power Spectrum Density

Figure 14 presents the normalized power spectrum density (PSD) of the longitudinal velocity fluctuations at the center of the jet and r/D≈1.0 with different heights. The reduced frequency was normalized by the jet velocity and the edge length of the square across-section, i.e. reduced frequency $N_f = fB/V_{jet}$. In Figure 14 (a), it can be seen that due to continuous energy input of the jet and flow regulation of the honeycomb and screens underneath the jet, PSD of all frequency component remained constant and did not decay with higher frequencies. No dominant frequency can be found at the center of the jet. However, at r/D=1.0, a dominant low frequency peak, around $N_f = 0.06\sim0.07$, can be found for velocity fluctuations at multiple heights, as shown in Figure 14 (b) (c) (d). Similar trends can be found at other radial locations in the outburst region and they

are not presented here. This peak PSD in the "energy-containing range" indicates that a large-scale flow structure dominates the flow in the outburst region. At higher frequencies, the normalized PSD of longitudinal velocity fluctuation decreased with a slope of -2/3 obeying the Kolmogorov's "5/3" law in the inertial sub-range, which was also described as $nS(z,n)/u_*^2 = 0.26f^{-2/3}$ in Simiu and Scanlan [28].

As discussed in the authors' previous study [23], the low frequency peak in the power spectrum was caused by the periodic motion of primary vortices in the shear layer. This phenomenon has been observed and verified by many researchers in their studies of the impinging jet flow, such as Ho and Nosseir [29], Didden and Ho [30], etc. Meanwhile, many studies on impinging-jet heat transfer have confirmed that the oscillating behavior of instantaneous Nusselt number distribution results from the periodic motion of primary vortices [31]. To confirm what effects this low-frequency peak in the outburst flow has on the dynamic wind loads acting on the high-rise building model, the PSD of the force coefficient fluctuations was plotted and compared for the radial location r/D≈1.0 in Figure 15.

In the normal ABL wind, the along-wind force PSD often shows a wide-band distribution as it is mainly affected by the oncoming wind turbulence, while the across-wind force PSD usually has a narrow-band peak which is induced by flow separation and vortex shedding [5]. The PSD's of along-wind and across-wind force fluctuations of the high-rise building model are found to be more correlated in the outburst wind than in the ABL wind as shown in Figure 15, particularly in the high-frequency range. The PSD of higher-frequency range for both force components was considerable due to the high

turbulence of the outburst flow. Meanwhile, it is obvious that both PSD plots have low frequency peaks of $N_f = fB/V_{jet} < 0.1$. Although these two peak frequencies are quite close to each other, the underlying physics of them are considered to be different. The peak frequency for the along-wind force fluctuation is found to be very close to the peak of the longitude velocity fluctuation at this location, as shown in Figure.14, implying that the along-wind force fluctuation is more correlated to the oncoming flow turbulence. The peak frequency of across-wind force fluctuation, which is around $N_f = fB/V_{jet} = 0.08$, is most likely contributed by the flow separation at the sidewall edges, which could also be expected in the ABL wind [5]. This peak reduced frequency, if re-normalized by the mean velocity across the building height (~8.6 m/s), is approximately 0.12, which matches the vortex-shedding frequency found for a square cylinder in both smooth and turbulence flow [32]. In addition, the normalized PSD of across-wind force fluctuation is also found to be larger than its along-wind counterpart in the range of $N_f = 0.08\sim0.2$, which may also result from the fine structures of local sidewall vortex shedding.

In general, the power spectrum density of the force fluctuation shows more sophisticated details than those found in the normal ABL wind. All factors discussed above, including low-frequency primary vortices, sidewall flow separations, and high overall turbulence, contribute to the dynamic wind loads on the building model. These unique features of dynamic wind loads should be considered for the design of high-rise building for microburst wind.

6. Summary and Conclusions

A laboratory study was conducted to investigate the nature of wind loads on a high-rise building model induced by a simulated microburst wind. The microburst was reproduced in the laboratory condition using an impinging-jet-based microburst simulator in the Department of Aerospace Engineering, Iowa State University. The high-rise building model used in the present study has a 45 mm×45 mm square cross-section and a total height of 180 mm and was placed at different radial locations (r/D=0.0, 0.5, 1.0, 1.5, and 2.0) with different orientations (0 degree, 22.5 degree, and 45 degree). Velocity and turbulence intensity profiles at different locations within the steady impinging jet flow were accessed. The wind loading effect was studied using two methods, i.e. surface pressure measurement and overall force measurement. Both the mean and dynamic wind loads were analyzed in the present study. Generally, due to the complexity of the flow field, the mean and dynamic wind loads induced by microburst would be more complicated than those produced in the ABL wind. Major findings of the present study are summarized as follows:

1) Mean pressure distribution on the high-rise building depends on the radial location within the microburst flow field. When the high-rise building is located in or near the center of the microburst, i.e. r/D=0.0 and 0.5, the mean pressure distribution around the building surface is greatly influenced by the local high static pressure in the core. When it is located at r/D>0.5, high positive pressure is found on the windward wall and minimum negative pressure is found on the sidewalls. An “upside-down’

distribution pattern is observed due to the unique wind profile in the outburst region compared to the normal ABL wind.

2) Overall mean wind loads are found to depend on the radial locations and the orientations of the building model. For 22.5 and 45 degree orientations, the maximum along-wind force is found at r/D=0.5, while it is found at r/D=1.0 for 0 degree orientation case. The across-wind force is generally negligible except for the 22.5 degree orientation case.

3) Root-mean-square pressure distribution also varies as the radial location changes. Generally, the pressure fluctuation is small when the building is located in or near the center of the microburst. In the outburst region, maximum pressure fluctuation is found on the sidewall edges when the building is located at r/D≈1.5 and 2.0. Local RMS force coefficients also showed that the dynamic wind loads are closely related to the local turbulence level in the outburst region. The local force fluctuation is found to be larger at higher elevations (z/H>0.5) and further radial locations (r/D=1.5 and 2.0).

4) The overall RMS wind load as a function of radial location and orientation are also summarized here. Maximum RMS wind loads are found at r/D=1.5. Across-wind force fluctuation is found to be greater than its along-wind counterpart.

5) Power spectrum density analysis suggests that the low-frequency peak in the PSD of the dynamic wind loads is contributed by the primary-vortex shedding in the outburst region. The PSD of along-wind and across-wind force fluctuation is found to be better correlated than those found in the ABL wind. PSD in the high-frequency range of

the force fluctuation is also considerable due to the high turbulence level in the outburst region.

References

[1] Beers, P.E. http://buildingenvelope.wordpress.com/2011/05/24/hurricane-and tornado-damage-in-urban-areas-%E2%80%93-a-recent-history/ (Hurricane and Tornado Damage in Urban Areas – A Recent History). May 24, 2011

[2] Melbourne, W.H., 1979. Comparison of Measurements on the CAARC Standard Tall Building Model in Simulated Model Wind Flows. Journal of Wind Engineering and Industrial Aerodynamics, 6:73-88

[3] Wardlaw R.L., Moss, G.F., 1970. A standard tall building model for the comparison of simulated natural winds in wind tunnels. CAARC, CC 662m Tech, 1970.

[4] Tanaka H., Lawen N., 1986. Test on the CAARC Standard Tall Building Model with a Length Scale of 1:1000. J. Wind. Eng. Ind. Aerodyn. 25, 15-29.

[5] Lin N., Letchford C.W., Tamura Y., Liang B. Nakamura O., 2005. Characteristics of wind forces acting on tall buildings. J. Wind. Eng. Ind. Aerodyn. 93, 217–242.

[6] Kwok K.C.S., 1982. Cross-wind response of tall buildings. Eng. Struct. 4, 256-262.

[7] Kawai H., 1992. Vortex induced vibration of tall buildings. J. Wind. Eng. Ind. Aerodyn. 41-44, 17-128.

[8] Marukawa H., Ohkuma T., Momomura Y., 1992. Across-wind and torsional acceleration of prismatic high rise buildings. J. Wind. Eng. Ind. Aerodyn. 41-44,1139-1150.

[9] Kareem A., 1992. Dynamic response of high-rise buildings to stochastic wind loads. J. Wind. Eng. Ind. Aerodyn. 41-44, 1101-1112.

[10] Kwok K.C.S., 1988. Effect of building shape on wind-induced response of tall building. J. Wind. Eng. Ind. Aerodyn. 28, 381-390.

[11] Kim Y.M., You K.P., Ko N.H., Across-wind responses of an aeroelastic tapered tall building. J. Wind. Eng. Ind. Aerodyn. 96, 1307–1319.

[12] Kim Y., Kanda J., 2010. Characteristics of aerodynamic forces and pressures on square plan buildings with height variations. J. Wind. Eng. Ind. Aerodyn. 98, 449–465.

[13] Sykes D.M., 1983. Interference effects on the response of a tall building model. J. Wind. Eng. Ind. Aerodyn. 11, 365—380.

[14] Kareem A., 1987. The effect of aerodynamic interference on the dynamic response of prismatic structures. J. Wind. Eng. Ind. Aerodyn. 25, 365-372.

[15] Taniike Y., 1992. Interference mechanism for enhanced wind forces on neighboring tall buildings. J. Wind. Eng. Ind. Aerodyn. 41-44, 1073-1083.

[16] Lam K.G., Zhao J.G., Leung M.Y.H., 2011. Wind-induced loading and dynamic responses of a row of tall buildings under strong interference. J. Wind. Eng. Ind. Aerodyn. 99, 573–583.

[17] Chen L., Letchford C.W., 2004. Parametric study on the along-wind response of the CAARC building to downbursts in the time domain. J. Wind. Eng. Ind. Aerodyn. 92, 703–724.

[18] Sengupta A., Haan, F.L, Sarkar, P.P., Balaramudu V., 2008. Transient loads on buildings in microburst and tornado winds. J. Wind. Eng. Ind. Aerodyn. 96, 2173-2187.

[19] Yang Z.F., Sarkar P.P., Hu H., 2011. An experimental study of flow field around a high-rise building model in tornado-like winds. Journal of Fluids and Structures, 27(4), 471-486.

[20] Irwin P.A., 2009. Wind engineering challenges of the new generation of super-tall buildings. J. Wind. Eng. Ind. Aerodyn. 97, 328–334.

[21] Fujita, T. T., 1985. The Downburst. SMRP Research Paper, University of Chicago Press

[22] National Weather Service, http://www.erh.noaa.gov/cae/svrwx/downburst.htm

[23] Zhang Y., Sarkar P.P., Hu H., 2012. Experimental and Numerical Investigations on the Flow Characteristics of Microburst-like Winds. 50th AIAA Aerospace Sciences Meeting including the New Horizons Forum and Aerospace Exposition 09 - 12 January 2012, Nashville, Tennessee, AIAA 20121197.

[24] Irwin H.P.A.H., Cooper K.R., Girard R., 1979. Correction of distortion effects caused by tubing systems in measurements of fluctuating pressures. Journal of Industrial Aerodynamics, 5, 93-107.

[25] Hjelmfelt, M.R., 1988. Structure and life cycle of microburst outflows observed in Colorado. J. Appl. Meteorol. 27(8), 900-927.

[26] Huang S., Li Q.S., Xu S., 2007. Numerical evaluation of wind effects on a tall steel building by CFD. Journal of Constructional Steel Research 63, 612–627.

[27] Braun, A.L., Awruch, A.M. 2009. Aerodynamic and aeroelastic analyses on the CAARC standard tall building model using numerical simulation. Computers and Structures 87, 567-581.

[28] Simiu E., Scanlan R.H., 1996. Wind effects on Structures, an introduction to wind engineering, second edition. John Wiley & Sons, New York. Page 53-54.

[29] Ho C.M., Nosseir N.S., 1981. Dynamics of an impinging jet. Part 1. The feedback phenomenon. J . Fluid Mech. 105, 119-142.

[30] Didden N., Ho C.M., 1985. Unsteady separation in a boundary layer produced by an impinging jet. J. Fluid Mech. 160, 235-256.

[31] Chung Y.M., Luo K.H., 2002. Unsteady heat transfer analysis of an impinging jet. Journal of Heat Transfer 124, 1039-1048.

[32] Vickery B.J., 1966. Fluctuating lift and drag on a long cylinder of square cross-section in a smooth and in a turbulent stream. J. Fluid Mech. 25(3), 481-494.

Figure 1. *Building Damages during Hurricane Alicia in 1982 (left) and Hurricane Wilma in 2003 (right), by Beers [1]*

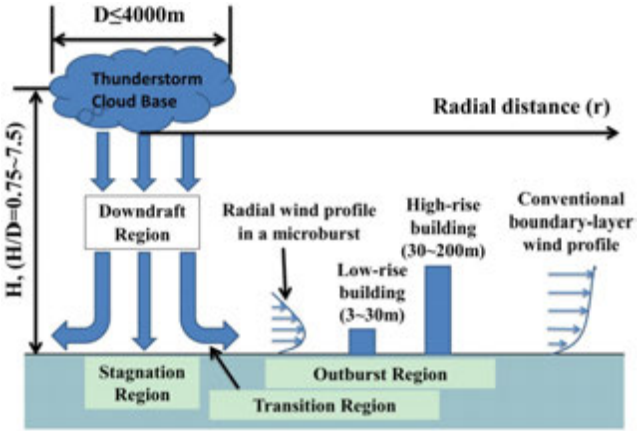

Figure 2. *Schematic of microburst flow field and scale comparison with typical low-rise and high-rise buildings*

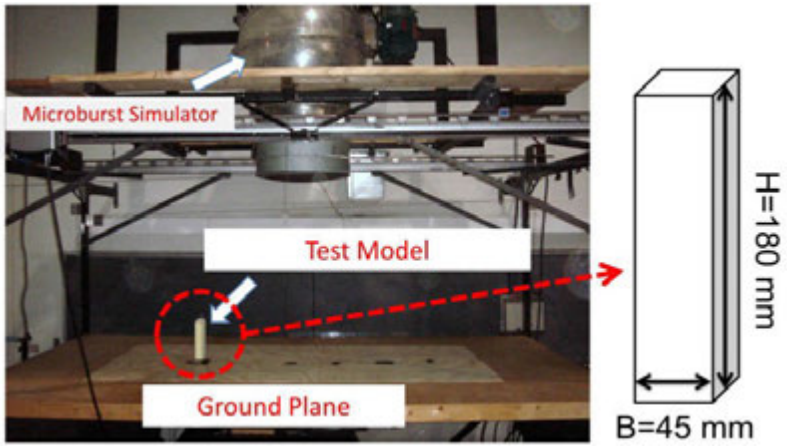

Figure 3. *Microburst simulator and dimensions of high-rise building model*

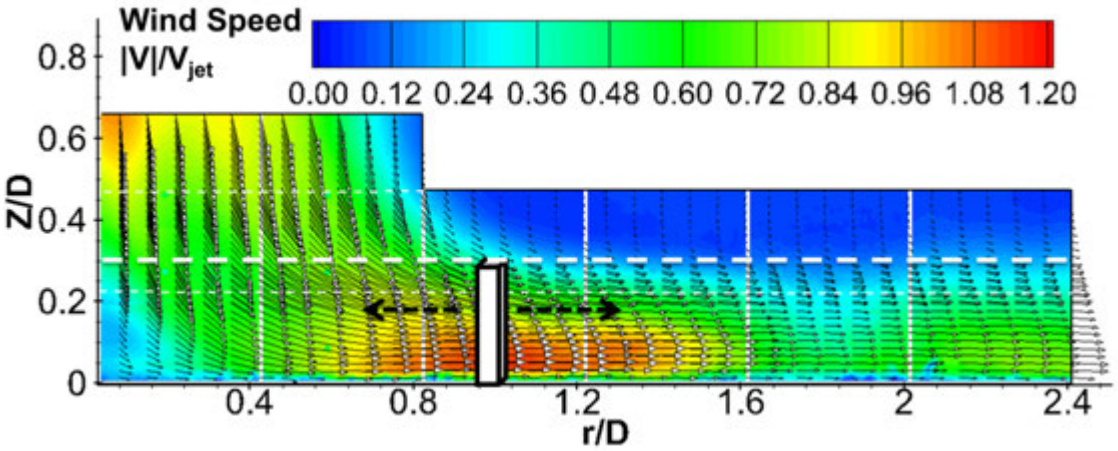

Figure 4. *PIV velocity contour of the microburst flow field and scale comparison with the building model*

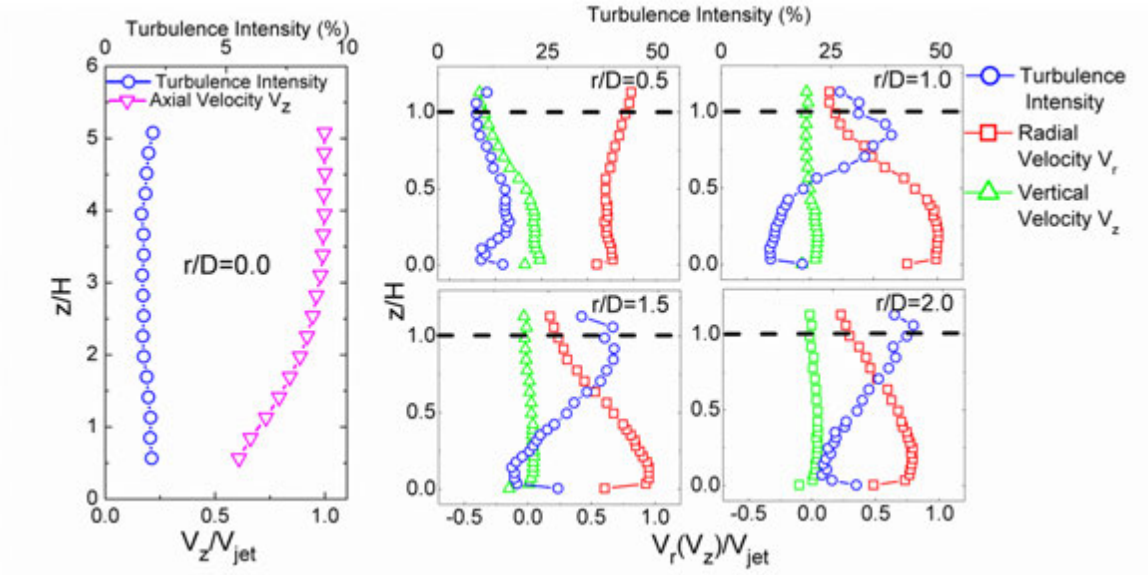

Figure 5. *Velocity and turbulence intensity profiles at different radial locations*

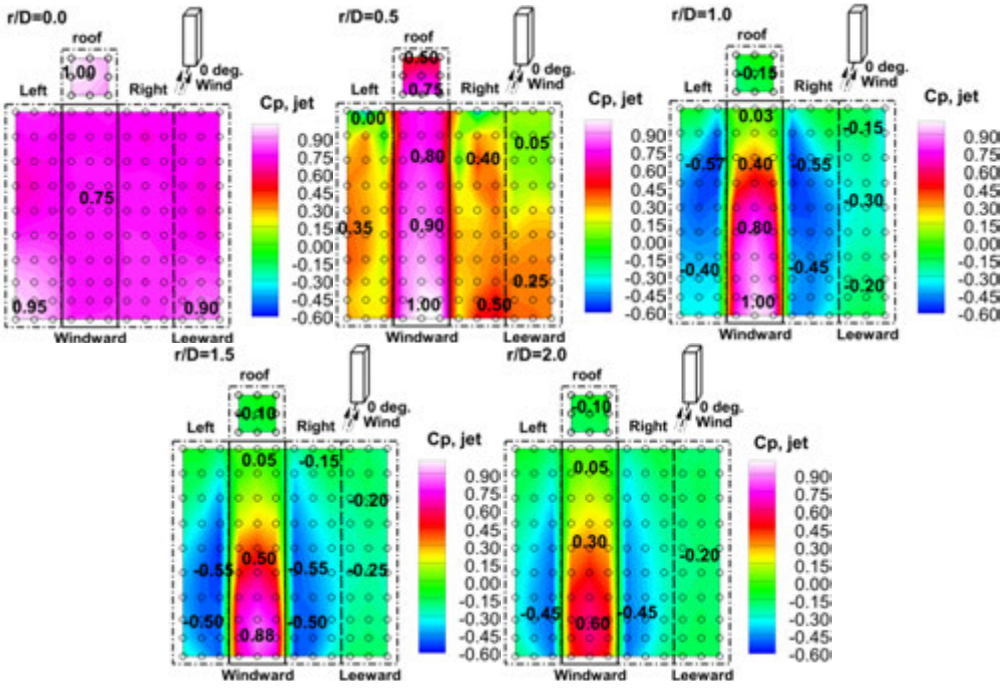

Figure 6. *Mean pressure distribution on the high-rise building model at different r/D's*

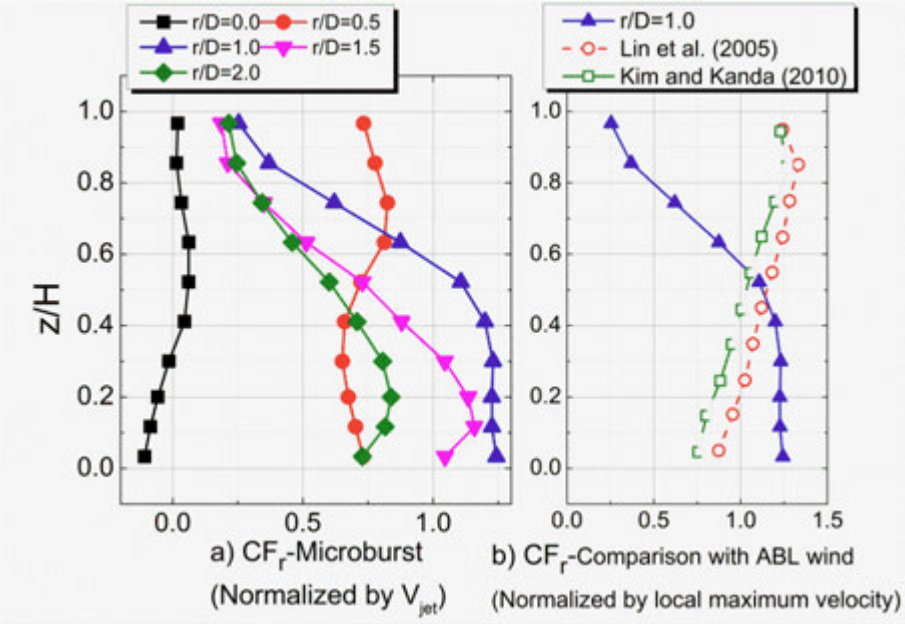

Figure 7. *Mean local along-wind force coefficients and comparison with data in ABL wind*

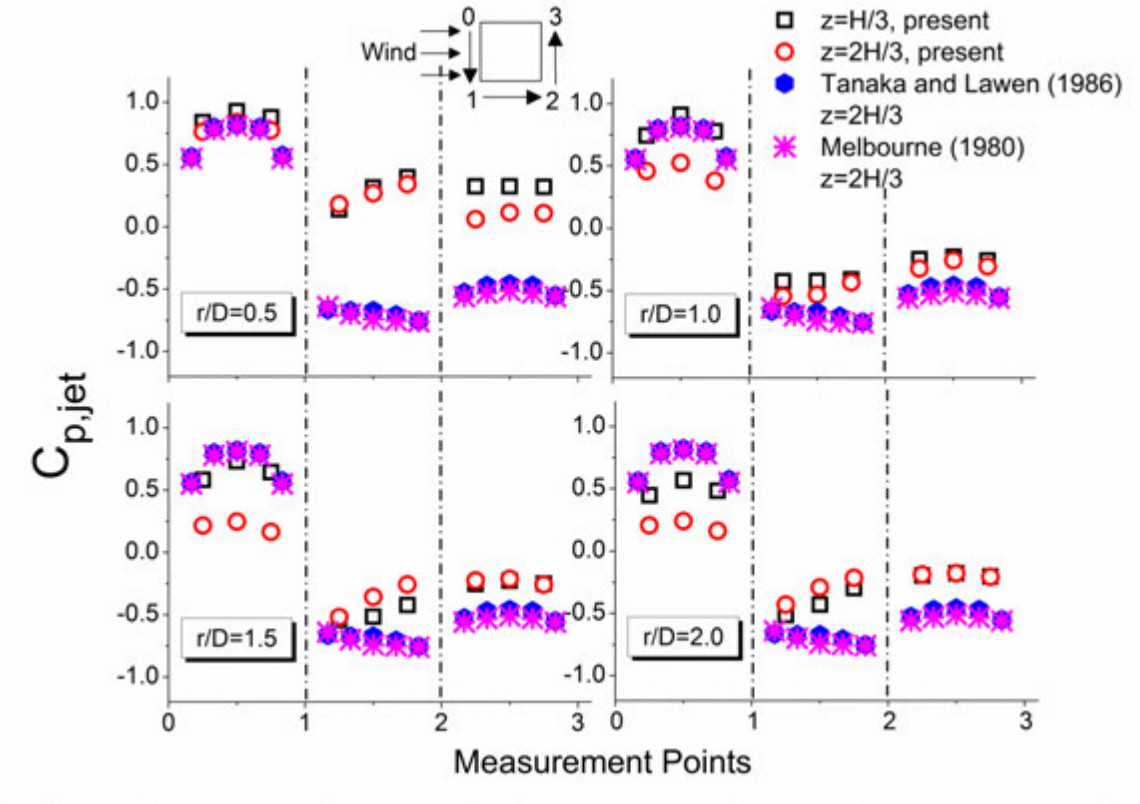

Figure 8. *Mean pressure coefficients in circumferential direction and comparison with data in ABL wind*

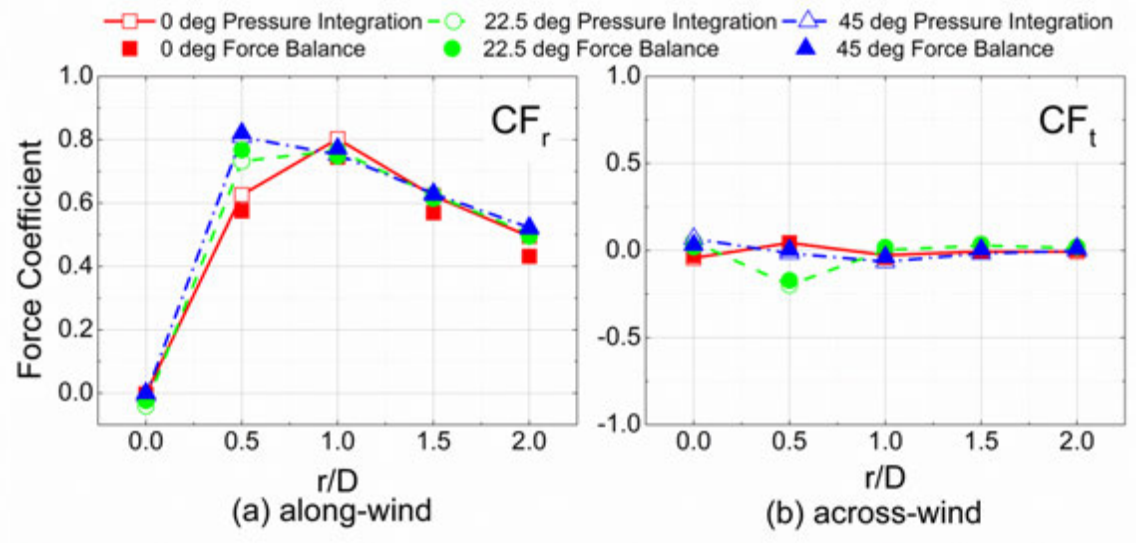

Figure 9. *Mean overall wind loads at different radial locations and with different orientations*

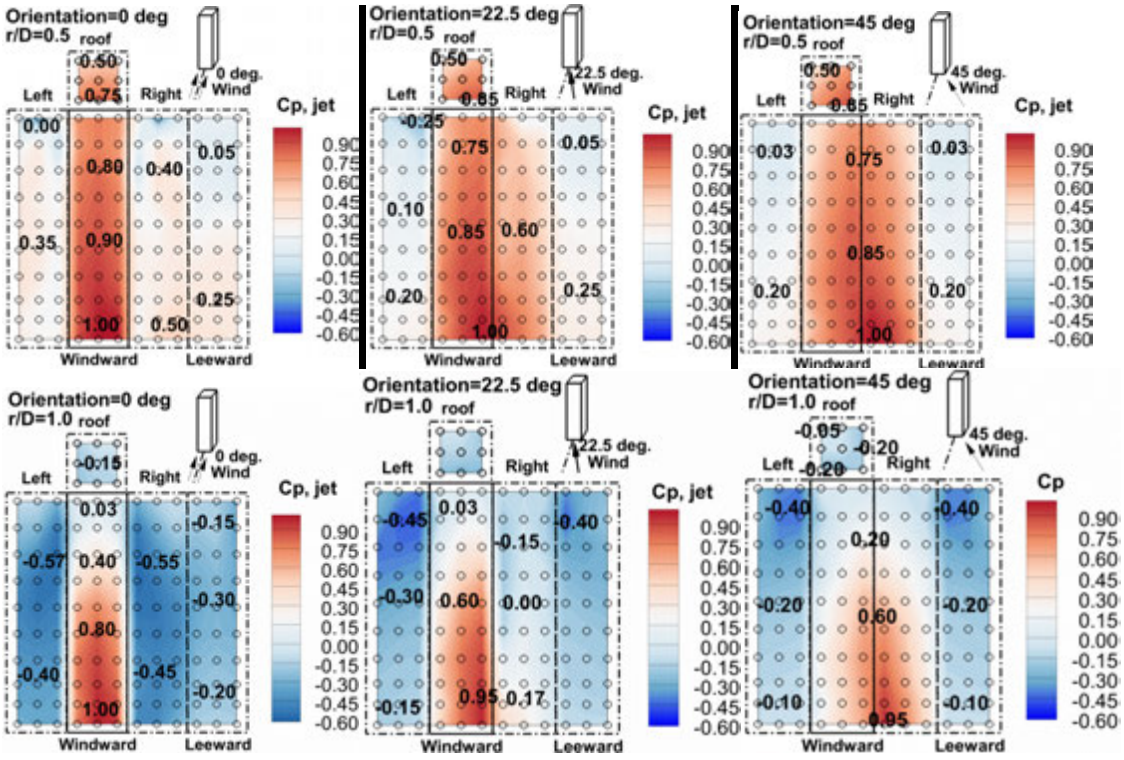

Figure 10. *Mean pressure distributions for different orientations at the same radial location*

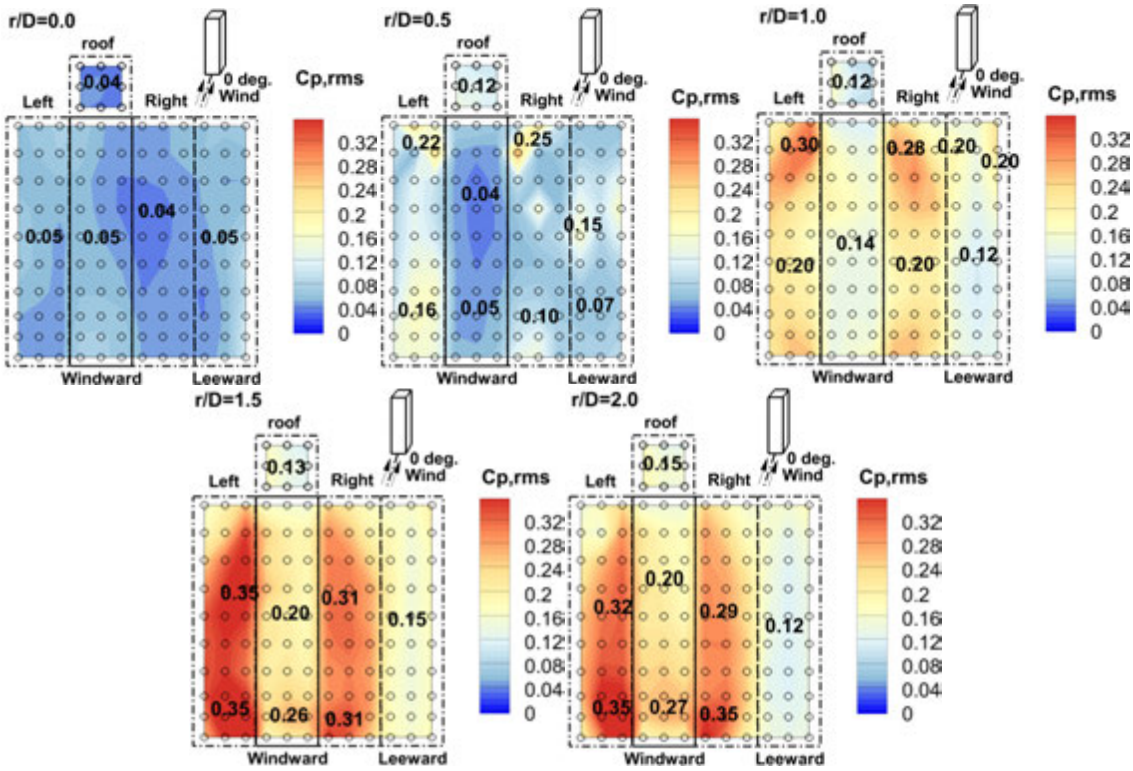

Figure 11. *Distribution of root-mean-square of pressure fluctuation*

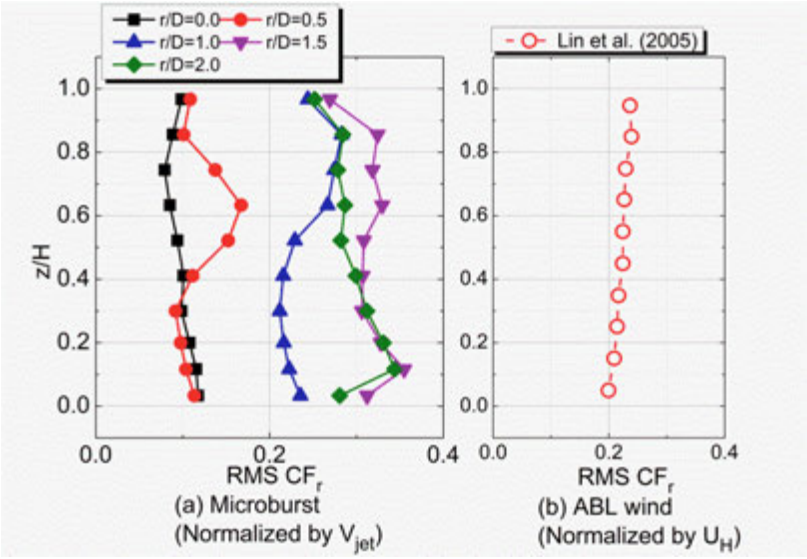

Figure 12. *Root-mean-square of local along-wind force fluctuation and comparison with data in the ABL wind*

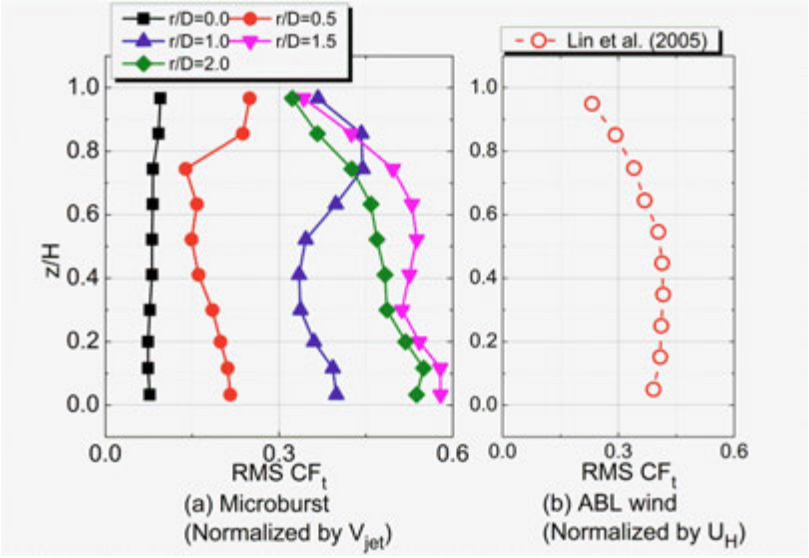

Figure 13. *Root-mean-square of local across-wind force fluctuation and comparison with data in the ABL wind*

Table 1. *Root-mean-square of overall force fluctuations*

r/D	RMS Force Coefficients					
	0 degree		22.5 degree		45 degree	
	CF_r	CF_t	CF_r	CF_t	CF_r	CF_t
0	0.17	0.13	0.14	0.10	0.13	0.10
0.5	0.12	0.15	0.12	0.13	0.10	0.12
1	***0.21***	0.28	0.15	0.16	0.15	0.15
1.5	***0.21***	***0.32***	***0.15***	***0.19***	***0.18***	***0.19***
2	***0.21***	0.31	0.14	0.19	0.14	0.15

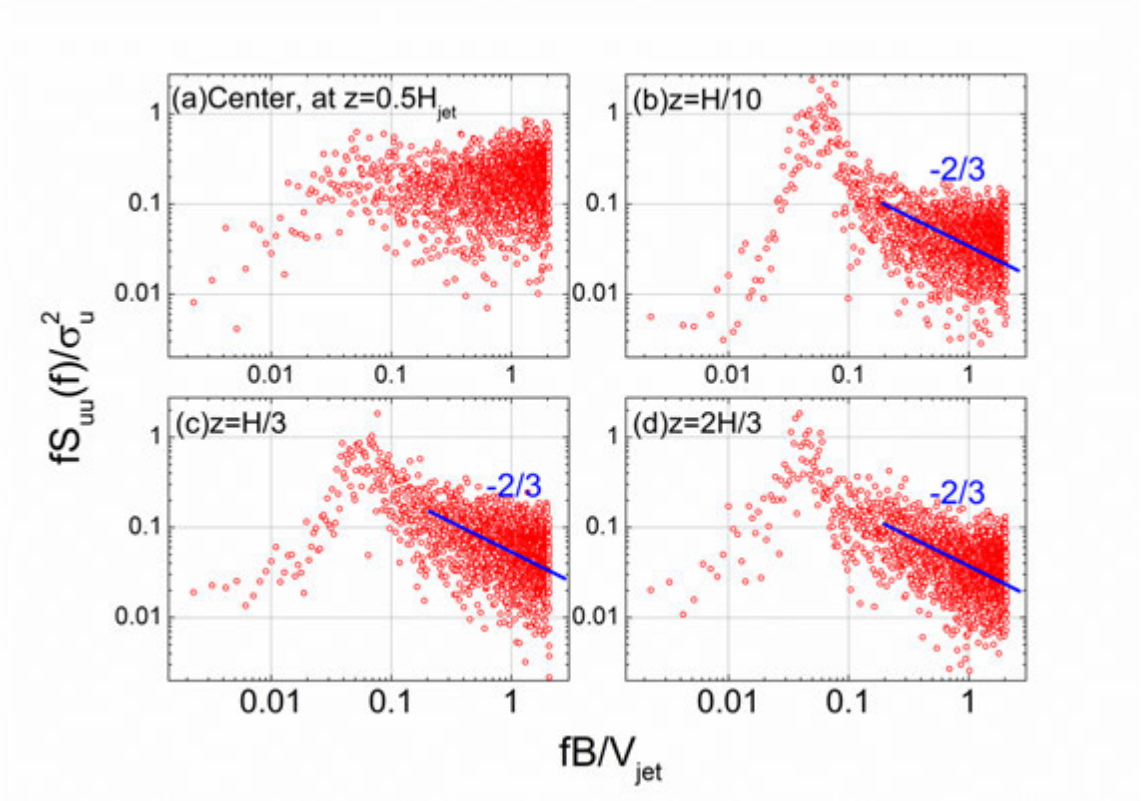

Figure 14. *Power spectrum density of velocity fluctuations at (a) center of the microburst (b)(c)(d) different height at r/D≈1.0*

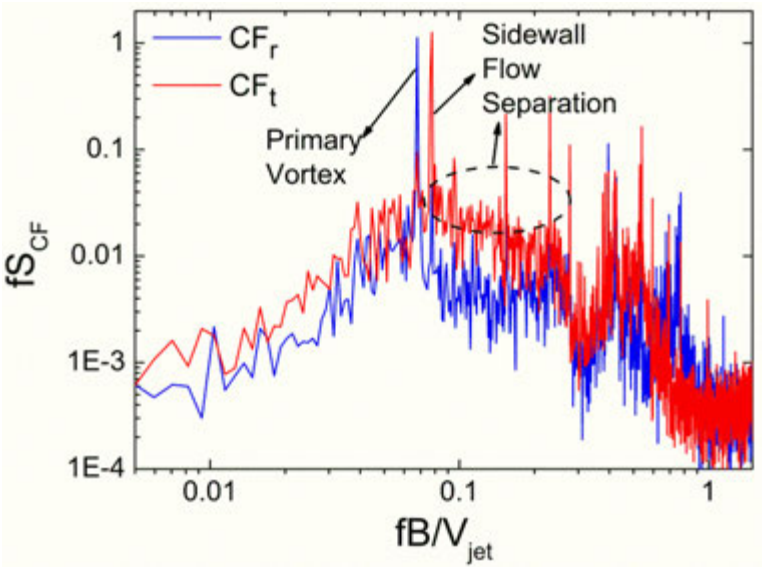

Figure 15. *Power spectrum density of force fluctuations at r/D=1.0*

CHAPTER 6

NUMERICAL SIMULATION OF MICROBURST WIND AND ITS LOADING EFFECTS ON BUILDING MODELS USING AN IMPROVED IMPINGING JET MODEL AND A COOLING SOURCE MODEL

Yan Zhang, Partha P. Sarkar, Hui Hu

Department of Aerospace Engineering, Iowa State University, Ames, Iowa, 50010

Abstract: A numerical simulation was performed to simulate the microburst flow field and its wind loading effects on building models, utilizing an improved impinging jet model and a cooling source model. The macroscopic flow features and a comparison with previous research data suggests that by eliminating the strong shear at the jet interface, the improved impinging jet model provides a reasonable simulation of the transient microburst flow field, similar as the simulation of the cooling source model. Differences in the pressure and velocity distributions at different time-steps were found mainly due to the extra hydrostatic pressure added by the density of the cooled air in the cooling source model. Wind loading effects on the low-rise building were found to be similar in the two models. However, negative pressure on the roof and leeward wall of the high-rise building was found to be considerably lower in the cooling source model, which may result from the different strength and location of the low-pressure region associated with the primary vortex. Besides, the positive pressure on the windward wall was constantly higher in the cooling source model than in the impinging jet model, which may also be attributed to the increased density of the oncoming flow.

1. Introduction

A microburst is defined as an intense downdraft impacting the ground and forming a damaging outflow with a diameter less than 4 kilometers (Fujita, 1985). Due to the unique flow characteristics and near-ground extreme winds, microbursts are dangerous for the safety of aviation and responsible for many damages of civil structures during thunderstorms. Since 1970s, a number of full-scale meteorological studies, including Northern Illinois Meteorological Research on Downbursts (NIMROD) (Fujita, 1985), Joint Airport Weather Studies (JAWS) (Hjelmfelt, 1988) and etc., have been conducted to reveal the formation and microphysical process of a microburst. However, the field data have a few limitations: (1) low resolution near the ground (2) case dependent (3) relatively scarce, which makes it not suitable for wind engineering studies. Therefore, several researchers have tried to use different modeling methods to reproduce the microburst phenomenon in either physical or numerical simulations.

The steady-impinging-jet model has been widely adopted due to its simplicity and ability to produce reasonable outflow profile representing a microburst at its maximum strength (Selvam and Holmes, 1992; Holmes, 1999; Wood et al., 2001; Chay et al., 2005; Kim and Hangan, 2007; Sengupta and Sarkar, 2008; Zhang et al., 2012; etc.). However, the steady impinging jet intrinsically ignores the time-domain evolution of the flow field, which contains critical information for a realistic microburst event. To study the transient behavior of a microburst, several laboratory and numerical simulations have been performed by researchers, deploying either an impinging jet or a cooling source approach. These laboratory studies include dropping denser fluid into water (Lundgren

et al., 1992; Alahyari and Longmire, 1995; Yao and Lundgren, 1996) and using pulsed jet (Mason et al., 2005). Numerical simulation known as cooling source model uses a simplified sub-cloud model, as suggested by Anderson et al. (1992), which is computationally less complex than the meteorological full-cloud model. It has been proven that this cooling source model is capable of producing a transient wind velocity profile resembling that obtained in the field study (Orf et al., 1996; Orf and Anderson, 1999; Mason et al., 2010; Vermeire et al., 2011; Zhang et al. 2012). Transient behavior of an impinging jet model has also been numerically simulated and compared with those of a cooling source model in Vermeire et al. (2011) and the authors' previous study (Zhang et al. 2012). These comparisons showed that the instantaneous maximum velocity profile generated in the transient impinging jet model deviated from those observed in the field study and simulated cooling source model. This deviation might result from the strong forcing source of the continuous jet and the strong shear at the jet-ambient interface. Therefore, the impinging jet model should be modified in order to get a faithful microburst simulation using this model. Furthermore, even though the flow fields of both modeling methods have been studied extensively, little research has been done to address the different wind loading effects on buildings induced by different modeling methods.

In the present study, 3D numerical simulation has been conducted of full scale. An improved impinging jet model has been introduced to eliminate the effects of constant forcing term and the strong shear at the jet-ambient interface. The jet inlet velocity was designed to change in both spatial and temporal domain in a similar fashion as that of the

cooling source model. The cooling source model was also simulated for a comparison. The macroscopic flow field characteristics of the simulated microburst and the induced flow around two building models, i.e. a high-rise building (square-plan prism) and a low-rise building (cube), have been studied and compared in detail. The differences of wind loading effects on these two buildings induced by the improved impinging jet model and cooling source model were also analyzed.

2. Description of Numerical Models

Three dimensional RANS (Reynolds Averaged Navier-Stokes) simulation ($k-\omega$) was performed in this study using commercially available software FLUENT 12.1 (ANSYS Inc.). According to Sengupta and Sarkar (2008), $k-\omega$ generally gives a better simulation for the impinging jet flow among different turbulence models. The governing equations for the numerical simulation in Cartesian coordinate system are given as follows:

Continuity

$$\frac{\partial \rho}{\partial t}+\frac{\partial}{\partial x_i}\left(\rho u_i\right)=0 \tag{1}$$

Momentum

$$\frac{\partial}{\partial t}\left(\rho u_i\right)+\frac{\partial}{\partial x_j}\left(\rho u_i u_j\right)=-\frac{\partial p}{\partial t}+\frac{\partial}{\partial x_j}\left[\mu\left(\frac{\partial u_i}{\partial x_j}+\frac{\partial u_j}{\partial x_i}-\frac{2}{3}\delta_{ij}\frac{\partial u_k}{\partial x_k}\right)\right]+\frac{\partial}{\partial x_j}\left(-\rho\overline{u_i' u_j'}\right)+f_i \tag{2}$$

The Reynolds stress term $-\rho\overline{u_i' u_j'}$ needs to be modeled to close the equation. The Reynolds stress term was modeled based on Boussinesq hypothesis as

$-\overline{u_i' u_j'} = 2\nu_t S_{ij} - \frac{2}{3} k\delta_{ij}$, where $S_{ij} = \frac{1}{2}\left(\frac{\partial u_i}{\partial x_j} + \frac{\partial u_j}{\partial x_i} \right)$ and ν_t is newly introduced turbulence eddy viscosity term. f_i is the gravitational force term, which was considered in the cooling source model but set to zero in the impinging jet model.

For the cooling source model, the energy equation was also included

$$\frac{\partial}{\partial t}(\rho E) + \frac{\partial}{\partial x_i}\left(u_i(\rho E + p)\right) = \frac{\partial}{\partial x_i}\left(K_{eff} \frac{\partial T}{\partial x_i} \right) + Q(x, y, z, t) \tag{3}$$

where $Q(x, y, z, t)$ is a four dimensional cooling source term, which will be discussed later.

In the present study, the shear-stress transport (SST) $k-\omega$ model was used to solve the turbulence eddy viscosity term. The transport equations for the turbulence kinetic energy k and the specific dissipation rate ω can be found in Menter (1994). Model constants were set to be default values in FLUENT. A second order upwind scheme was used for solving the continuity and momentum equations. Both k and ω were computed using the Quadratic Upstream Interpolation for Convective Kinematics (QUICK) scheme. The PISO scheme was used to provide pressure-velocity coupling. For the transient formulation, a second-order implicit scheme was adopted.

The computational domain and mesh cut-plane are shown in Figure 1. A circular jet inlet with a diameter of 2.5km (D) was placed at the center at an altitude of 2.5km (H). This H/D=1 ratio falls into the range of a real microburst, known to be varying between 0.75 and 7.5. The dimension of the entire domain is sufficiently large, i.e. 10km×10km×3km. As shown in this figure, a high-rise building (10m×10m×50m) and a

low-rise building (10m×10m×10m) were placed in the x-z plane at a coordinate of (2500, 0, 0)m and (-2500, 0, 0)m respectively, such that r/D=1. A structured mesh was used to model this domain with 3.9 million hexahedron cells. The density of the mesh was increased near the ground and around the building locations in order to capture more detailed information. The distance of the first row of the grid was set to be approximately 1m. This resulted in a large dimensionless wall distance value (y+>>30), indicating that the near-wall velocity was fully approximated by logarithmic law. Due to the extremely large computational domain, the cost of simulation would become very high if the mesh is refined enough to solve the viscous sub-layer. However, since the macroscopic flow characteristics are of more interests, this lack of accuracy in the wall viscos sub-layer does not affect the overall discussion in the present study.

The boundary conditions were defined differently for two modeling methods, as shown in Figure 1. For the improved impinging jet model, a velocity inlet condition varying in both space and time was used instead of a constant velocity inlet which was used in Zhang et al. (2012). The jet velocity in this simulation can be expressed as $V_j = K(x,y)K'(t)V_{j\max}$, where $K(x,y)$ and $K'(t)$ are spatial and temporal functions and $V_{j\max}$ is the maximum jet velocity in the entire simulation ($V_{j\max} = 40m/s$). The spatial and temporal velocity distributions are both $\cos^2()$ functions which are illustrated in Figure 2. Outer boundaries were set to be outflow boundary conditions for this incompressible flow problem. For the cooling source model, a cooling function was embedded into the computational domain directly underneath the inlet boundary, by

adding a source term $Q(x,y,z,t)$ into the energy equation (Eqn. 3). The cooling source function was first suggested by Anderson (1992). The spatial and temporal distributions of the cooling source were similar with those displayed in Figure 2, except that the spatial distribution $K(x,y,z)$ is three dimensional. This three-dimensional spatial distribution function of the cooling source can be defined as:

$$K(x,y,z)=\begin{cases}\cos^2(\pi R) & R<0.5\\ 0 & R>0.5\end{cases} \qquad \text{where } R=\sqrt{\left(x/D\right)^2+\left(y/D\right)^2+\left(\left(z-H\right)/D_z\right)^2} \qquad (4)$$

The vertical range of the cooling source is D_z determined by and is set to be 2km. Therefore, the cooling function can be expressed as: $Q(x,y,z,t)=K(x,y,z)K'(t)Q_{\max}$, where $Q_{\max}=Cp\cdot dT$ is the maximum energy input, Cp is the specific heat of air and dT is the temperature changing rate (-0.1k/s in the present study). The inlet- and outer-boundary were defined as pressure inlet and pressure outlet, respectively. Compressible flow condition was used to resolve a density change induced by the cooling function. No-slip wall boundary conditions were defined for both the ground wall and the building walls. The ground surface roughness effect is not discussed in the present study.

3. Results and Discussions

3.1 Macroscopic Evolution of Flow Field

The underlying physics of the impinging jet model (either steady or transient) and the cooling source model were observed to be notably different. While a cooling source model is normally driven by the gravity of the denser fluid, an impinging jet model relies on a momentum forcing source. A traditional impinging jet model, either laboratory or

numerical, usually has a constant and continuous velocity distribution across the jet exit. This distribution induces strong shear at interface, which results in a strong primary vortex immediately after the jet is issued. The strong shear of the jet flow is responsible for the continuously shed vortices and deviation of the maximum velocity profile found in the transient impinging jet (Zhang et al. 2012).The results of the improved impinging jet model suggested here were observed to be quite different from that of the traditional impinging jet mentioned above. Figure 3 and Figure 4 show the evolution of the flow field for the improved impinging jet model and the cooling source model, respectively. In both figures, left columns are the velocity iso-surface where $0.5V_{j\max}$ was found for each model, and the right columns are the velocity contour (normalized by $V_{j\max}$) in x-z plane. The maximum jet velocity $V_{j\max}$ for the two models was not the same (40m/s for the impinging jet and 25m/s for the cooling source). It should also be noted that the time scale for two modeling methods are different due to the intrinsically different underlying physics. Therefore, two set of time notations were used, in which t represents the time for the impinging jet model and τ for the cooling source model. In Figure 3, it can be seen clearly that no strong primary vortex was formed at the downdraft stage (t=100s and 173s), since the velocity profile has been modified to reduce the velocity gradient at the jet interface. At 245s, a relatively stronger reverse flow started to show above the leading edge of the expanding outflow. Later on, this reverse flow rolled into the primary vortex and expanded in radial direction, resulting in a moving maximum velocity region underneath the vortex. At t=336s, this maximum velocity region hit the location where the high-rise building and the low-rise building were placed (r/D=1). No

following vortices, as observed in the traditional impinging jet model, were formed during the process described above.

The evolution of velocity field for the impinging jet model was found to be very similar to that of the cooling source model as illustrated by Figure 4, although the underlying physics for two models were different. For the cooling source model, the primary vortex was also seen after sinking cooled air impacted the ground and the radial expansion started. For the comparison purpose, the velocity iso-surface and contour at $\tau = 514s$ were also provided, when the maximum velocity and the primary vortex reached the building location. Even though the flow fields were similar, some differences can still be visualized between two modeling methods. First, upon hitting the ground, the maximum velocity (relative to $V_{j\max}$) region created by the cooling source model was found to be more significant, comparing the velocity contour at $t = 336s$ and $\tau = 514s$. Second, the core of the expanding primary vortex for the cooling source model was found to be closer to the ground at the time when the primary vortex reached the building locations. These differences are possibly due to the additional hydrostatic pressure and gravitational effects of the cooling source model and may result in different wind loading effects on buildings, which will be discussed in the following section.

To clearly demonstrate these differences, the pressure and velocity profiles (at 10m height) along radial direction were compared in Figure 5 and Figure 6. These profiles were extracted from the flow field along y-direction, where no building obstacles were placed. Two time-steps related to the contours of Figure 3 and Figure 4 are displayed, namely at the time ($t_{-1} = 245s$, $\tau_{-1} = 410s$) when the jet impacted the ground and at the

time ($t_0 = 336s$, $\tau_0 = 514s$) when the primary vortex reached the building locations. In Figure 5, the pressure coefficient is defined as $Cp_{j\max} = \left(p - p_{atm}\right) / \left(0.5\rho V_{j\max}^2\right)$, where $V_{j\max}$ is the maximum jet velocity for each model and ρ is set to be constant (1.225 kg/m^3) for both models. It can be seen that the pressure in the core region of the cooling source model is considerably higher than that of the impinging jet model, particularly at $t_{-1}\left(\tau_{-1}\right)$, which was most likely contributed by the hydrostatic pressure of the descending denser fluids. This result implies that the pressure rise within the microburst dead center might be underestimated by the impinging jet model since no density change is considered. Meanwhile, a notably lower pressure accompanied with the primary vortex was also seen for the cooling source model than that for the impinging jet model, at $t_{-1}\left(\tau_{-1}\right)$. At $t_0\left(\tau_0\right)$, the bandwidth of the high pressure region in the cooling source model decreased as the denser fluid had expanded radially, although the positive pressure of the cooling source model at the center was still significant. Meanwhile, the low pressure in the vicinity of the building location was comparable for the two models at this particular time. Figure 6 shows the wind speed at 10m height along y-direction for both models at same specific time. At $t_{-1}\left(\tau_{-1}\right)$, the maximum normalized wind speed induced by the cooling source model was significantly higher than that induced by the impinging jet model. As the primary vortex expanded, the maximum velocity of the impinging jet model increased, while that of the cooling source model decreased. At $t_0\left(\tau_0\right)$, the maximum velocity of these two models was almost the same, when the

vortex reached the building locations. These results imply that the acceleration of the radial outflow in the cooling source model was triggered much earlier than in the impinging jet model, due to the extra hydrostatic pressure added in the stagnation region. Therefore, it is reasonable to conclude that the microburst simulated by the cooling source model is more destructive for buildings near the center and within the core region ($r/D<0.5$) of the flow field.

To validate the result of the present study, the wind speed profile in vertical direction at $r/D=1$ for each model was extracted and compared with those in the previous studies and the NIMROD field data in Figure 7. The vertical height was normalized by the height (b) where half of the maximum velocity was found so that the uncertainty of the maximum velocity height can be eliminated among different research data. It can be seen that the velocity profiles for both the improved impinging jet model and the cooling source model generally correspond well with the previous cooling source model and the NIMROD field data. Some near-ground discrepancies were seen possibly due to different surface roughness used in the previous studies. Most interestingly, the improved impinging jet model used in the present study provided a much better correlation of the velocity profile as compared with the tradition impinging jet model (Vermeire, 2012; Zhang et al., 2012), by simply removing the strong velocity gradient at the jet interface. Therefore, despite intrinsic differences, both the improved impinging jet model and the cooling source model are reasonable models in terms of the outflow velocity profile.

3.2 Fluid-structure Interaction and Wind Loading Effects

In a steady impinging jet flow, r/D=1 is typically the critical radial location where the maximum radial velocity occurs, as suggested by many previous studies (Zhang et al. 2012). Based on this knowledge, the buildings were placed at r/D=1 in the present simulation. However, the result of the present simulation suggest that the maximum radial velocity for both models occurs before it reached r/D=1 due to the modified velocity and cooling source distribution. In the previous section, it has been discussed that at time $t_0\left(\tau_0\right)$, the primary vortices for both models reached the building locations (r/D=1), and the local pressure and wind speed were comparable at this specific time. To investigate the model differences in wind loading effects, the flow field around the high-rise building and the low-rise building are provided in Figure 8 and Figure 9. For the high-rise building in the impinging jet model (Figure 8(a)), the high-speed flow separated over the roof and the leeward side of the building, forming a reverse flow region behind the building. This flow pattern is very similar to that observed in the boundary layer wind, except that the near ground wind is much more significant. For the cooling source model (Figure 8(b)), the wind speed contours in front of the high-rise building is similar, while flow patterns above and in the wake of the building are different at this specific time compared to that of the improved impinging jet model. This difference was caused by a closer primary vortex to the building in the cooling source model, as illustrated in the zoomed-out velocity contours (Figure 8 (c) (d)). The vortex core was qualitatively determined by the minimum velocity center visualized in these contours. It can be seen that while the vortex core was located at approximately

266m above the roof of the building in the impinging jet model, a much lower location of approximately 179m was seen in the cooling source model. Furthermore, the pressure coefficient contours for these two cases were also dramatically different as shown in Figure 9. As clearly shown, the magnitude and the height of the low-pressure ring were apparently different at this moment, which may directly affect the pressure distribution around the high-rise building, particularly on the roof and leeward side of the building. Figure 10 shows the flow field around the low-rise building. It can be seen that the velocity contours were very similar since it was deeply immersed within the high wind speed region in both two models.

Figure 11 shows the near-ground velocity profiles at r/D=1.0 for two models at the critical time $t_0(\tau_0)$, which were extracted in y-z plane where no building was placed. The heights of the high-rise and low-rise building models are indicated in this plot. It can be seen that at this specific time for comparison, the impinging jet model generates a higher velocity, except that the cooling source has a higher near-ground wind speed under approximately z/D≈0.0025. With these velocity profiles as input, the wind loading effects on the high-rise building and low-rise building were analyzed in Figure 12. The pressure coefficient along the centerline of the building models were extracted and compared at the critical time $t_0(\tau_0)$. Generally, higher positive pressures on the windward wall could be found in the cooling source model, although the oncoming flow velocity is higher in the impinging jet model, particularly for the high-rise building model. This extra wind pressure was contributed by the larger air density of the oncoming flow in the cooling source model. Large discrepancy of the negative pressure

could be seen over the roof and the leeward wall of the high-rise building, which could be attributed to the effect of low pressure region caused by the primary vortex as discussed previously in Figure 9. The negative pressure on the roof and leeward wall of the low-rise building matched very well between two modeling results, indicating a similar flow-structure interaction occurred at this specific time in two models.

4. Conclusions

A numerical simulation was conducted to study the transient macroscopic flow features and wind loading effects on high-rise and low-rise buildings, utilizing an improved impinging jet model and a cooling source model. The impinging jet model incorporated a space- and time-dependent velocity inlet, which was different from the traditional constant velocity inlet. The cooling source model was simulated by adding a cooling source function into the energy conservation equation, which had similar spatial and temporal variation as that the impinging jet model used here.

The macroscopic flow field variation suggests that the improved impinging jet model significantly reduces the shear at the jet interface and eliminates the intense primary vortex during the downdraft stage of the simulated microburst. Generally, the flow structure evolution of these two models was similar, while some differences were visualized. The surface pressure within the core region of the cooling source model was found to be significantly higher than that of the impinging jet model. Due to this extra pressure added by the denser air, it was also found that the cooling source model triggered earlier outflow acceleration after the jet impacted the ground. The radial velocity profile in vertical direction at the critical time was compared with the previous

studies and the field data. A reasonable match was found for each model. In particular, the improved impinging jet model was found to provide a better match of velocity profile with cooling source model and field data than the tradition transient impinging jet model.

The fluid-structure interaction and the wind loading effects in these two models were also analyzed. Generally, the wind loading effects on the low-rise buildings were very similar between two modeling methods. However, due to the difference in relative strength and location of the primary vortex, the flow field and pressure distribution over the roof and in the wake of the high-rise building were found to be different. The cooling source model resulted in lower negative pressure on the roof and leeward wall of the high-rise building than the impinging jet model. Furthermore, due to the increased density of the oncoming flow in the cooling source model, the positive pressure on the windward wall was found to be generally larger than that in the impinging jet model.

References

Alahyari, A., Longmire, E.K., 1995: Dynamics of experimentally simulated microbursts. AIAA Journal. 33 (11), 2128-2136.

Anderson, J. R., Orf, L. G. and Straka, J. M.: A 3-D model system for simulating thunderstorm microburst outflows, Meteor. Atmos. Phys., 49, 125–131, 1992.

Chay. M.T., Albermani, F., and Wilson, R., 2005: Numerical and analytical simulation of downburst wind loads. Engineering Structures. 28, 240-254

Fujita T.T., 1985: The downburst, microburst, and macroburst. SMRP Res. Paper No. 210 [NTIS No. PB85-148880], Univ. of Chicago.

Hjelmfelt M.R., 1988. Structure and life cycle of microburst outflows observed in Colorado. J. Appl. Meteorol, 27(8), 900-927.

Holmes, J. D., 1999: Modeling of Extreme Thunderstorm Winds for Wind Loading of Structures and Risk Assessment. Wind Engineering into the 21st Century, Proc. of the 10th Intl. Conf. on Wind Eng. eds. A. Larsen et al., Denmark, June 1999, 1409−1415.

Kim J. and Hangan H., 2007: Numerical simulation of impinging jets with application to downbursts. J. Wind Eng. and Ind. Aerodyn. 95, 279-298.

Lundgren, T.S., Yao, J., Mansour, N.N., 1992: Microburst modeling and scaling. J. Fluid Mech. 239, 461-488.

Mason, M.S. Letchford, C.W. and James, D.L. 2005: Pulsed wall jet simulation of a stationary thunderstorm downburst, Part A: Physical structure and flow field characterization. J. Wind Eng. and Ind. Aerodyn. 93, 557-580.

Mason, M.S., Wood, G.S., and Fletcher, D.F. 2010: Numerical investigation of the influence of topography on simulated downburst wind fields. J. Wind Eng. and Ind. Aerodyn. 98, 21-33.

Menter. F.R., 1994. Improved two-equation k-omega turbulence models for aerodynamic flows. AIAA Journal. 32(8), 1598-1605.

Orf, L.G., Anderson, J.R. and Straka, J.M. 1996: A Three Dimensional Numerical Analysis of Colliding Microburst Outflow Dynamics. J. Atmospheric Sciences. 53(17), 2490-2511.

Orf, L.G., and Anderson, J.R. 1999: A Numerical Study of Traveling Microbursts. Monthly Weather Review. 127, 1244-1258.

Selvam, R.P., Holmes, J.D. (1992) Numerical simulation of thunderstorm downdrafts. J Wind Eng Ind Aerod 44: 2817-2825.

Sengupta, A., Sarkar, P. P., 2008: Experimental measurement and numerical simulation of an impinging jet with application to thunderstorm microburst winds. J. Wind Eng. and Ind. Aerodyn. 96, 345-365.

Wood, G.S., Kwok, C.S., Motteram, N.A., Fletcher, D.F., 2001. Physical and numerical modelling of thunderstorm downbursts. J. Wind Eng. and Ind. Aerodyn. 89, 535–552.

Vermeire B.C., Orf L.G., Savory E., 2011. Improved modelling of downburst outflows for wind engineering applications using a cooling source approach. J. Wind Eng. and Ind. Aerodyn., 99(8), 801-814.

Yao, J., Lundgren, T.S., 1996. Experimental investigation of microbursts. Exp. Fluids 21, 17–25.

Zhang Y., Sarkar P.P., Hu H., 2012. Experimental and Numerical Investigations on the Flow Characteristics of Microburst-like Winds. 50th AIAA Aerospace Sciences Meeting including the New Horizons Forum and Aerospace Exposition 09 - 12 January 2012, Nashville, Tennessee, AIAA 20121197.

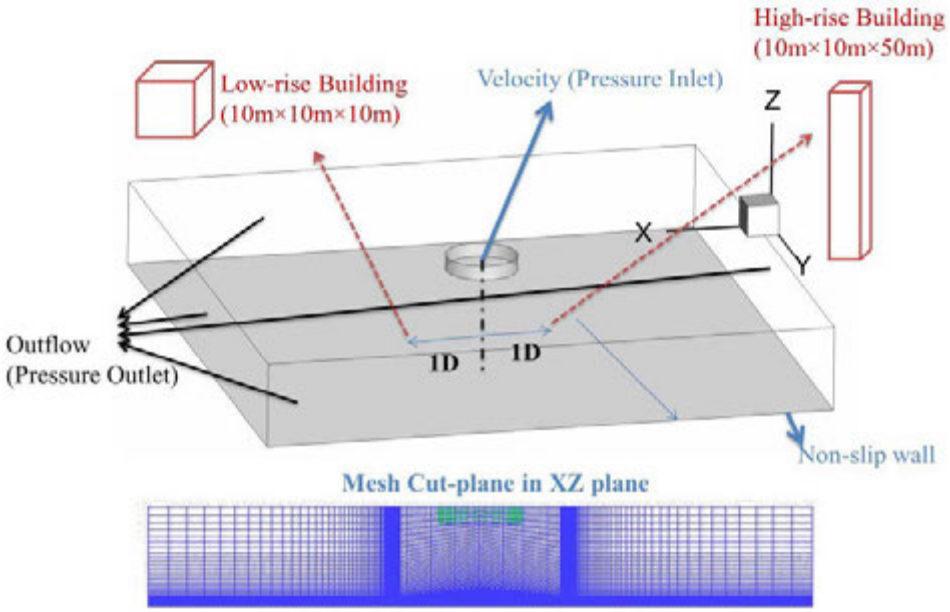

Figure 1. *Computational domain and mesh*

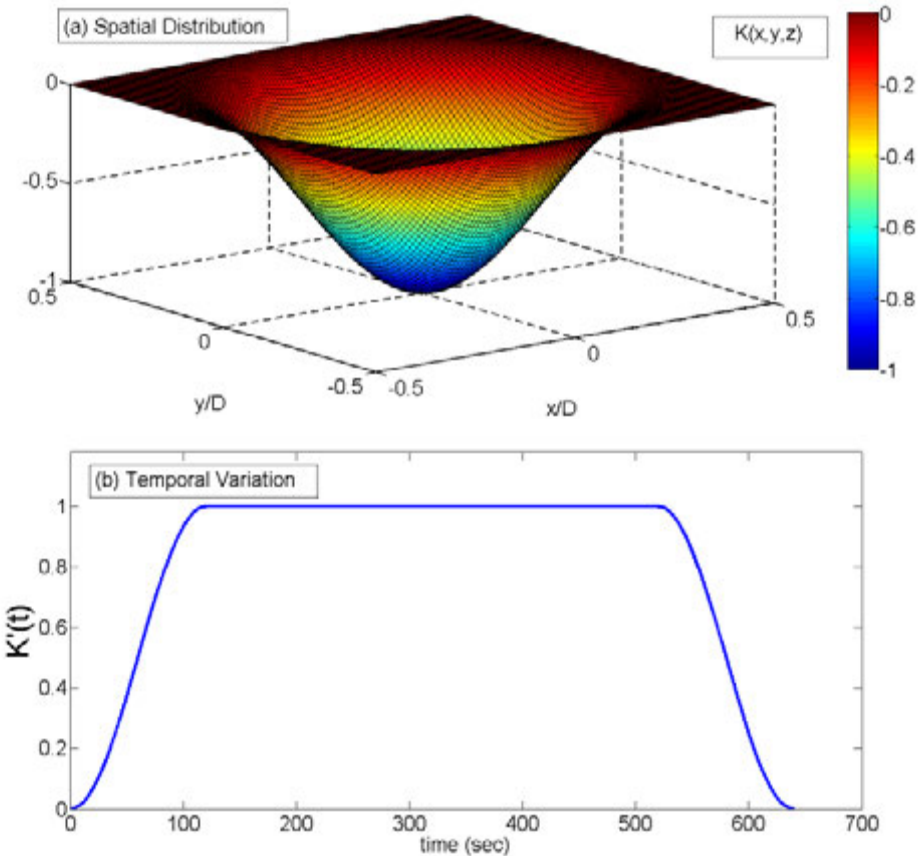

Figure 2. *Spatial and temporal distribution functions*

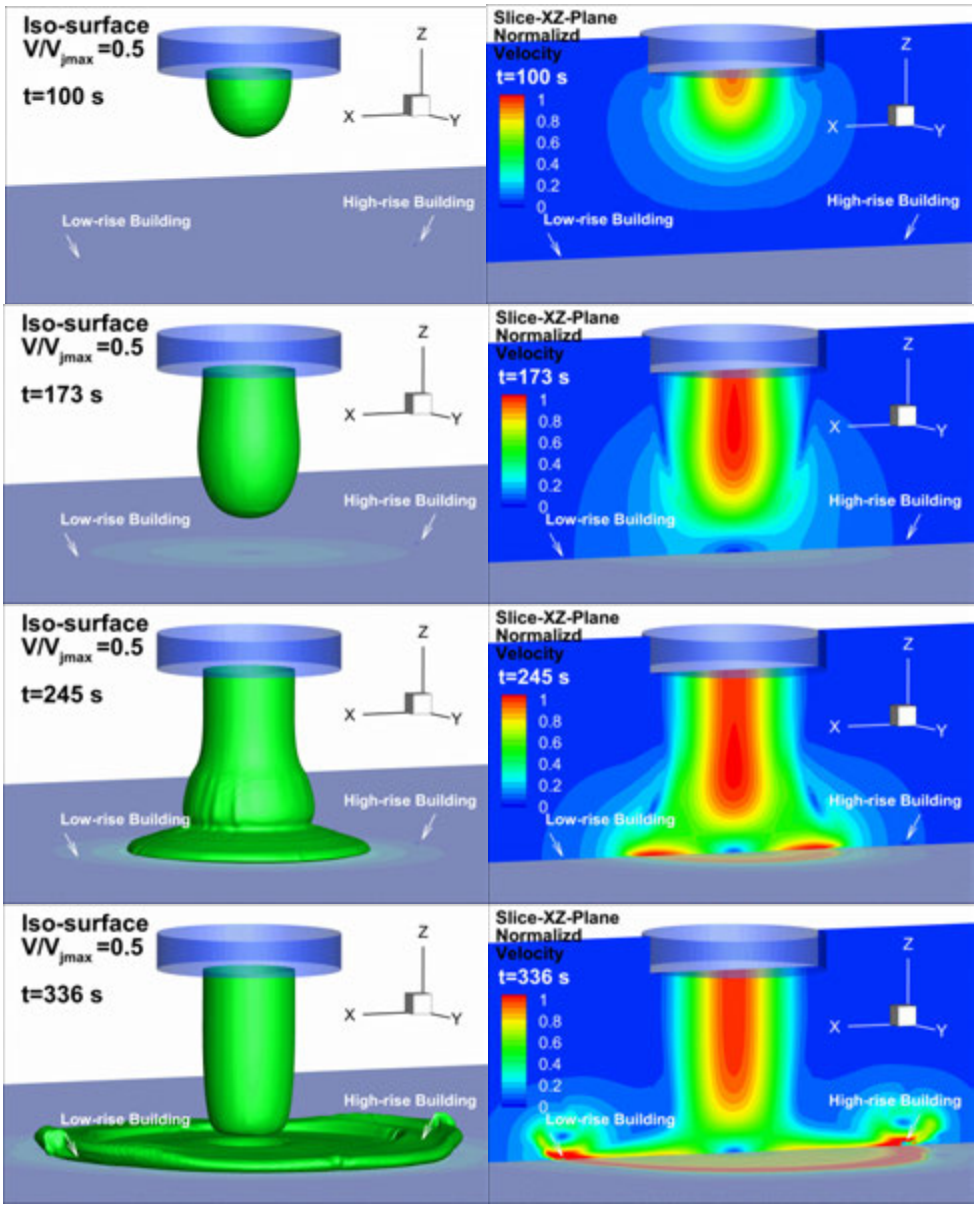

Figure 3. *Velocity iso-surface and cut-plane contour for improved impinging jet model*

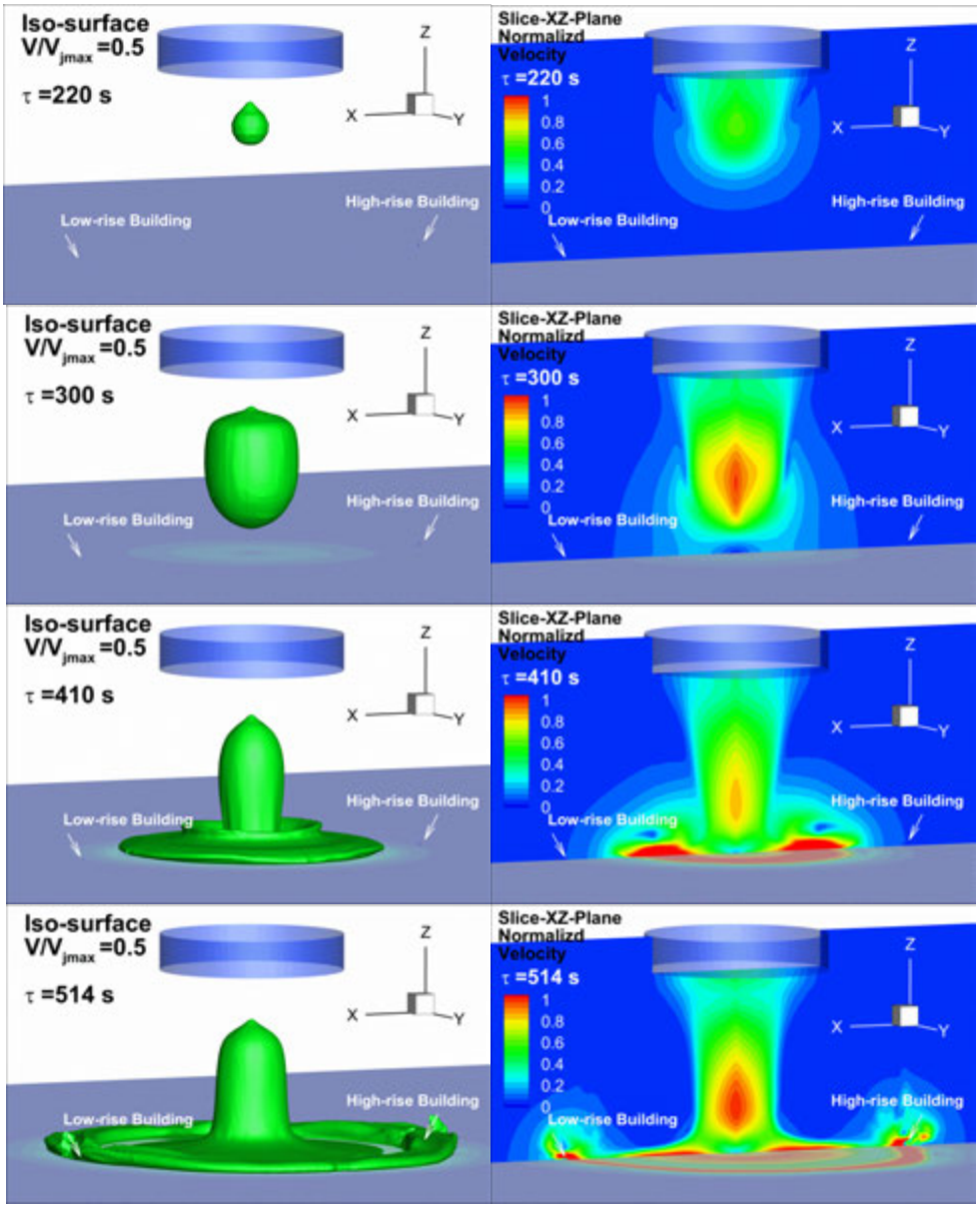

Figure 4. *Velocity iso-surface and cut-plane contour for cooling source model*

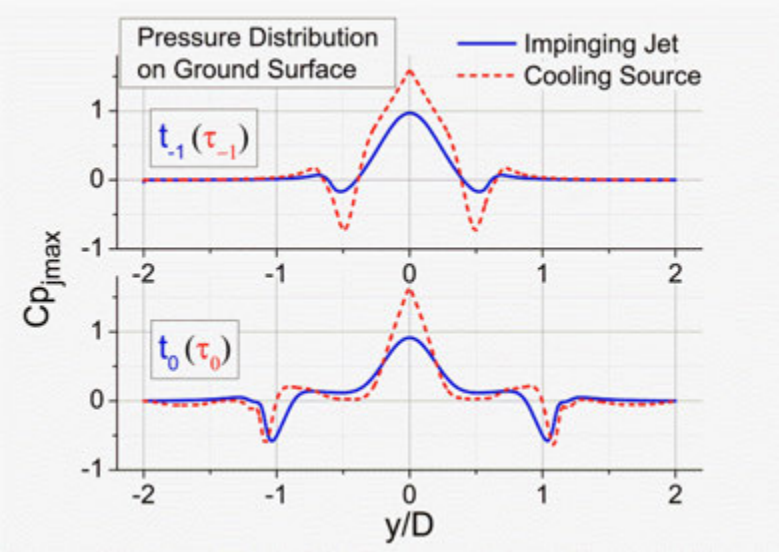

Figure 5. *Ground pressure distribution along y direction at two time steps*

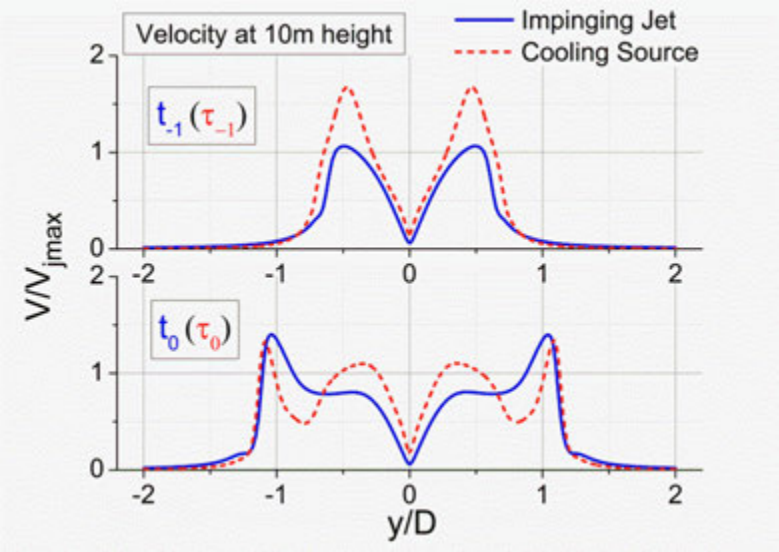

Figure 6. *Wind speed at 10m height along y direction at two time steps*

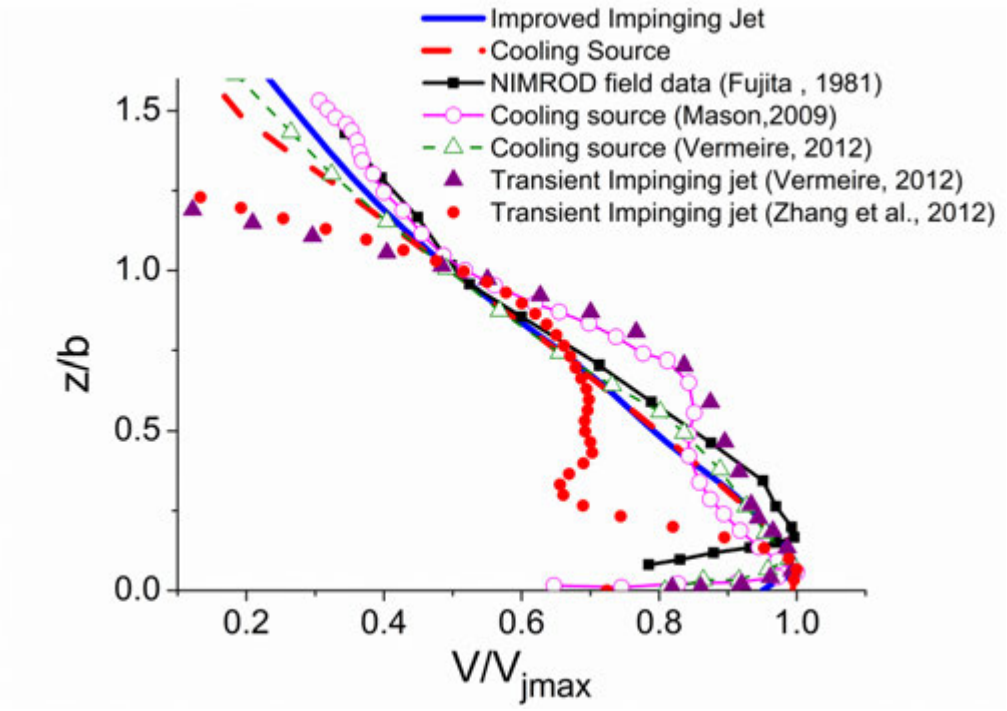

Figure 7. *Comparison of velocity profile at building location*

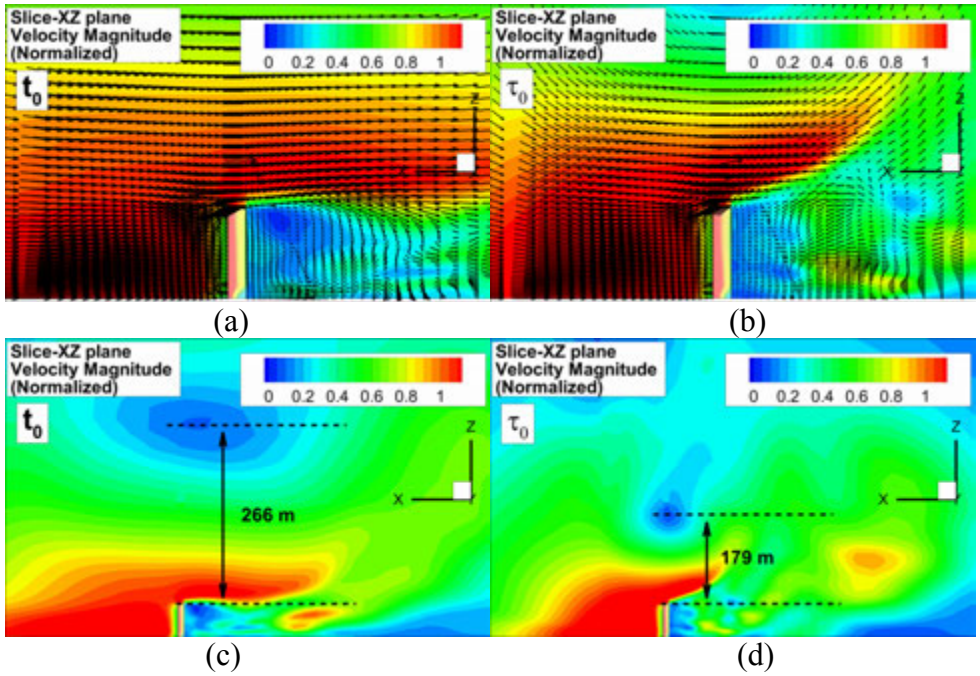

Figure 8. *Velocity contours around the high-rise building at the critical time*
(a) zoomed-in view (c) zoomed-out view of impinging jet
(b) zoomed-in view (d) zoomed-out view of cooling source

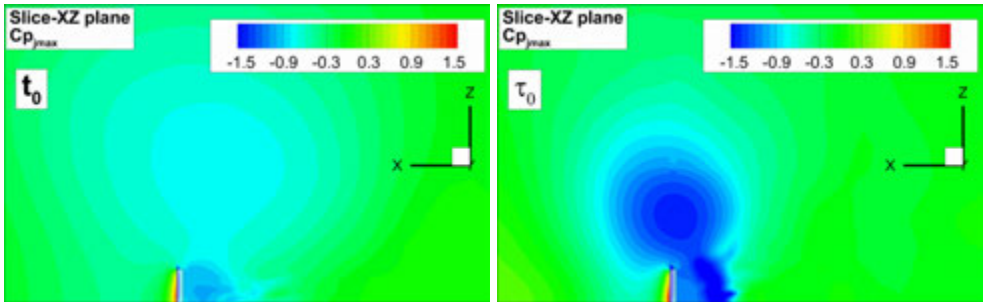

(a) (b)

Figure 9. *Pressure coefficient contours around the high-rise building at the critical time (a) impinging jet; (b) cooling source*

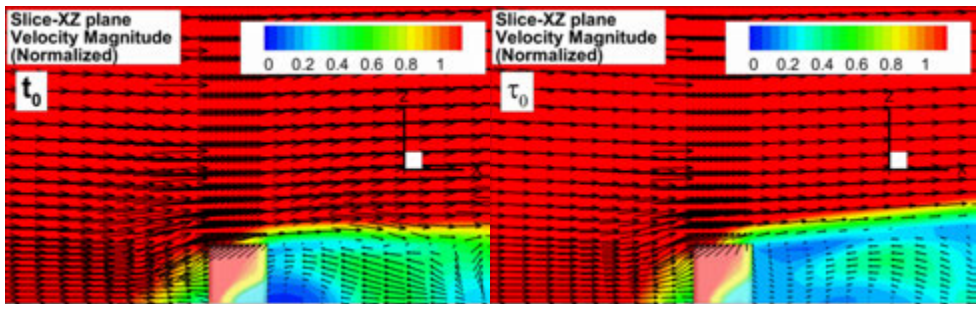

Figure 10. *Velocity contours around the low-rise building at the critical time (Left-impinging jet; right-cooling source)*

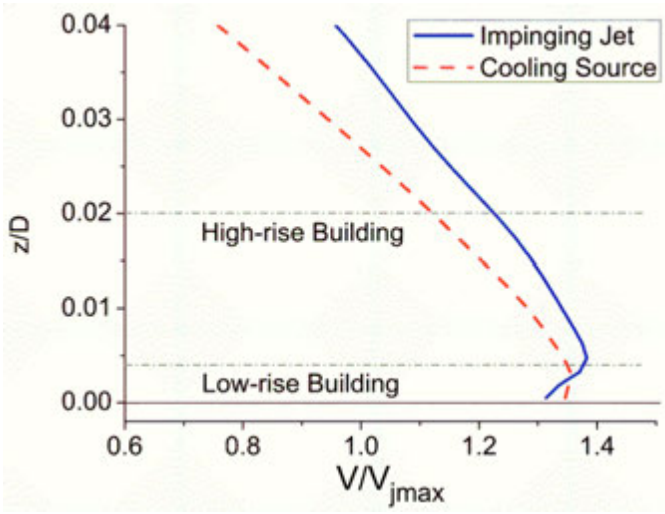

Figure 11. *Normalized velocity profile at r/D=1(at time* $t_0(\tau_0)$*)*

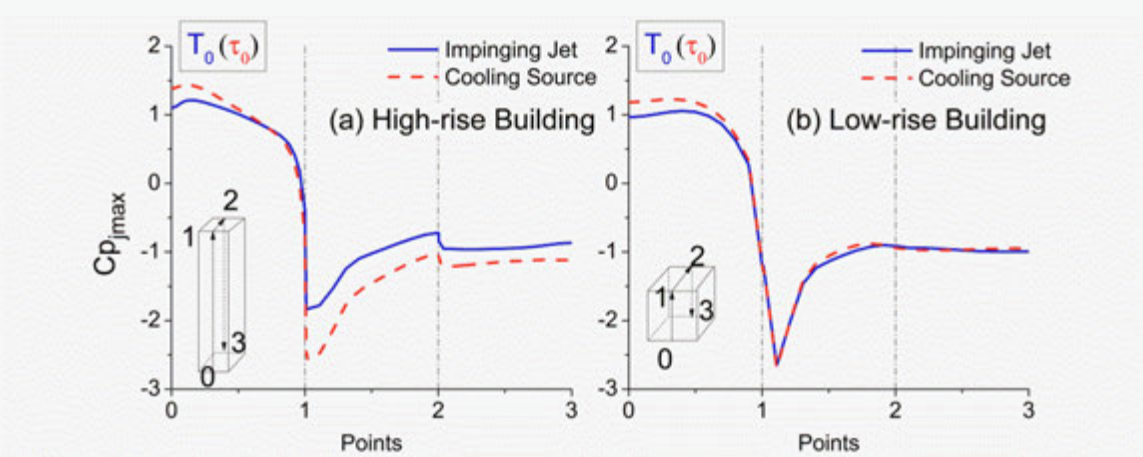

Figure 12. *Pressure coefficients along the centerline of the buildings (at time* $t_0(\tau_0)$*)*

CHAPTER 7

GENERAL CONCLUSION

1. Major Accomplishments of the Current Research

Microburst produces unique flow features that are significantly different from those typically expected in the boundary-layer winds. Thunderstorm downbursts caused an average of $1.4 billion property loss every year in the United States. However, the characteristics of microburst flow field and its wind loading effects on civil structures is far from being fully understood. Meanwhile, limited field research projects could not provide enough information for the wind engineering study of microburst, particularly for the near-ground wind characteristics and wind loading effects on structures. Therefore, further studies are needed to fill these research gaps. The current research includes both experimental and numerical simulations of microburst-type winds and studies of wind loading effects on different civil structural models, utilizing both impinging jet and cooling source approaches. The major accomplishments of this research are summarized below.

1) Studied the flow field of a steady impinging jet using both three-dimensional point velocity measurements and Particle Image Velocimetry (PIV). The detailed information of velocity and turbulence distribution in the outflow of the simulated microburst was revealed. Results were compared with the previous studies and the field data, which suggested that a steady impinging jet resembles a statistical average of a series of simulated microburst events with a time period approaching infinity. The steady

impinging jet was then used for the study of microburst-wind loading effects on different building models.

2) Studied the microburst flow-structure interaction and wind loading effects on two gable-roofed building models, by conducting PIV and surface pressure measurements. The effects of important parameters, such as the distance between the centers of the microburst-like winds and the house models, the roof angle and the orientation angles of the house models with respect to the oncoming microburst-like wind, and the Reynolds numbers of the microburst-like flow, were assessed quantitatively. Pressure distributions were compared with those defined in ASCE 7-05 standard to address the different wind loads induced by microburst winds.

3) Studied the microburst-wind loading effects on low-rise buildings with various geometric shapes, including a cube, a grain bin model, and two gable-roofed building models. Both mean and fluctuating pressure distribution were studied and compared. These results were also compared with those obtained in the conventional boundary-layer winds. The purpose of this study is to establish a preliminary database and general understanding on the wind loading effects on different low-rise structures.

4) Studied the mean and dynamic features of microburst-wind loads on a high-rise building model. Both the mean and dynamic wind loads were found to depend on the radial location and the orientation of the high-rise building within a microburst flow field. Power spectrum density of the velocity and force coefficient fluctuations was also investigated to reveal different frequency components of the dynamic wind loads. It was found that the along-wind and across-wind force fluctuations were better correlated in

the outburst wind than those in the ABL wind. Evidence suggests that the dynamic wind loads were influenced by the low-frequency movement of primary vortices and the high turbulence in the outburst region.

5) Compared the transient behaviors of an impinging jet model and a cooling source model by conducting a 2-D axisymmetric numerical simulation. Several differences in the flow field evolution were revealed, mainly related to the different formation and transportation process of the primary vortex. Ground surface pressure distributions were found to be different due to different forcing parameter of the two models. Comparison with the field data suggested that both models resembled the dynamic features of a real microburst outflow. However, results showed that the cooling source model could produce a reasonable instantaneous radial velocity profile at maximum wind condition, while the transient impinging jet model resulted in some deviation from field measurements.

6) Conducted 3-D numerical simulation to compare the microburst flow field ant its wind loading effects on building models, using an improved impinging jet model and a cooling source model. The macroscopic flow features and a comparison with previous research data suggested that by eliminating the strong shear at the jet interface, the improved impinging jet model provided a reasonable simulation of the transient microburst flow field, similar as the simulation of the cooling source model. Differences in the pressure and velocity distributions at different time-steps were found mainly due to the extra hydrostatic pressure added by the density of the cooled air in the cooling

source model. Wind loading effects and fluid-structure interaction around a high-rise building and a low-rise building were analyzed.

2. Recommendations for Future Research

Based on the research accomplishments as discussed above, the following recommendations are made:

1) The effect of the translational motion on microburst-wind loads has been given in Appendix A. However, due to the relatively small translational speed of the current microburst simulator, the effect was not significant. A microburst simulator with faster translating speed should be established to study a realistic translating microburst.

2) A larger microburst simulator should be established to obtain a better scale for both the flow field and the building models. Resolution and accuracy of the measurement will be improved by doing so.

3) A laboratory cooling source model would be helpful to get a better understanding of this natural phenomenon and the validation of the numerical results.

APPENDIX

EFFECTS OF THE TRANSLATIONAL MOTION ON MICROBURST-WIND LOADS

The effect of the translational motion on microburst-wind loads has been considered during the current research. However, due to the relatively small translational speed of the current microburst simulator, the effect was generally not significant. The effects of translational motion on mean and fluctuating wind loads of the high-rise building model was shown here as an example. Detailed parameters and definitions can be found in Chapter 5. Figure 1 shows the time history of along-wind and across-wind loads under different translational speeds. It can be seen that due to the relatively small translational speeds (compared to $V_{jet}\approx13$ m/s), the translational motion generally did not affect the mean wind loads on the building model. Table 1 summarizes the translational effects on the fluctuating wind loads. It was found that the fluctuation of the along-wind load increased slightly as the translational speed increased, while the fluctuation of the across-wind load had an opposite trend.

Further studies are needed to accurately quantify the translational effects on both mean and fluctuating wind loads.

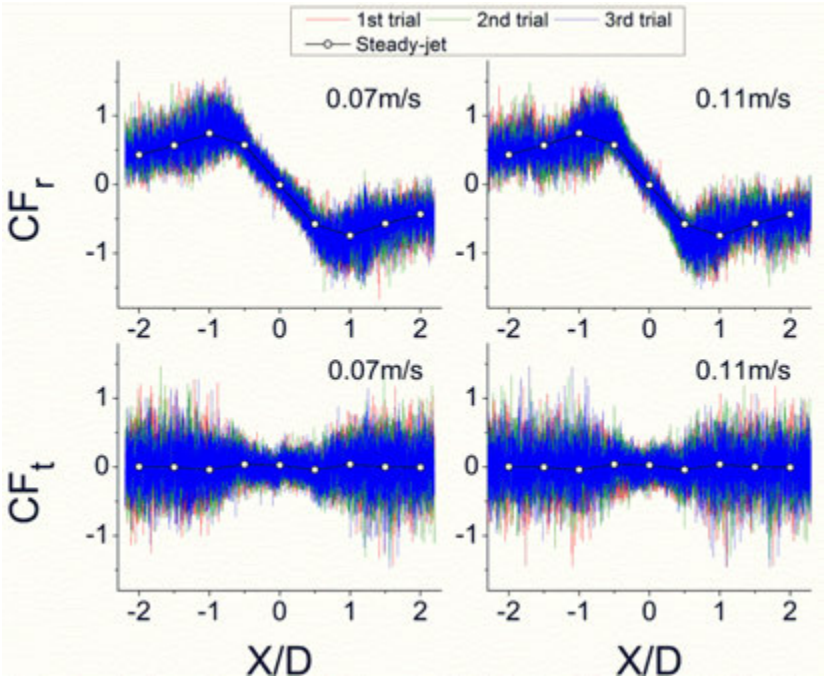

Figure 1. *Time history of along-wind and across-wind loads under different translational speeds*

Table 1. *Root-mean-square of fluctuating wind loads of the high-rise building model*

Stationary			**Translating speed=0.07m/s**			**Translating speed=0.11m/s**		
r/D	**CF_r**	**CF_t**	**Trials #**	**CF_r**	**CF_t**	**Trials #**	**CF_r**	**CF_t**
0.0	0.17	0.13	**1st**	0.29	0.28	**1st**	0.31	0.24
0.5	0.12	0.15	**2nd**	0.29	0.26	**2nd**	0.31	0.23
1.0	0.21	0.28	**3rd**	0.29	0.27	**3rd**	0.31	0.25
1.5	**0.21**	**0.32**	**averaged**	0.29	0.27	**averaged**	0.31	0.24
2.0	0.21	0.31						